

# THE HYBRID PRESSURIZED AIR RECEIVER (HPAR) FOR COMBINED CYCLE SOLAR THERMAL POWER PLANTS

by

Holger Kretzschmar

*Thesis presented for the degree of Master of Science in the  
Faculty of Engineering at Stellenbosch University*



Department of Mechanical and Mechatronic Engineering,  
Stellenbosch University,  
Private Bag X1, Matieland 7602, South Africa.

Supervisor: Mr. P. Gauché

March 2014

# Declaration

By submitting this thesis electronically, I declare that the entirety of the work contained therein is my own, original work, that I am the owner of the copyright thereof (unless to the extent explicitly otherwise stated) and that I have not previously in its entirety or in part submitted it for obtaining any qualification.

Date: .....

Copyright © 2014 Stellenbosch University  
All rights reserved.

# Abstract

## THE HYBRID PRESSURIZED AIR RECEIVER (HPAR) FOR COMBINED CYCLE SOLAR THERMAL POWER PLANTS

H. Kretzschmar

*Department of Mechanical and Mechatronic Engineering,  
Stellenbosch University,  
Private Bag X1, Matieland 7602, South Africa.*

Thesis: MScEng (Mech)

March 2014

Concentrating solar power technology is a modern power generation technology in which central receiver systems play a significant role. For this technology a field of heliostats is used to reflect solar irradiation to the receiver located on top of the tower. An extensive review has shown that contemporary receiver designs face geometric complexities, lack of thermal efficiency as well as issues with durability and cost. The purpose of this study is to develop a new receiver concept that can potentially reduce these issues. A parametric analysis was used to identify potential means of improvement based on an energy balance approach including sensitivities involved with convection and radiation heat transfer. Design criteria such as the use of headers to minimize pressure drop was also investigated. Based on these findings the hybrid pressurized air receiver was developed which is a combination of tubular and volumetric receiver technologies. The fundamental idea of the receiver was investigated by simulating the ray-tracing and coupled natural convection and radiation heat transfer. The ray-tracing results have shown that the use of quartz glass is a prospective solution to higher allowable flux densities, but with reflection losses in the order of 7%. The coupled natural convection heat transfer simulation further revealed that the receiver concept effectively eliminates the escape of buoyant plumes and radiative heat losses are minimized. Empirical data was gathered from a medium flux concentrator and good agreement with the numerical results was obtained. The thesis therefore concludes that the research outcomes were met. Ongoing research aims to optimise the receiver concept for a 5 MW pilot plant.

# Uittreksel

## DIE HIBRIEDE SAAMGEPERSDE-LUG ONTVANGER VIR GEKOMBINEERDE SIKLUS SONTERMIESE KRAGSTASIES

(“HYBRID PRESSURIZED AIR RECEIVER (HPAR) FOR COMBINED CYCLE  
SOLAR THERMAL POWER PLANTS”)

H. Kretzschmar

*Departement Meganiese en Megatroniese Ingenieurswese,  
Universiteit van Stellenbosch,  
Privaatsak X1, Matieland 7602, Suid Afrika.*

Tesis: MScIng (Meg)

Maart 2014

Gekonsentreerde sonkrag tegnologie is ’n moderne kragopwekkingstegnologie waar sentrale ontvangersisteme ’n beduidende rol speel. Vir hierdie tegnologie word ’n veld heliostate gebruik om sonstraling na die ontvanger wat aan die bopunt van die toring geleë is te reflekteer. ’n Omvattende hersiening het daarop gewys dat kontemporêre ontwerpe van die ontvangers ’n aantal geometriese kompleksiteite, ’n tekort aan termiese doeltreffendheid sowel as probleme in terme van duursaamheid en koste in die gesig staan. Die doel van die studie is om ’n nuwe ontvangerskonsep te ontwikkel wat moontlik hierdie probleme kan verminder. ’n Parametriese analise is gebruik om potensiële maniere van verbetering aan te dui wat gebaseer is op ’n energiebalans benadering; insluitend sensitiwiteite betrokke by konvektiewe en stralingswarmte-oordrag. Ontwerpkriteria soos die gebruik van spuitstukke om drukverliese te minimaliseer is ook ondersoek. Gebaseer op hierdie bevindinge is die hibriede saamgepersde-lug ontvanger ontwikkel. Laasgenoemde is ’n kombinasie van buis- en volumetriese ontvangertegnologie. Die fundamentele idee van die ontvanger is ondersoek deur straalberekening asook die gelyktydige natuurlike konveksie en stralingswarmte-oordrag te simuleer. Die straalberekeningsresultate het getoon dat die gebruik van kwarts glas ’n moontlike oplossing is om hoër stralingsintensiteit te bereik, maar met refleksieverliese in die orde van 7%. Die gelyktydige natuurlike konveksie en stralingswarmte-oordrag simulatie het verder aan die lig gebring dat die ontvangerkonsep die ontsnapping

van konvektiewe hitte uitskakel en die stralingsverliese minimaliseer. Empiriese data is ingesamel van 'n konsentreerder met medium energiedigtheid en 'n goeie ooreenstemming met die numeriese resultate is verkry. Uit die tesis kan dus afgelei word dat die navorsingsuitkomst bereik is. Voortdurende navorsing het ten doel om die ontvangerkonsep te optimeer vir 'n 5 MW loodsaanleg.

# Acknowledgements

I would like to express my sincere gratitude to the following people and organisations:

- My family and friends
- Mr. P. Gauche (supervisor)
- Dr. J.E. Hoffmann (co-supervisor)
- STERG staff
- Sasol Technology
- Department of Science and Technology (DST) Solar Thermal Spoke Fund
- Stellenbosch University Hope Project

# Dedications

*This thesis is dedicated to my parents, family and friends who have supported me throughout this period. I could not have done this without them.*

# Contents

<b>Declaration</b>	<b>i</b>
<b>Abstract</b>	<b>ii</b>
<b>Uittreksel</b>	<b>iii</b>
<b>Acknowledgements</b>	<b>v</b>
<b>Dedications</b>	<b>vi</b>
<b>Contents</b>	<b>vii</b>
<b>List of Figures</b>	<b>x</b>
<b>List of Tables</b>	<b>xii</b>
<b>Nomenclature</b>	<b>xiii</b>
<b>1 Introduction</b>	<b>1</b>
1.1 Background . . . . .	1
1.2 Objective . . . . .	4
1.3 Methodology . . . . .	5
1.4 Scope of Project . . . . .	5
1.5 Structure of Document . . . . .	6
<b>2 Literature Review</b>	<b>8</b>
2.1 Introduction . . . . .	8
2.2 External Tube Receiver . . . . .	8
2.3 Cavity Receiver . . . . .	10
2.4 Volumetric Receiver . . . . .	11
2.5 Small Particle Receiver . . . . .	14
2.6 Emerging New Receiver Concepts . . . . .	15
2.7 Conclusion . . . . .	16
<b>3 Parametric Analysis</b>	<b>17</b>
3.1 Introduction . . . . .	17



3.2	Energy Balance . . . . .	17
3.3	Entropy Generation . . . . .	19
3.4	Exergy Balance . . . . .	19
3.5	Parametric Analysis on System Efficiency . . . . .	20
3.6	Parametric Analysis on Internal Pipe Flow . . . . .	26
3.7	Conclusion . . . . .	31
<b>4</b>	<b>Hybrid Pressurized Air Receiver Concept</b>	<b>32</b>
4.1	Introduction . . . . .	32
4.2	Concept Development . . . . .	32
4.3	Material Considerations . . . . .	35
4.4	Expected Benefits of the HPAR Concept . . . . .	36
4.5	Potential Drawbacks of the HPAR Concept . . . . .	37
4.6	Experimental Manifestation of the HPAR . . . . .	37
4.7	Numerical Analysis and Validation Method . . . . .	38
4.8	Conclusion . . . . .	40
<b>5</b>	<b>Ray-Tracing Analysis</b>	<b>41</b>
5.1	Introduction . . . . .	41
5.2	Description of Model . . . . .	41
5.3	Modelling Setup . . . . .	42
5.4	Numerical Results . . . . .	46
5.5	Conclusion . . . . .	48
<b>6</b>	<b>Coupled Natural Convection and Radiation Heat Transfer Simulation</b>	<b>49</b>
6.1	Introduction . . . . .	49
6.2	Buoyancy-Driven Flow . . . . .	50
6.3	Radiation Heat Transfer . . . . .	52
6.4	Flux Mapping Strategies . . . . .	54
6.5	Modelling Setup . . . . .	55
6.6	Numerical Results . . . . .	61
6.7	Conclusion . . . . .	63
<b>7</b>	<b>Empirical Validation</b>	<b>64</b>
7.1	Introduction . . . . .	64
7.2	Experimental Setup . . . . .	64
7.3	Experimental Results . . . . .	65
7.4	Conclusion . . . . .	70
<b>8</b>	<b>Conclusion</b>	<b>71</b>
8.1	Conclusion . . . . .	71
8.2	Research Contribution and Outlook . . . . .	71
8.3	Recommendations . . . . .	72

<i>CONTENTS</i>	<b>ix</b>
<b>Appendices</b>	<b>73</b>
<b>A Correlations for Fluid Properties</b>	<b>74</b>
A.1 Air . . . . .	74
A.2 Sodium . . . . .	75
A.3 Solar Salt . . . . .	76
<b>B Development of an Internal Pipe Flow Model and Validation</b>	<b>77</b>
B.1 Introduction . . . . .	77
B.2 Mathematical Model . . . . .	77
B.3 Program Structure . . . . .	82
B.4 Program Validation . . . . .	84
<b>C Design and Calibration of a Cold Water Flat Plate Calorimeter</b>	<b>87</b>
C.1 Introduction . . . . .	87
C.2 Calorimeter Design . . . . .	87
C.3 Calibration . . . . .	89
<b>D Optical Simulation and Validation of the Solar Concentrator</b>	<b>92</b>
D.1 Introduction . . . . .	92
D.2 Modelling Setup . . . . .	92
D.3 Modelling Results . . . . .	92
D.4 Empirical Validation . . . . .	97
D.5 Conclusion . . . . .	100
<b>E Design of Empirical Validation Setup</b>	<b>102</b>
E.1 Introduction . . . . .	102
E.2 Specification . . . . .	102
E.3 Pressure Drop Calculation . . . . .	103
E.4 Fan Specification . . . . .	104
E.5 Venturi Design . . . . .	104
E.6 Venturi Calibration . . . . .	105
E.7 Thermocouple Calibration . . . . .	106
<b>List of References</b>	<b>107</b>

# List of Figures

1.1	The Stellenbosch University Solar Power Thermodynamic cycle . . .	3
1.2	Illustration of power cycle efficiency curves . . . . .	4
2.1	Modular cavity receiver . . . . .	11
2.2	Pressurized volumetric receiver . . . . .	12
2.3	Dual receiver concept . . . . .	14
2.4	Reticulate porous ceramic receiver . . . . .	15
3.1	Illustration of irreversibility and actual work . . . . .	20
3.2	Plot of receiver efficiency versus heat losses . . . . .	21
3.3	Thermodynamic efficiency curves versus concentration ratio . . . . .	22
3.4	Stagnation temperature plot versus aspect ratio . . . . .	24
3.5	Sensitivity of view factor . . . . .	25
3.6	Sensitivity of view factor and heat transfer coefficient . . . . .	25
3.7	Sensitivity of mass flow rate . . . . .	27
3.8	Sensitivity of mass flow rate versus pressure drop . . . . .	28
3.9	Sensitivity of heat transfer fluid . . . . .	29
3.10	Flownex schematic of header . . . . .	30
3.11	Flownex schematic of pipes in series . . . . .	30
4.1	Concept development of the Hybrid Pressurized Air Receiver (HPAR)	33
4.2	Illustration of the transmission zones . . . . .	34
4.3	Schematic diagram of a combined cycle utilizing the HPAR . . . . .	35
4.4	Sketch of the experimental manifestation of the HPAR . . . . .	37
4.5	Outline of numerical simulation and validation method . . . . .	39
5.1	Illustration of a dual-axis tracking solar concentrator . . . . .	42
5.2	Illustration of the data exchange between the Matlab and SolTrace	43
5.3	Illustration of the ray paths as modelled in SolTrace . . . . .	47
5.4	Ray hitpoints of fully-packed tube receiver . . . . .	48
5.5	Ray hitpoints of receiver including quartz wafers . . . . .	48
6.1	Illustration of flux projection method . . . . .	55
6.2	Illustration of named selections used in numerical model . . . . .	56
6.3	Transmission curve of fused silica quartz glass . . . . .	58

6.4	Residual plot of simulation run . . . . .	61
6.5	Contour plot of receiver with forced airflow and no quartz wafers .	61
6.6	Contour plot of receiver without forced airflow and no quartz wafers	61
6.7	Contour plot of receiver including quartz wafers and forced airflow .	62
6.8	Contour plot of receiver including quartz wafers and no forced airflow	62
7.1	Image of medium flux solar concentrator . . . . .	65
7.2	Validation of fully packed tube receiver including the forced airflow	66
7.3	Validation of fully packed tube receiver excluding forced airflow . .	66
7.4	Transient plot of fully packed tube receiver including forced airflow	67
7.5	Transient plot of fully packed tube receiver excluding forced airflow	67
7.6	Transient plot of quartz receiver including forced airflow . . . . .	68
7.7	Validation of quartz receiver including forced airflow . . . . .	69
7.8	Validation of quartz receiver excluding forced airflow . . . . .	69
7.9	Transient plot of quartz receiver excluding forced airflow . . . . .	70
B.1	Illustration of major energy terms . . . . .	78
B.2	Differential control volume of tube element . . . . .	80
B.3	General program structure of internal pipe flow model . . . . .	83
B.4	Fluid-flow network model of receiver tubes in Flownex . . . . .	84
B.5	Validation of internal pipe flow model using Flownex . . . . .	85
C.1	Cold water flat plate calorimeter . . . . .	88
C.2	Calibration setup of cold water flat plate calorimeter . . . . .	89
C.3	Illustration of the resistance heater, insulation and the calorimeter .	90
C.4	Transient thermal response of the calorimeter . . . . .	90
C.5	Power calibration curve of calorimeter . . . . .	91
D.1	Illustration of the solar concentrator as modelled in SolTrace . . . .	93
D.2	Flux map of target at perfectly aligned mirrors . . . . .	94
D.3	Flux map of back wall at perfectly aligned mirrors . . . . .	94
D.4	Flux map characterisation from image of target . . . . .	95
D.5	Flux map of target with adapted aimpoint corrections . . . . .	96
D.6	Flux map of the back wall with adapted aimpoint corrections . . .	96
D.7	Flux map of target with large specular error . . . . .	97
D.8	Flux map of the back wall with large specular error . . . . .	97
D.9	Snapshot image from the infra-red camera . . . . .	99
D.10	Comparison of absorbed energy versus solar irradiance of calorimeter	99
D.11	Normalized absorbed power of calorimeter . . . . .	100
E.1	Schematic of components used in test setup . . . . .	103
E.2	Fan curve K100 XL . . . . .	105
E.3	Power curve K100 XL . . . . .	105
E.4	Venturi calibration curve plotted over range of pressure values . . .	105

# List of Tables

4.1	Parametric case description to investigate the HPAR concept . . . .	40
5.1	Optical properties of mirror glass and carbon black paint . . . . .	44
6.1	Material properties of quartz, ceramic insulation and stainless steel	58
6.2	Flux profiles for wall boundary conditions of fully packed tube receiver	59
6.3	Flux profiles for wall boundary conditions of the quartz receiver . .	60
B.1	Parametric values used for validation . . . . .	85
D.1	Validation results of solar concentrator . . . . .	98
E.1	Pressure drop through rock bed for different Reynolds numbers . .	104

# Nomenclature

## Constants

$g =$	9.81 m/s <sup>2</sup>
$\sigma =$	$5.67 \times 10^{-8}$ W/m <sup>2</sup> K <sup>4</sup> (Stefan-Boltzmann's constant)
$\pi =$	3.143
$h =$	$6.662\ 606\ 896 \times 10^{-34}$ J/s (Planck's constant)
$k_b =$	$1.380\ 650\ 4 \times 10^{-23}$ J/K (Boltzmann's constant)

## Variables

$Ar$	Archimedes number . . . . .	[ ]
$A$	area . . . . .	[m <sup>2</sup> ]
$A_r$	collective absorber tube area . . . . .	[m <sup>2</sup> ]
$C$	concentration ratio . . . . .	[ ]
$C, M, N$	Dittus Boehlter coefficients . . . . .	[ ]
$C_1, C_2$	auxiliary coefficients . . . . .	[ ]
$c_p$	specific heat capacity of constant pressure . . . . .	[kJ/kg K]
$D_i, D_o$	inner and outer tube diameter . . . . .	[m]
$dx$	elementary tube length . . . . .	[m]
$E$	total energy . . . . .	[kJ]
$E_m$	total mass transfer . . . . .	[kJ]
$E_{b\lambda}$	Planck's emissive power . . . . .	[W/m <sup>2</sup> ]
$f$	friction factor . . . . .	[ ]
$F$	aggregate configuration factor . . . . .	[ ]
$F'$	collector efficiency factor . . . . .	[ ]
$F_R$	heat removal factor . . . . .	[ ]
$Gr$	Grashoff number . . . . .	[ ]
$h$	enthalpy . . . . .	[kJ/kg]
$h_c$	convective heat transfer coefficient . . . . .	[W/m K]
$h_w$	external convective heat transfer coefficient . . . . .	[W/m K]
$I$	radiation intensity . . . . .	[W/m <sup>2</sup> ]

$I_{xx}, I_{yy}, I_{zz}$	projected radiation intensity . . . . .	[W/m <sup>2</sup> ]
$I_{b\lambda}$	black body intensity . . . . .	[W/m <sup>2</sup> ]
$j, k$	local surface . . . . .	[ ]
$k$	thermal conductivity . . . . .	[W/m K]
$L$	characteristic length . . . . .	[m]
$n$	refractive index . . . . .	[ ]
$N$	total number of surfaces . . . . .	[ ]
$Nu$	Nusselt number . . . . .	[ ]
$m$	mass . . . . .	[kg]
$P$	pressure . . . . .	[Pa]
$Pr$	Prantdl number . . . . .	[ ]
$Q$	total heat transfer . . . . .	[kJ]
$Q'$	total heat transfer per unit length . . . . .	[kJ/m]
$Q''$	total heat transfer per unit area . . . . .	[kJ/m <sup>2</sup> ]
$r$	radius . . . . .	[m]
$Ra$	Rayleigh number . . . . .	[ ]
$Re$	Reynolds number . . . . .	[ ]
$S$	path length . . . . .	[m]
$S$	incident collector flux . . . . .	[W/m <sup>2</sup> ]
$\dot{S}_{gen}$	entropy generated . . . . .	[W/K]
$s$	specific entropy . . . . .	[kJ/kg K]
$t$	time . . . . .	[s]
$T$	temperature . . . . .	[°C]
$U_l$	overall heat loss coefficient . . . . .	[W/m K]
$U_o$	overall internal loss coefficient . . . . .	[W/m K]
$V$	velocity . . . . .	[m/s]
$W$	total work . . . . .	[kJ]
$\dot{X}_{dest}$	exergy destroyed . . . . .	[W/K]
$x, y, z$	coordinate (global) . . . . .	[m]
$x', y', z'$	coordinate (local) . . . . .	[m]
$\alpha$	absorptivity . . . . .	[ ]
$\alpha$	thermal diffusivity . . . . .	[m <sup>2</sup> /s]
$\beta$	thermal expansion coefficient . . . . .	[1/K]
$\beta$	extinction coefficient . . . . .	[ ]
$\delta_{err}$	error deviation . . . . .	[ ]
$\delta_{ij}$	visibility function . . . . .	[ ]

$\epsilon$	emissivity . . . . .	[ ]
$\epsilon$	void fraction . . . . .	[ ]
$\eta$	efficiency . . . . .	[ ]
$\kappa$	spectral absorptivity coefficient . . . . .	[ ]
$\mu$	dynamic viscosity . . . . .	[kg/m s]
$\Omega$	solid angle . . . . .	[rad]
$\psi$	exergy per unit mass . . . . .	[W/kg]
$\phi$	direct normal irradiance . . . . .	[W/m <sup>2</sup> ]
$\Phi$	phase function . . . . .	[ ]
$\rho$	density . . . . .	[kg/m <sup>3</sup> ]
$\rho$	reflectivity . . . . .	[ ]
$\sigma$	spectral emissivity coefficient . . . . .	[ ]
$\sigma_s$	scattering coefficient . . . . .	[ ]
$\theta$	angle . . . . .	[rad]
$\Theta$	normalized absorbed energy . . . . .	[1/m <sup>2</sup> ]
$v$	specific volume . . . . .	[m <sup>3</sup> /kg]
$\nu$	kinematic viscosity . . . . .	[m <sup>2</sup> /s]
$\zeta$	Z-rotation angle . . . . .	[rad]

### Vectors and Tensors

$\mathbf{H}_p$	vector from origin to heliostat
$\mathbf{N}$	surface normal of heliostat
$\mathbf{S}$	vector from sun to heliostat
$\mathbf{r}$	position vector
$\mathbf{s}$	direction vector
$\mathbf{s}'$	scattering direction vector
$\mathbf{T}_p$	vector from origin to target
$\mathbf{R}$	vector from heliostat to target
$\mathbf{U}_1$	desired x-axis unit vector
$\mathbf{U}_2$	calculated x-axis unit vector
$\mathbf{V}$	vertical vector from heliostat

### Subscripts

1,2	initial and final state
ap	aperture
abs	absorber
a, amb	ambient



atm	atmosphere
Carnot	Carnot
c	collector
conv	convection
cu	copper
e	electric
elv	elevation
Erg	Ergun
f	fluid
i	interior
k	system boundary
lam	laminar
$l \rightarrow r, r \rightarrow l$	local to reference and reference to local
max	maximum
norm	normalized
o	dead state, operating conditions, exterior
rad	radiation
rec	receiver
refl	reflection
u	useful
s	surface, static
sky	sky
sys	system
t	thermal
tot	total
tilt	tilt
x, y, z	coordinate
Z	zenith
$\lambda$	wavelength
$\dot{\quad}$ (dot)	quantity per unit time
$\hat{\quad}$ (hat)	unit vector
* (asterisk)	characteristic

**Abbreviations**

CCD	Charge Coupled Device
CFD	Computational Fluid Dynamics
CPC	Compound Parabolic Concentrator

CPU	Central Processing Unit
CR	Concentration Ratio
CRS	Central Receiver Systems
CSIRO	Commonwealth Scientific and Industrial Research Organisation
CSP	Concentrating Solar Power
DAQ	Data Acquisition System
DC	Direct Current
DLR	German Aerospace Centre
DIAPR	Directly-Irradiated Annular Pressurized Receiver
DNI	Direct Normal Irradiance
DO	Discrete Ordinates
DOS	Disc Operating System
FEMRAY	Finite Element Mesh Ray-Tracing
HPAR	Hybrid Pressurized Air Receiver
HRSR	Heat Recovery Steam Generator
IPCM	Implicit Pressure Correction Method
NNR	National Nuclear Reactor
NREL	National Renewable Energy Laboratory
PBMR	Pebble Bed Modular Reactor
PEGASE	Production of Electricity by Gas Turbine and Solar Energy
PHOEBUS	Technology Program Solar Air Receiver
PSA	Plataforma Solar de Almería
REFOS	Receiver for Solar Fossil Power Plants
RNG	Renormalized Group theory
RPC	Reticulate Porous Ceramic
RTE	Radiative Transfer Equation
S2S	Surface-to-Surface
SASEC	Southern African Solar Energy Conference
SEGS	Solar Electric Generating Systems
SE	Simulation Environment
SOLGATE	Solar Hybrid Gas Turbine Electric Power System
SOLHYCO	Solar Hybrid Power and Cogeneration Plants
SPA	Solar Position Algorithm
SUNSPOT	Stellenbosch University Solar Power Thermodynamic Cycle
TESS	Thermal Energy Storage System
UDF	User-Defined Function

# Chapter 1

## Introduction

To put the remarkable growth of Concentrating Solar Power (CSP) into perspective, Behar *et al.* (2013) highlights that in 2011, 1.3 GW of CSP plants were in operation, 2.3 GW were under construction and 37.1 GW were in the planning phase. The research performed in this project aims to contribute towards the development of this technology by an innovative new patented receiver.

### 1.1 Background

#### 1.1.1 Solar Thermal Power Plants

Solar thermal power plants are modern power generation systems where conventional power blocks are combined with an energy input from concentrating solar collectors. These collectors can be generally classified as 2 types: line-focussing and point-focussing (Gazzo *et al.*, 2010).

Examples of line focussing concentrators include the parabolic trough or linear Fresnel systems. They typically provide concentration ratios of 30 to 80 suns and heat up thermal fluids to about 400 °C (Romero-Alvarez and Zarza, 2007). A parabolic trough collector consists of a parabolic shaped mirror mounted on a high-precision structure. The mirror concentrates the incoming solar rays via single axis tracking onto the absorber tube, which is located at the focal line of the collector system. A heat transfer fluid (e.g., oil, steam, molten salt) gains the thermal energy through the tubes and thus provides the heat input to the turbine, either directly or via a heat exchanger (Price *et al.*, 2002). Linear Fresnel systems work in similar fashion except that they consist of multiple flat mirrors mounted in array lines on the ground (Haeberle *et al.*, 2002).

Point focussing systems have higher thermal efficiencies where concentration ratios of 200 to 1000 suns are obtained. Subsequently, much higher temperatures of up to 1000 °C can be obtained (Romero-Alvarez and Zarza, 2007).

Generally two types of point-focussing systems exist, parabolic dish and Central Receiver System (CRS), also termed solar power towers. Parabolic dishes consist of a paraboloid shaped collector and a receiver system. The collector is mounted on a dual-axis tracking pedestal continuously pointing the receiver system towards the sun. The receiver system typically consists of a series of metal absorber tubes feeding hot gas to a Stirling engine.

Parabolic dishes in general are scaled smaller than power towers, typically in the range of 5 to 50 kW (IRENA, 2012). Here, the thermal energy is converted to electrical energy via a dish Stirling engine or micro turbine. Dish collectors have the potential of achieving the highest efficiencies of all solar concentrating systems. CRS, in contrast to dish Stirling engines, can generate electricity in MW sizes with tower heights reaching up to 150 m and field sizes occupying thousands of hectares (Stine and Geyer, 2001). In these systems incoming solar irradiation is concentrated via multiple tracking mirrors, called heliostats, to the top of the tower. Here an energy absorption unit, called a receiver, converts the incoming light energy to thermal energy. The thermal energy is absorbed by a heat transfer fluid and used in a conventional power cycle.

### 1.1.2 Historical Background on Solar Power Tower Technology

The Solar One tower was the first of its kind built in the USA and commissioned from 1982 to 1988. It was a 10 MW water-steam solar power tower system, and its purpose was to demonstrate that large-scale solar power generation is practical and reliable. In 1991 Solar One was converted from water-steam to a molten salt power plant and renamed Solar Two (Grasse *et al.*, 1991; Pacheco *et al.*, 2000). The purpose of this conversion was to investigate and validate the new technology. In 1999 Solar Two was decommissioned due to financial constraints (Romero-Alvarez and Zarza, 2007). The next large scale power tower, built in Spain by the Spanish company Abengoa, was a 10 MW tower (PS10), which was shortly followed by a larger 20 MW tower (PS20) in 2007 (Grasse *et al.*, 1991; Romero *et al.*, 2002; NREL, 2013). More recent completed projects include the Sierra Sun towers (5 MW) built by eSolar and the Gemasolar plant built by Torresol (Slack *et al.*, 2010; Meduri *et al.*, 2010; Burgaleta *et al.*, 2012).

Many smaller research tower facilities have been developed over the last twenty years primarily in the USA (Sandia National Laboratories), Spain (Plataforma Solar de Almería), Israel (Weizmann Institute of Science), Germany (Solar Institute Julich), Australia (Commonwealth Scientific and Industrial Research Organisation) and France (Themis)(Winter *et al.*, 1991; Stine and Geyer, 2001; Romero *et al.*, 2002; Kolb *et al.*, 2011).

Due to the rapidly increasing demand in energy, many more commercial

solar tower projects have been planned and are currently under construction. Among the biggest is the soon to be completed Ivanpah Solar Electric Generating Systems (SEGS) project which is a 390 MW power tower facility and the Crescent Dunes tower project (110 MW), constructed by SolarReserve (Wiesenberg *et al.*, 2012; Tian and Zhao, 2013). The largest project development in planning to date is the TuNur project (2000 MW) (Berraho *et al.*, 2012).

South Africa is also about to enter the power tower industry with a 50 MW tower currently under construction in Upington called Khi Solar One (Abengoa, 2013).

### 1.1.3 SUNSPOT

Stellenbosch University has developed a combined power generation cycle, called Stellenbosch University Solar Power Thermodynamic cycle (SUNSPOT), which is a combined Rankine/Brayton cycle coupled by a heat storage unit (Kröger, 2012). The SUNSPOT cycle is depicted in figure 1.1.

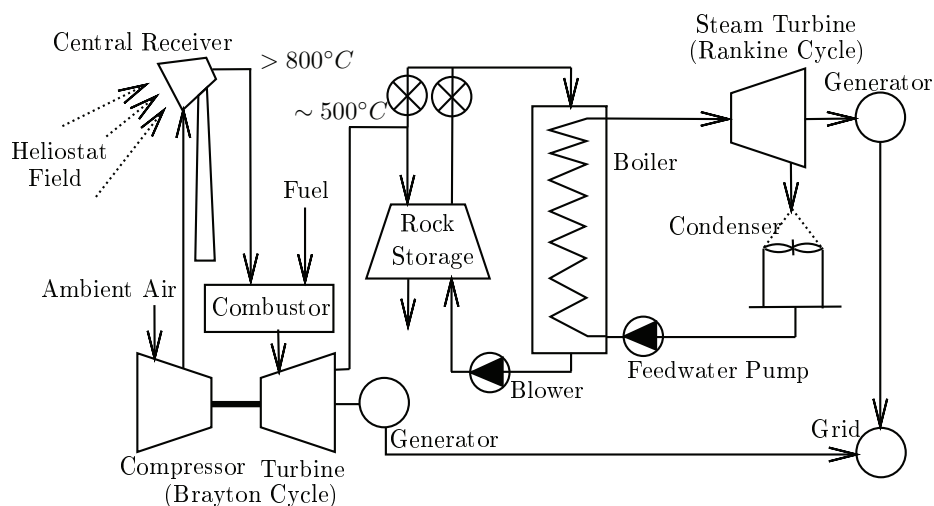


**Figure 1.1:** The Stellenbosch University Solar Power Thermodynamic cycle (Kröger, 2012)

The heat storage is comprised of a rock-bed with rocks typically found in the Northern Cape region of South Africa. For the Brayton cycle, ambient air is pressurized through the compressor stage to pressures of 15-20 bar. The pressurized air then enters the receiver and is heated to the desired fluid outlet temperature beyond 800 °C. The hot air is then further heated in the combustion chamber to the desired gas turbine inlet temperature. Consequently, the performance of the receiver has a direct impact on the energy requirement of the combustion unit. The air stream exiting the gas turbine is fed into the

storage unit which in turn provides a heat source for the Rankine cycle where steam is generated. The benefit of a combined cycle is that higher system efficiencies are obtained. The Brayton cycle operates at higher temperatures and the excess energy is used to fire the Rankine cycle at lower temperatures. When plotting the efficiencies, as depicted in figure 1.2, one can clearly see that

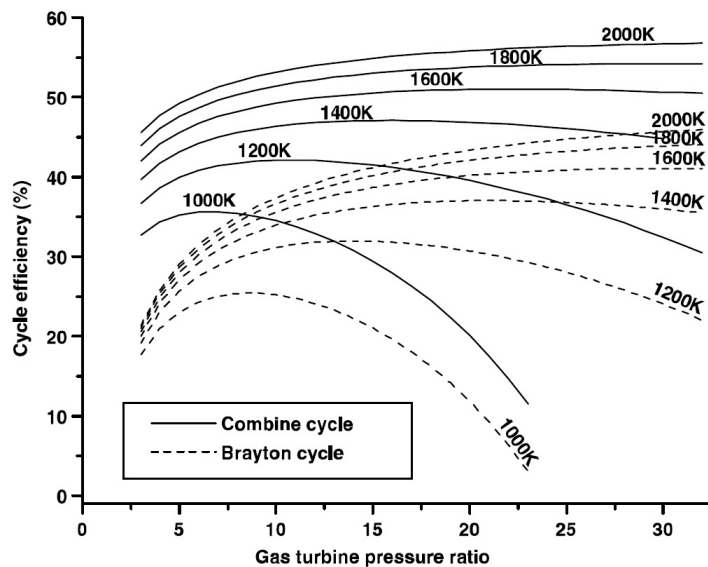


**Figure 1.2:** Illustration of cycle efficiency curves for combined cycle vs. Brayton cycle plotted against gas turbine pressure ratio (Segal and Epstein, 2003)

the benefit of a combined cycle is that higher cycle efficiencies are obtained at a lower pressure ratio compared to the conventional Brayton cycle or Rankine cycle.

## 1.2 Objective

The objective of this thesis is to design, model and empirically validate a receiver concept that can be used within a combined cycle power plant, such as the SUNSPOT cycle. The receiver concept should, therefore, make use of pressurized air as the heat transfer fluid. The objective is also to derive the receiver concept, based on an energy balance approach, where higher efficiencies are aspired.

Another objective for this study is to develop a scalable receiver design. For once, the receiver or certain components of the receiver are validated against empirical results. Since only small-scale flux concentrators were available, the receiver was designed at laboratory scale. A scalable receiver would have a significant advantage over current pressurized air receiver types, as current receivers have certain size limitations on some of their components. It is also

envisioned to develop a receiver concept with a less complex shape than contemporary pressurized air receivers (i.e., the elimination of a pressurized quartz window), which would then also have a direct implication on component cost. A recipient objective would be to design the receiver such that it could compensate for higher flux densities.

### 1.3 Methodology

The overall methodology of this study is to develop a receiver concept based on the energy balance approach, model it using numerical simulation tools and validate the numerical results. The development of the receiver concept requires an extensive review of state of the art receiver types and past experiences made in this field. Also, in order to understand the physical attributes involved in solar receivers, a parametric analysis is required to reveal the mathematical dependencies of energetic and exergetic terms. Further design investigations, such as the use of headers instead of tubes in series, are required to derive a potential receiver concept. The next step in the methodology is to finalize the concept based on these findings and define the limitations of the final receiver prototype with regards to this project. It is further required to develop a strategy where ray-tracing software and computational fluid dynamics (CFD) software are coupled so that the physics of the receiver concept can be effectively captured in the numerical model. The numerical model also needs to be compared with empirical results to test its validity. The methodology used in this project is to develop an optical numerical model of a small-scale solar concentrator using a ray-tracing tool, called SolTrace, and empirically characterise it with a flat plate cold water calorimeter, as published in Kretzschmar *et al.* (2012) and Mouzouris *et al.* (2012). Once the concentrator is characterised it can be used to validate the coupled ray-tracing and CFD model of the receiver. This approach ensures that each of the modelling tools is validated separately.

Finally, conclusions and recommendations can be made with respect to the numerical and empirical results.

### 1.4 Scope of Project

The scope of this project is restricted to investigating the fundamental idea of the receiver concept. Research is conducted by providing an extensive literature survey on different types of receivers, developing mathematical models relevant to the receiver analysis, conducting investigations with regard to design aspects that can potentially improve receiver performances and finally developing the receiver concept. The final prototype design of the receiver is beyond the scope of this project as the prototype is aimed to obtain fluxes

from a larger-scale heliostat field which has not been designed or constructed yet. The project only addresses the unique features of the receiver concept, namely the investigation of the reverse air flow and the effect of using quartz as a potential radiation shield.

## 1.5 Structure of Document

The document consists of eight chapters. Each chapter can be briefly outlined as follows:

- Chapter 1: The introduction consists of a broad background on solar thermal power stations, narrowed down to a short description of the history of power towers followed by the introduction of the SUNSPOT cycle, the thesis objective, thesis motivation and the scope of this project.
- Chapter 2: This chapter forms the literature study of the thesis where various receiver technologies relevant to this project have been reviewed. The review starts with external tube receivers, cavity receivers, volumetric receivers and ending with miscellaneous types of receivers that have emerged over the last few years.
- Chapter 3: The parametric analysis in chapter 3 presents the energy balance equation, the concept of entropy generation and exergy destruction, which are the most important thermodynamics relations for a receiver system. The chapter also highlights results obtained after investigating certain effects that might contribute to higher efficiencies.
- Chapter 4: Based on the knowledge gained from the previous chapters, this chapter presents the Hybrid Pressurized Air Receiver (HPAR) concept. It highlights the selected materials suitable for the concept followed by the expected benefits and potential drawbacks of the idea.
- Chapter 5: This chapter presents the model used in the ray-tracing analysis accompanied with the ray-tracing results.
- Chapter 6: The coupled natural convection and radiation chapter presents the theory background on buoyancy-driven flow and radiation transfer and how this is modelled, followed by a discussion on flux mapping strategies between a ray-tracing tool and the CFD software. Then the modelling setup of a HPAR module is outlined followed by the numerical results thereof.
- Chapter 7: This chapter provides a comparison between the numerical results from chapter 6 and experimental work done using the characterised solar concentrator that was presented in appendix D.



- Chapter 8: The last chapter provides the overall conclusions and a summary of the research contribution in terms of publications. Finally, a recommendation on the road forward is briefly highlighted.

# Chapter 2

## Literature Review

This section provides a brief overview of the types of receivers that have been developed including external tube receivers, cavity receivers, volumetric receivers, small-particle receivers and new emerging concepts.

### 2.1 Introduction

For central receiver systems the receiver has the purpose of intercepting and converting the incident solar light into thermal energy and passing it onto the heat transfer fluid. The receiver is typically situated at the top of the central receiver tower. Over the years many different receiver concepts have been developed. These can generally be classified as directly-irradiated or indirectly-irradiated receivers (Ávila Marín, 2011). Directly-irradiated receivers utilize a working fluid such as air that is actively taking part in the absorption of incident sunlight as it is directly exposed to the incident radiation (Romero-Alvarez and Zarza, 2007). For indirectly-irradiated receivers, however, the working fluid is contained in a fixed and opaque absorber structure such that the working fluid is only indirectly exposed to the sunlight. The hybrid pressurized air receiver is the first air receiver concept that is, in fact, a combination of both types.

### 2.2 External Tube Receiver

External tube receivers are the oldest and most mature receiver technologies. They have been studied and developed over the last 30 years and have also been tested at numerous solar tower plants worldwide (Pacheco *et al.*, 2000; Romero *et al.*, 2002; Romero-Alvarez and Zarza, 2007; Meduri *et al.*, 2010). This technology was adapted from the well-established boiler manufacturing industry which is a proven and safe technology to use, especially since most external tube receivers were part of prototype projects (Grasse *et al.*, 1991; Winter *et al.*, 1991). Studies on boiler tubes have been extensively found in

literature (Reynolds, 1963; Gartner *et al.*, 1974; Faghri and Welty, 1978; Shub, 1993; Yu-ting *et al.*, 2009; Naphon, 2011; Yang *et al.*, 2012).

First generation external tube receivers used steam as the heat transfer fluid. The next generation switched to molten salt due to its excellent thermal conductivity (0.52 W/mK), heat capacity (1.6 kJ/kgK) and low vapour pressure. Therefore, the receivers could accommodate higher solar flux densities than 800 kW/m<sup>2</sup> (Pacheco *et al.*, 2000). Molten salt, additionally, remains liquid at lower pressures compared to steam or pressurized air. Hence, the tube thickness can be reduced which further enhances the heat transfer to the working fluid. Some challenges remain for molten salt systems due to the solidifying of the liquid at temperatures below 220 °C. Common leakages and the replacement of parts such as valves, header pipes etc. further cause significant down-times.

The benchmark performance of external tube receivers, at the time, was investigated during the commissioning phase of the Solar One tower (Winter *et al.*, 1991). The receiver was designed for a direct steam plant at 516 °C at 100 bar (Radosevich and Skinrod, 1989). The thermal efficiency of the receiver initially was at 77 % for an absorbed power of 34 MW<sub>t</sub>, but increased to 82 % after painting and curing the absorber surface (Pacheco *et al.*, 2000). The losses experienced were primarily due to radiation losses and throttling the mass flow rate to operate the receiver at constant temperature (Radosevich and Skinrod, 1989). Problems experienced during the testing phase included overheating and deformation of the tubes at the superheating section (Radosevich and Skinrod, 1989). Also, especially during start-up and shut-down phases, significant temperature gradients of up to 111 °C was experienced between the ends and centre of the tubes (Romero-Alvarez and Zarza, 2007). As a result start-up and shut-down procedures had to be executed slowly with high caution, at the expense of efficiency drop. The problems associated within the superheating section were removed in the Solar Two project where direct steam was replaced with molten salt. The Solar Two molten salt receiver recorded efficiencies of up to 88 %, where molten salt was heated from 220 °C to 565 °C at an absorbed power of 34 MW<sub>t</sub> (Pacheco *et al.*, 2002).

Generally, external tube receivers benefit from being capable of using surround heliostat fields. They are also applicable to multiple heat transfer fluids. Their drawback, however, is that they can accommodate high temperature (up to 1000 °C) or high pressure (120 bar), but not both (Kribus, 1999). Also, they generally cannot operate at higher fluxes than 600 kW/m<sup>2</sup>, unless heat transfer fluids such as liquid sodium are used (Romero-Alvarez and Zarza, 2007). The efficiency of external tube receivers leaves room for improvement.

## 2.3 Cavity Receiver

Cavity receivers are developed from their predecessors, the external tube receiver, which, apart from their geometric shape, have few differences. They consist of tube panels located in well insulated enclosures to efficiently absorb the incident sunlight (Suter, 2012; Sparrow and Cess, 1978). Various studies have considered changing the geometric shapes of the enclosures (Harris and Lenz, 1985; Paitoonsurikarn and Lovegrove, 2003; Jilte *et al.*, 2013), and also investigated the effect of different inclination angles (Taumoefolau and Lovegrove, 2002; Jilte *et al.*, 2013).

Cavity receivers have higher efficiencies than external tube receivers due to lower convection and reradiation losses. The low convection losses are obtained since stagnation zones occur within the cavity and thus hot convection air plumes are less likely to escape from the receiver (Prakash *et al.*, 2010). Studies on convection heat losses in solar cavity receivers have been extensively reviewed in Wu *et al.* (2010). Also, reradiation losses are minimized as the aperture area is smaller relative to the absorber surface area (Li *et al.*, 2010). Cavity receivers further benefit from a higher apparent absorptance due to multiple reflections occurring within the cavity (Suter, 2012). Apparent absorptance is termed the fraction of energy flux emitted by a blackbody surface stretched across the cavity opening that is absorbed by the cavity opening (Maag *et al.*, 2011). In cavity receivers some of the absorber panels (e.g. side panels, top panels and bottom panels) do not face normal to the incident solar irradiation. As a result the heat flux density is more effectively distributed and more uniform wall temperatures are obtained (Fang *et al.*, 2011; Montes *et al.*, 2011; Yu *et al.*, 2012; Teichel *et al.*, 2012).

A drawback of current cavity receiver types include the fact that no surround heliostat field can be utilized. This deficit however can be overcome by means of modular receiver designs (Schmitz *et al.*, 2006). The first modular cavity power tower was constructed in California in 2009, called Sierra Sun Tower (5 MW<sub>e</sub>), which is a dual-cavity receiver (Tian and Zhao, 2013). Another one currently under construction at Upington (South Africa), called Khi Solar One, consists of three cavity receivers, facing to the south, west and east direction (Abengoa, 2013). The Khi Solar One tower is illustrated in figure 2.1.

All large-scale (MW sizes) cavity receivers built to date make use of either molten salt or direct steam as the heat transfer fluid. Recent studies, however, have also investigated the application of tubular cavity receivers in pressurized air cycles. These include the Solar Hybrid Power and Cogeneration Plants (SOLHYCO) project, Production of Electricity by Gas turbine and Solar Energy (PEGASE) project (France) and the tube receiver at the Commonwealth Scientific and Industrial research Organisation (CSIRO) in Australia (Amsbeck *et al.*, 2010; Grange *et al.*, 2011; Daguene-Frick *et al.*, 2013; Stein *et al.*, 2010). Pressurized air receivers with tubular technologies remain attractive

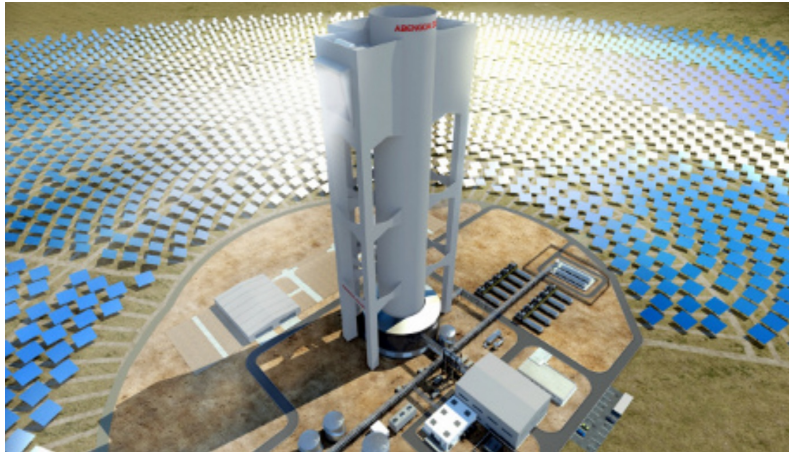


**Figure 2.1:** Modular cavity receiver under construction at Khi Solar one, Upington, South Africa (Source: Abengoa (2013))

due to their simplicity and flexibility for scale-up and are also more likely to have lower cost than volumetric pressurized air receivers (Soo Too and Benito, 2013).

Test experiences for the SOLHYCO project have shown that receiver efficiencies of 39.7% with open aperture and 43% with the quartz window configuration were achieved (Amsbeck *et al.*, 2010). Fluid outlet temperatures of 800 °C were obtained. The simulated efficiency values however were predicted much higher with 67.7% for the open configuration and 80.8% for closed configuration (Amsbeck *et al.*, 2009). Amsbeck *et al.* (2009) reasoned that the significant difference between the simulations and the empirical results is due to design flaws of the cavity structure (poor insulation material and weak external mounting structure causing air gap leakages) and mass flow leakages at the turbine.

For the PEGASE project and the 200 kW<sub>e</sub> tube receiver at the CSIRO no experimentally recorded figures of efficiencies have been published to date.

## 2.4 Volumetric Receiver

Volumetric receivers, mostly developed in Europe and Israel over the last 20 years, are classified as directly-irradiated receivers (Ávila Marín, 2011). The operating principle is based on air being forced through a porous wire-mesh or ceramic foam, where the porous material is exposed to the incident solar flux. The air itself is also exposed to the incident flux and thus direct absorption is obtained (Romero and Steinfeld, 2012). The air flow can either be pressurized using a quartz window or be at ambient conditions.

Volumetric receivers, in general, are more efficient than tubular receivers. Their efficiencies were documented to reach up to 80% at temperatures in

the vicinity of around 1200 °C (Ávila Marín, 2011). These high efficiencies are obtained because of direct absorption and the surface temperature at the frontal absorber section being lower than the final air outlet temperature. Cold (or relatively cold) air enters the absorber material and cools down the frontal cells. The porous absorber foam further allows sunlight to penetrate deeper into the volumetric foam structure and thus reflection, convection and reradiation losses are minimized. This effect has been investigated in numerous studies and is termed the *volumetric effect* (Wu *et al.*, 2011; Villafán-Vidales *et al.*, 2011; Fend *et al.*, 2004*a,b*).

Pressurized closed volumetric receivers have set the benchmark of the highest achievable temperatures and efficiencies. The Directly-Irradiated Annular Pressurized Receiver (DIAPR) 30-50 receiver recorded fluid outlet temperatures of 1200 °C, a thermal efficiency of 71 % and pressure of 20 bar (Kribus *et al.*, 2001; Karni *et al.*, 1998). This receiver uses a fused-silica window to maintain the pressurized operating conditions and a so called 'porcupine' volumetric absorber. Although experimentation of this receiver type has only been conducted on laboratory scale to date upscaled projects are expected to commence soon.

The Receiver for Solar Fossil Power Plants (REFOS) showed similar results during the Solgate project where fluid outlet temperatures of 960 °C was obtained at 70 % thermal efficiency (Buck *et al.*, 2002). The REFOS makes use of a dome-shaped quartz window, a thin SiC porous absorber cup and a compound parabolic concentrator (CPC). Figure 2.2 shows a schematic diagram of the REFOS developed for the Solar Hybrid Gas Turbine Electric Power System SOLGATE (2005) project.

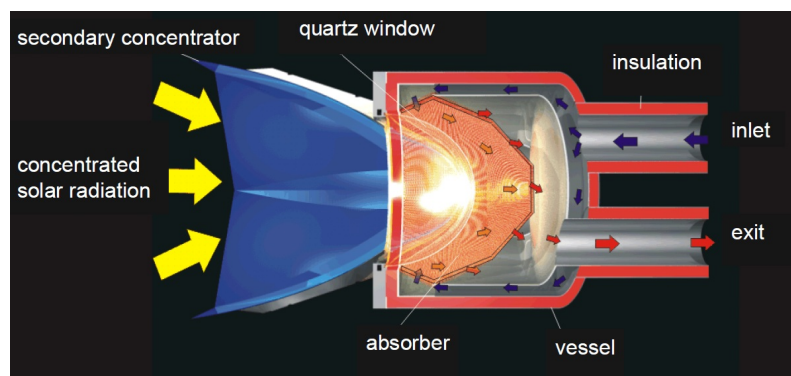


**Figure 2.2:** Pressurized volumetric receiver as developed for the REFOS project Heller *et al.* (2006)

The use of pressurized quartz windows pose several problems including sensitivity to thermal shock, size limitation, thickness constraint and low resistance to high pressures and temperatures. Quartz windows can only tolerate temperatures of around 800 °C under pressurized conditions and thus require

active cooling at higher fluxes. They also require thorough cleaning maintenance as severe dust deposition may cause excessive radiative absorption and thus overheating (Lipinski *et al.*, 2009). Pressurized quartz windows also involve high costs, especially the domed-shaped window profile. Hence, the latest receiver developments consider alternative designs without the use of a quartz window.

Volumetric receivers without the use of quartz windows are typically termed open volumetric receivers. Open volumetric receivers operate with air at ambient pressure and are thus only applicable to the Rankine cycle, where the hot air is passed through a steam generator (Ávila Marín, 2011). It cannot be fed directly into a gas turbine for use in a Brayton gas cycle, because a gas turbine requires the use of pressurized air.

Research and development on open volumetric receivers have been initiated in the early 1990s of which the largest prototype receiver was the PHOEBUS-TSA (Technology Program Solar Air Receiver) with power levels of up to  $3\text{ MW}_t$ . PHOEBUS-TSA was tested at the Plataforma Solar de Almeria (PSA) (Koll *et al.*, 2009; Grasse, 1991; Meinecke and Cordes, 1994; Hoffschmidt *et al.*, 2003).

The first open volumetric receiver power tower was constructed at Jülich (Germany) with a size of  $1.5\text{ MW}_e$ . It started operation in March 2009 (Koll *et al.*, 2009) with the aim of demonstrating the potential of the open volumetric receiver technology at larger scale. The next tower utilizing this technology is planned to be built in Algeria with a size of  $7\text{ MW}$  (Koll *et al.*, 2011).

Limitation of this receiver type include the fact that ambient air is used. Ambient air has poor thermal properties compared to pressurized air or other liquid heat transfer fluids. The density and heat capacity of air further decrease as the air temperatures increases and therefore worsens the case. Hence, the open volumetric receiver can only sustain a certain amount of irradiation before material failure occurs (Becker *et al.*, 2006). The material failure is also influenced by the pressure drop versus depth through the porous medium (Kribus *et al.*, 1996). It was found that the absorber surface would fail if not sufficient mass flow via pressure drop is ensured, especially at the centre of the receiver aperture where maximum solar flux is experienced; while much less pressure drop is required at the sides, close to the rims. This gives rise to a complicated control system problem (Ahlbrink *et al.*, 2010).

The technical issues involved with higher flux densities and flow instability inhibit the open volumetric receiver technology from rolling out to larger systems at commercial scale (Ávila Marín, 2011).

An improved concept of the open volumetric receiver has been proposed by Pitz-Paal *et al.* (1991) where matrices of square quartz glass channels are placed in front of the ceramic foil absorbers. This concept illustrates the same fundamental idea which the receiver concept presented in this project, is based on, namely to generate a convection but also a radiation trap. The quartz glass channels are transparent to the incident sunlight while absorbing some of the

thermal radiation emitted back from the absorber foil. Therefore some of the reradiation losses are captured. The study showed that an efficiency increase of up to 10 % can be expected (Pitz-Paal *et al.*, 1991). Furthermore, higher fluid outlet temperatures are obtained since the radiation absorbed within the quartz glass is transferred to the air. The quartz glass structure also assist in stabilising the air flow patterns. Over the last two decades no further research on this concept was done.

An alternative receiver concept, proposed by Buck *et al.* (2006) is the dual receiver concept, which is an open volumetric air receiver with evaporator tubes located in front of the receiver aperture. In the described system steam is generated not only by the hot air from the open-volumetric receiver that passes through the steam generator but also inside the evaporator tubes. The evaporator tubes are additionally used to cool down the porous material at the frontal receiver aperture. Reradiation and convection losses are therefore reduced.

The dual receiver concept showed an increase of 27 % in the annual electricity production, compared to the typical open volumetric receiver concept (Buck *et al.*, 2006). An illustration of the receiver concept is depicted in 2.4.

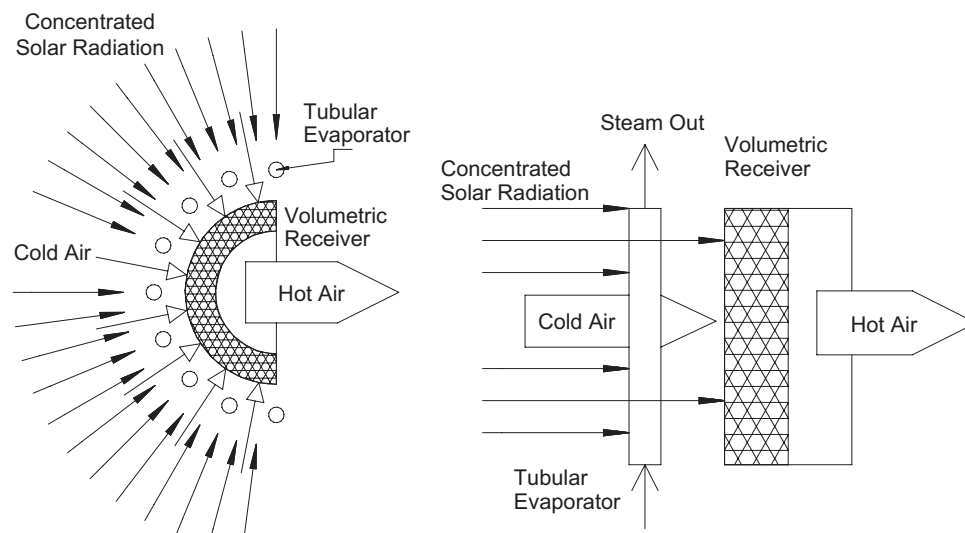


**Figure 2.3:** Dual receiver concept (Buck *et al.*, 2006)

## 2.5 Small Particle Receiver

In small particle receivers the concentrated solar irradiation is absorbed by small particles entrained in a gas stream (Hunt and Miller, 2010; Ruther and Miller, 2010). As the particles gain thermal energy through absorption they simultaneously heat up the bulk gas mixture. Oxidation occurs and the hot gas



stream is then typically fed into a Brayton cycle to generate electricity. These receivers can also be used for hydrogen production or other thermo-chemical processes. Solid particle receivers have been extensively reviewed by Tan and Chen (2010), and they have great potential of becoming the next generation receiver type (Zanganeh *et al.*, 2012; Behar *et al.*, 2013).

Although it might seem a very promising technology many inherent technical problems need to be overcome, most of them involving the problems associated with the use of a quartz window, as discussed in section 2.4.

## 2.6 Emerging New Receiver Concepts

### 2.6.1 Reticulate Porous Ceramic Pressurized Air Receiver

A novel receiver concept, proposed by Lipinski *et al.* (2009), called the Reticulate Porous Ceramic (RPC) pressurized air receiver, consists of a reticulate ceramic absorber foam bounded by two concentric cylinders. This concept is more robust and less complex when compared to the closed volumetric air receiver. The prevention of the use of a quartz window is a result of a more simplistic design. It is therefore also classified as an indirectly-irradiated receiver. The receiver obtained an air outlet temperature of 1000 °C at 10 bar and an efficiency of 78 % (Lipinski *et al.*, 2009).

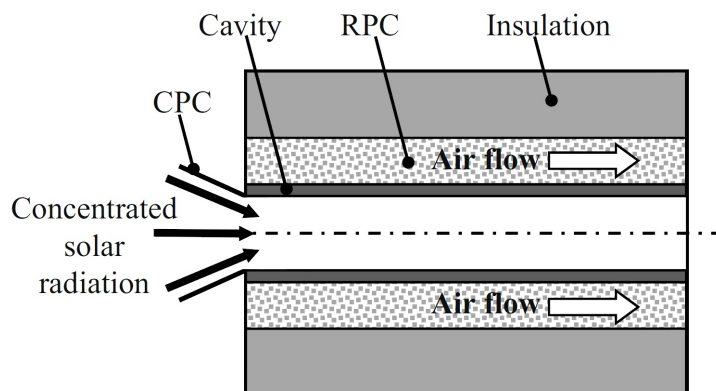


Figure 2.4: Reticulate porous ceramic receiver concept (Hischier, 2011)

### 2.6.2 Hex-Pyramid Receiver

The hex-pyramid receiver consists of multiple hexagonal pyramid-shaped absorber elements distributed in a honeycomb fashion around the cylindrical

tower, which reminds of a 'waffle iron'. The receiver is comparable to an external tube receiver, however, with higher efficiencies. The pyramid shaped elements provide a radiation trap, compared to fully exposed tube elements. The convection losses are also minimized as forced convection is reduced at the depth of the elements. Bifurcation of the pyramid edges further reduce the convection losses (Garbrecht *et al.*, 2012).

This receiver concept is intended to use molten salt as heat transfer fluid. Any heat transfer fluid however can be chosen since it is confined in walls. Preliminary numerical studies have estimated the receiver's efficiency at 91.2% (Garbrecht *et al.*, 2012). The result was compared to the molten salt receiver of Solar Two which ranges between 85.62% and 88% (Pacheco *et al.*, 2002).

## 2.7 Conclusion

The review showed that tubular receivers are favoured over other receiver types due to their proven technology. Aspects such as reliability, simple geometry and applicability to surround heliostat fields are factors that contribute to their success, but there is room for improvement on efficiency. The efficiency in tubular receivers can be increased with steam or molten salt, but issues such as drainage schemes, leakages at fittings and hot spots, make this approach also not completely flawless. The study revealed that cavity receivers are potentially a better solution than external tube receivers from an efficiency perspective, but with the drawback of not being able to use a surround field. Tubular air receivers generally lack efficiency and allowable flux densities, which in turn increase the size of the receivers for given flux input. Therefore, volumetric receivers potentially provide a better solution for this type of heat transfer fluid. Research revealed that volumetric receivers are not yet optimal. Complexity, material failure, size limitation and cost inhibit pressurized volumetric receivers using quartz windows from commercialization. Open volumetric receivers, on the other hand, are limited by their restricted use in the Rankine power cycle. An update on new emerging receiver concepts was also presented. Chapter 3 further presents a parametric analysis where the energy balance and exergy balance are used to reveal means of improving a receiver design.

# Chapter 3

## Parametric Analysis

### 3.1 Introduction

The parametric analysis presented in this chapter considers fundamental mathematical formulations to investigate sensitivities that can improve a receiver concept. Factors influencing the energy balance equation are extensively considered, and the concept of entropy generation and exergy destruction are highlighted. The implication of choosing air as the heat transfer is outlined compared to other heat transfer fluids. Finally, additional design aspects such as the effect of a header system are investigated.

### 3.2 Energy Balance

The conservation of energy principle states that energy can neither be generated nor destroyed during a process (Cengel, 2006). For this reason, an energy balance equation is set where the total energy entering a system less the total energy exiting a system will give the total change in energy within the system.

$$E_{\text{in}} - E_{\text{out}} = \Delta E_{\text{sys}} \quad (3.1)$$

Energy transfer can occur by heat transfer ( $Q$ ), work transfer ( $W$ ) and mass transfer ( $E_m$ ). Heat transfer occurs following a temperature difference between a system and its surroundings, whereas work transfer occurs as the result of a force displaced over a distance (e.g., spring work or shaft work) or electrical work performed (Cengel, 2006). Mass transfer adds or removes energy to a system as energy is accompanied with a body of mass. The energy equation can be expanded to a general form as shown,

$$E_{\text{in}} - E_{\text{out}} = Q_{\text{in}} - Q_{\text{out}} + W_{\text{in}} - W_{\text{out}} + E_{\text{m,in}} - E_{\text{m,out}} \quad (3.2)$$

If steady state is obtained, the change in energy within the system is zero, and equation 3.2 can be rearranged as follows:

$$\dot{Q}_{\text{in}} + \dot{W}_{\text{in}} + \sum_{\text{in}} \dot{m} \left( h + \frac{V^2}{2} + gz \right) = \dot{Q}_{\text{out}} + \dot{W}_{\text{out}} + \sum_{\text{out}} \dot{m} \left( h + \frac{V^2}{2} + gz \right) \quad (3.3)$$

For a receiver energy system, kinetic and potential energy terms are typically zero. Also, no work interactions occur within the receiver control system as work is only executed at the compressor and turbine stage. Therefore, equation 3.4 is obtained after simplifying, where  $\alpha$  denotes the absorptivity coefficient and  $h$  the enthalpy of the working fluid. The absorptivity coefficient is the fraction of solar light absorbed by the receiver, and thus also indicates the amount of reflection losses experienced.

$$\alpha \dot{Q}_{\text{in}} + \sum_{\text{in}} \dot{m} h = \dot{Q}_{\text{rad}} + \dot{Q}_{\text{conv}} + \sum_{\text{out}} \dot{m} h \quad (3.4)$$

Heat transfer occurs in three different modes; radiation, convection and conduction. Conduction, however, has less influence on the energy exchange of the system if the entire receiver is considered as a control volume. The most general form of radiation is given by equation 3.5.

$$\dot{Q}_{\text{rad}} = \epsilon A_{\text{ap}} \sigma F_{\text{kj}} (T_{\text{s}}^4 - T_{\text{amb}}^4) \quad (3.5)$$

where,

$\epsilon$  = emissivity

$A_{\text{ap}}$  = surface area of emitting body

$\sigma$  = Stefan-Boltzmann constant

$F_{\text{kj}}$  = configuration factor

$T_{\text{s}}$  = surface temperature of emitting body

$T_{\text{amb}}$  = temperature of environment

Energy transfer due to convection occurs if a change in temperature between the surface of the body and the surrounding air is experienced. For receiver applications convective heat transfer typically occurs from the body to the air. As a result, the air particles gain the thermal energy from the body as they sweep past the body. The general equation for convective heat transfer is given by 3.6

$$\dot{Q}_{\text{conv}} = h_{\text{c}} A_{\text{ap}} (T_{\text{s}} - T_{\text{amb}}) \quad (3.6)$$

The convection heat transfer coefficient, depicted as  $h_{\text{c}}$ , is calculated from

$$h_{\text{c}} = \frac{k \text{Nu}}{L} \quad (3.7)$$

where  $k$  is the thermal conductivity, Nu the Nusselt number and  $L$  the characteristic length of the body. Convection typically occurs as either an internal forced convection, external forced convection or natural convection.

### 3.3 Entropy Generation

The first law of thermodynamics states that energy can neither be created nor destroyed. It can only shift from one form to another. The first law, however, cannot specify in which direction the process takes place. Therefore there is the second law of thermodynamics, given by the Clausius inequality (equation 3.8), and the thermodynamic property called entropy.

$$\oint \frac{\delta Q}{T} \leq 0 \quad (3.8)$$

Entropy is typically defined as the measure of irreversibilities that take place during a process. If the irreversibilities are high the quality of energy is low. Entropy therefore also reveals what the quality of energy is compared to an energy balance where only quantitative energy terms are considered. For example, energy at higher temperatures has higher quality than the same amount of energy at lower temperatures, even though the quantity in terms of kilojoules remains the same. From this discussion it is clear that receiver systems should aim to increase the temperature of the fluid such that a higher energetic quality is obtained.

### 3.4 Exergy Balance

The maximum useful work that can be obtained from a system at a given state is defined as exergy, which is also termed availability (Cengel and Boles, 2007). Similarly, reversible work is the maximum useful work that can be obtained as a system undergoes a process between two specified states. If the process occurs without any irreversibilities from the initial state to the dead state, the magnitude of the reversible work is equal to the exergy at the initial state. In other words, exergy is not what the system will actually produce. It merely provides the upper limit of the useful work that can be produced without violating any thermodynamic laws. Additionally, exergy depends on the condition of the environment. If the dead state (process reached equilibrium with the environment) is lowered, more useful work can be obtained.

In practice, entropy cannot be destroyed. It can only be generated. Entropy generation, however, is proportional to exergy destruction. Exergy destruction is always greater than zero for irreversible processes and equal to zero for reversible processes, as depicted by equation 3.9.

$$\dot{X}_{\text{dest}} = T_o \dot{S}_{\text{gen}} \geq 0 \quad (3.9)$$

Exergy destruction occurs in processes due to friction, mixing, chemical reactions, heat transfer from a finite temperature difference, unrestrained expansion, non-quasi equilibrium compression and expansion (Cengel and Boles, 2007). The general exergy balance equation is given by 3.10.

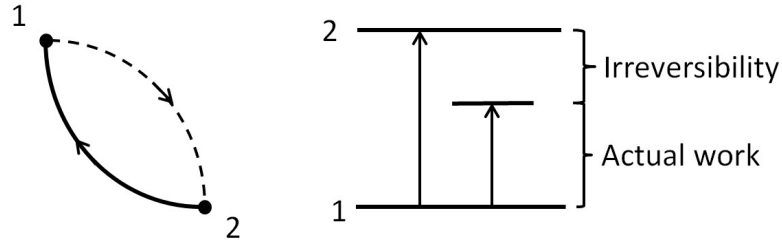


**Figure 3.1:** Conceptual illustration of reversible cycle, irreversibility and actual work (Cengel, 2006)

$$\sum \left(1 - \frac{T_o}{T_k}\right) \dot{Q}_k - \left(\dot{W} - P_o \frac{dV}{dt}\right) + \sum_{\text{in}} \dot{m}\psi - \sum_{\text{out}} \dot{m}\psi - \dot{X}_{\text{dest}} = \frac{dX_{\text{cv}}}{dt} \quad (3.10)$$

where  $\psi_{\text{in}} - \psi_{\text{out}}$  can be written as

$$\psi_{\text{in}} - \psi_{\text{out}} = (h_{\text{in}} - h_{\text{out}}) - T_o(s_{\text{in}} - s_{\text{out}}) + \frac{V_{\text{in}}^2 - V_{\text{out}}^2}{2} + g(z_{\text{in}} - z_{\text{out}}) \quad (3.11)$$

and the subscript o depict conditions at the dead state and k at the system's boundary respectively (Cengel and Boles, 2007). Equation 3.10 compared to 3.4 not only accounts for heat transfer to and from the receiver system but also the temperature difference between the receiver and its surroundings. Moreover, the effect of pressure variation between the two states is accounted by the term  $P_o dV/dt$ , which shows that the exergy balance not only considers energetic terms but also the effect of pressure drop. The work performed in this project considered the exergy balance but primarily focuses on the terms in the energy balance equation.

## 3.5 Parametric Analysis on System Efficiency

### 3.5.1 Effect of Solar Concentration Ratio

In the previous section it was demonstrated that based on the second law of thermodynamics higher temperatures are directly related to a better quality of energy and thus higher efficiency. CSP systems provide higher concentrations by mirrors that redirect the solar light to an absorbing surface, which gives rise to a certain concentration ratio. The concentration ratio (CR) is defined as the collector area divided by the absorbing area (Romero-Alvarez and Zarza, 2007).

$$C = \frac{A_c}{A_{\text{abs}}} \quad (3.12)$$

The concentration ratio is often referred to as a certain number of 'suns' (Hischier, 2011). The term originated in systems where absorber surfaces and collector unit surfaces had similar sizes. As a result, the concentration ratio is typically a factor of the number of collector surfaces used (e.g. 200 mirrors provide 200 suns), where each collector adds a 'sun' image onto the absorber surface.

A macro sensitivity analysis was performed to investigate the effect of the concentration ratio on a receiver system. Here, the size of the collector area and absorber surface area were set equal in order to simplify the analysis. Also Kretzschmar and Gauché (2012) have shown that radiation losses are more dominant than other energy terms within the high temperature range, as depicted in figure 3.2.

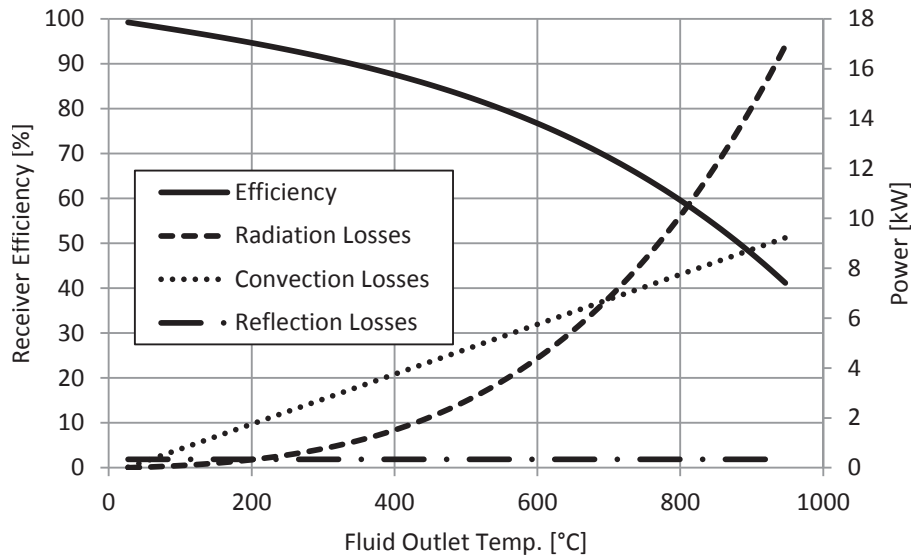


**Figure 3.2:** Plot of the receiver efficiency versus radiation, reflection and convection losses from a typical cavity receiver (Kretzschmar and Gauché, 2012)

It was therefore decided to first consider radiation losses at this stage and include the effect of convection in section 3.5.3. Conduction losses were neglected. Since reflection losses depict a percentage loss of the incident flux, these losses were also neglected. Based on these simplifying assumptions, an energy balance was set up as follows (Romero-Alvarez and Zarza, 2007),

$$\frac{Q_u}{A} = \alpha C \phi - \sigma \epsilon F (T_s^4 - T_{\text{amb}}^4) \quad (3.13)$$

In this equation  $Q_u$  denotes the useful energy absorbed,  $A$  is the unit collector and absorber area set to unity,  $\phi$  is the solar direct normal irradiance (DNI) in  $W/m^2$  and  $F$  is the aggregated radiation view factor of the absorber with respect to the surroundings.  $\alpha$  and  $\epsilon$  depict the hemispherical absorptivity and emissivity values respectively. The sensitivity of receiver efficiency with concentration ratio can be formulated by noting that  $\eta_{rec} = Q_u/(AC\phi)$ .

$$\eta_{rec} = \alpha - \sigma\epsilon F \frac{(T_s^4 - T_{amb}^4)}{C\phi} \quad (3.14)$$

The Carnot efficiency for a heat engine is given by equation 3.15.

$$\eta_{t,Carnot} = 1 - \frac{Q_u}{Q_{in}} = 1 - \frac{T_{max}}{T_o} \quad (3.15)$$

and the system's efficiency is given by

$$\eta_{t,sys} = \left(1 - \frac{T_{max}}{T_o}\right) \left(\frac{Q_u}{Q_{in}}\right) \quad (3.16)$$

$T_{max}$  denotes the highest temperature in the cycle and  $T_o$  the lowest temperature. Figure 3.3 shows the results obtained by plotting surface temperatures from the ambient temperature at  $20^\circ C$  to  $1400^\circ C$  using equation 3.14.

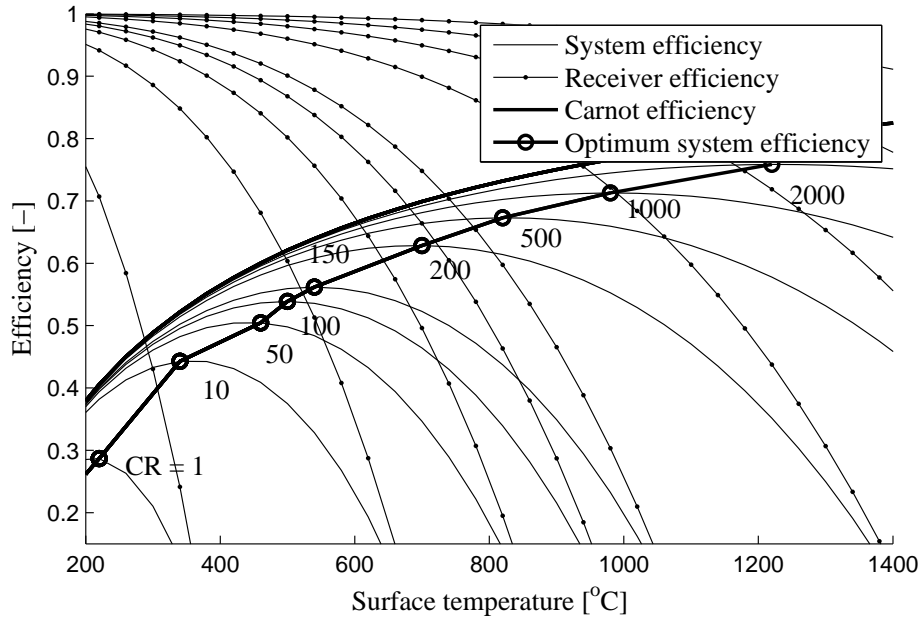


**Figure 3.3:** Thermodynamic efficiency curves for range of concentration ratio

The Carnot efficiency and system efficiencies are plotted using equations 3.15 and 3.16. The figure illustrates the sensitivity of the increase in concen-



tration ratio on the three efficiency curves. The concentration ratio was ranged between 1 and 2000, as shown in figure 3.3.

A DNI value of  $1000 \text{ W/m}^2$  was chosen with  $F = \epsilon = \alpha = 1$ . An aggregated view factor of 1 is similar to what external tube receivers typically experience. These plots therefore illustrate that, to obtain a maximum temperature of  $1000^\circ\text{C}$  at the turbine inlet, at least 1000 suns are required. Note that convection losses are not included at this stage. Also note that for every CR, there exists an optimum point where higher system efficiencies can be obtained at higher temperatures. This is because higher temperatures reduce the receiver efficiency and the overall system's efficiency. This optimum point should be defined as the system's operating point, and the concentration ratio should be specified such that the optimum operating temperature meets the required turbine inlet temperature.

Figure 3.3 also suggests that, in order to increase the overall system efficiency, the concentration ratio should be increased to obtain higher temperatures.

### 3.5.2 Effect of Absorptivity and Emissivity Coefficients

The effect of absorptivity and emissivity values reveals the importance of a good selective coating. The selective coating should ideally be able to absorb all the energy (high absorptivity) and emit none (low emissivity). In this case, all the energy is contained in the tube, and high temperatures are obtained. The coating used for the experiments in chapter 5 is carbon black paint (NS-7), which has an absorptivity of 0.96 and emissivity of 0.88 (Pompea and Breault, 1995). NS-7 was chosen for its high temperature tolerance and good absorption properties. The absorption properties are typically represented by an aspect ratio of absorptivity versus emissivity. The aspect ratio for NS-7, for example, is 1.07.

A sensitivity analysis on the stagnation temperature was performed by ranging the concentration ratio from 1 to 500 for different aspect ratios between 0.5 and 1.5, as shown in figure 3.4. The stagnation temperature is defined as the maximum surface temperature experienced by the absorber structure. No energy transfer via a working fluid is induced. Here, equation 3.17 was used, which was obtained by setting the absorbed power in the general equation to zero and rearranging it.

$$T_{s,\max} = \left[ \frac{\alpha C \phi}{\epsilon \sigma} - T_{\text{amb}}^4 \right]^{1/4} \quad (3.17)$$

The results show that the selective coating has a significant impact on the stagnation temperature. For instance, at 300 suns the surface temperature of the absorber can be increased from  $1000^\circ\text{C}$  to almost  $1400^\circ\text{C}$  with aspect ratios ranging from 0.5 to 1.5. The plot also shows that 150 suns are sufficient to theoretically achieve  $1000^\circ\text{C}$  stagnation temperature when using NS-7 paint.

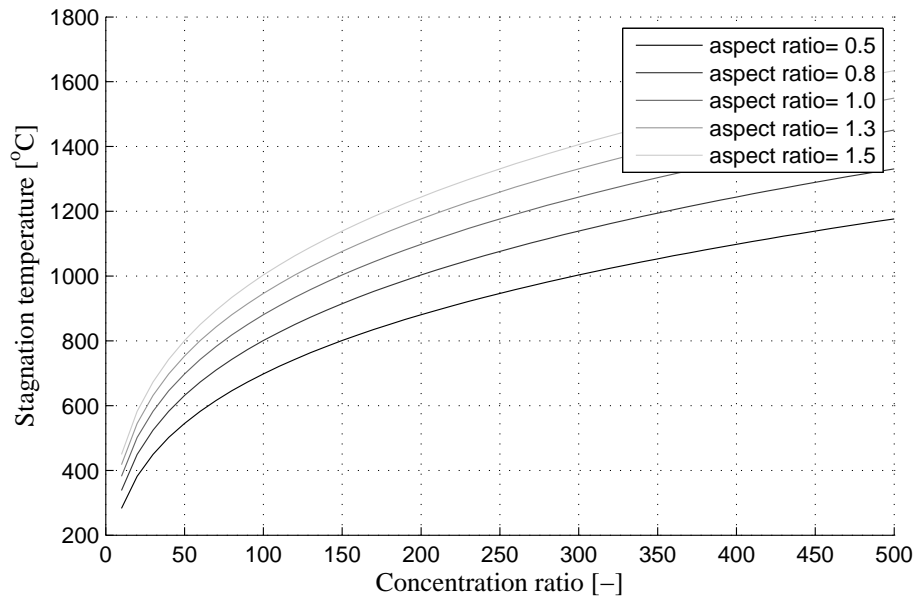


**Figure 3.4:** Stagnation temperature plot versus concentration ratio for increase in aspect ratio at a DNI of  $1000 \text{ W/m}^2$

### 3.5.3 Effect of View Factor and Convective Heat Transfer Coefficient

Figure 3.3 shows that for a typical external receiver with an aggregated view factor of 1, a concentration ratio in the vicinity of 2000 suns is required to obtain temperatures close to  $1000 \text{ }^\circ\text{C}$ . If the view factor can be reduced, the concentration ratio, i.e., number of heliostats required, can be significantly reduced for the same output.

This argument forms the basis on which cavity receivers are proposed. The view factor of a backwall (typically the hottest wall inside a cavity receiver) of a cubic cavity has a view factor close to 0.2 (Cengel, 2006). View factors are generally lowered by increasing the effective absorber wall area inside the cavity compared to the frontal aperture. Subsequently, a 'close-to' ideal receiver in terms of low radiation losses depicts a large round enclosure with a miniature inlet aperture. For such a receiver, however, the weight of the receiver tower is increased. It was, therefore, decided to perform a preliminary investigation on the effect of the view factor on the system efficiency. The results are shown in figure 3.5. Efficiency curves were plotted with view factors ranging from 0.2 to 1. The worst system efficiency is experienced at  $F = 1$ . The results also show that the view factor has an increasing significance on the improvement of the system efficiency as the view factor's magnitude gets closer to zero.

After the effect of radiation on the system's efficiency was investigated, the convection term was added to the energy balance equation, as depicted by the last term in equation 3.18

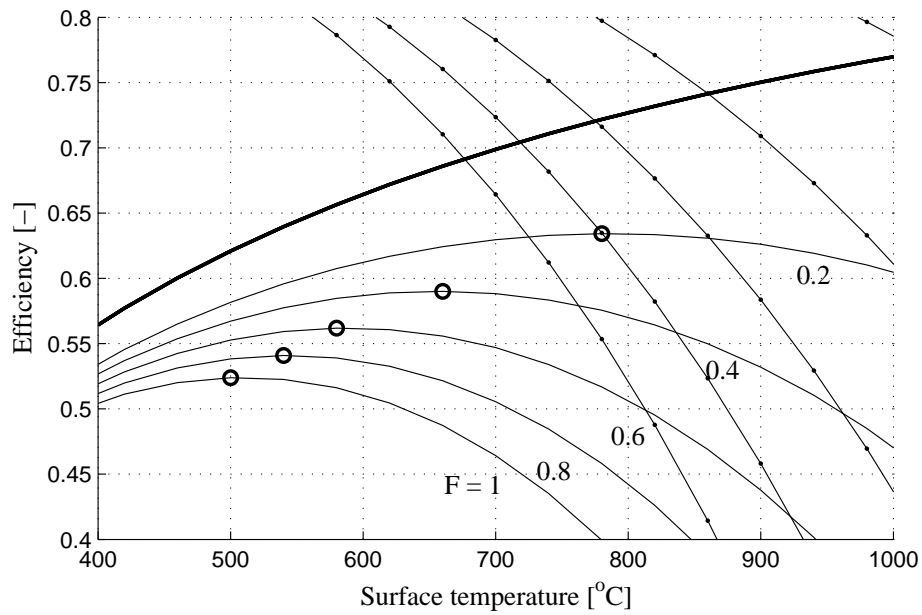


**Figure 3.5:** Sensitivity plot of a simplified receiver model subject to a variation in view factor values

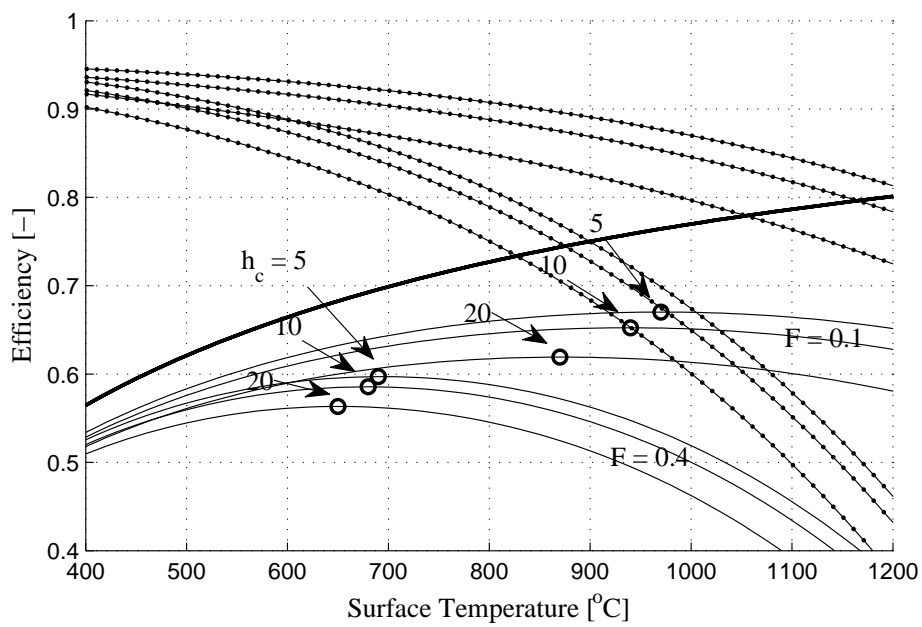


**Figure 3.6:** Sensitivity plot of a simplified receiver model subject to a variation in view factor values and external heat transfer convection coefficient

$$\frac{Q_u}{A} = \alpha C \phi - \sigma \epsilon F (T_s^4 - T_{\text{amb}}^4) - h_c (T_s - T_{\text{amb}}) \quad (3.18)$$

The sensitivity of the convective heat transfer coefficient is illustrated in figure 3.6.

Further sensitivities regarding the variation in view factor and potential improvements with the Hybrid Pressurized Air Receiver (HPAR) concept are presented by Kretzschmar and Gauché (2012).

## 3.6 Parametric Analysis on Internal Pipe Flow

### 3.6.1 Effect of Mass Flow Rate on Fluid Outlet Temperature

Sections 3.5.1 to 3.5.3 have addressed sensitivity analysis in terms of the external surface temperature of the absorber. The surface temperature, however, does not depict what the actual turbine inlet temperature will be. It merely is a close representation. Instead, the actual turbine inlet temperature is given by the fluid temperature at the receiver outlet. The effect and sensitivities accompanied by the heat transfer fluid are incorporated in the following sections. The reason why the sensitivity of the heat transfer fluid is only introduced at this stage is because it is accompanied by multiple varying parameters (e.g., density, viscosity, thermal conductivities, mass flow rate, size of pipe diameters and length etc.). These parameters provide a complex nature to the receiver model. In this section, an internal pipe flow model is presented that was used to investigate the effect of the mass flow rate on the fluid outlet temperature.

Two routines were coded to model the internal pipe flow. The first one was a simple version where the relevant heat transfer equations were developed and iteratively solved by means of calculating the error on the surface temperature variation. The code calculated correct values but showed poor robustness at low mass flow rates through the tubes. This is because the surface temperature is a sensitive parameter, as it affects every equation, and some to the 4th order magnitude. Subsequently, an alternative approach was used in which all resistances were lumped together, and expressions in terms of the collector efficiency factor and heat removal factor were developed. In this approach, the overall heat loss coefficient is iteratively solved until convergence is obtained. Contrary to adapting the surface temperature, a more robust search routine is obtained by adapting the overall heat loss coefficient, especially at low mass flow rates. The derivation of the mathematical equations and method are presented and validated in appendix B.

The effect of the fluid outlet temperature is shown in figure 3.7. For this model the receiver consists of a series of up to 100 tubes in which each tube is exposed to a concentration ratio of 150 suns and a DNI of 1000 W/m<sup>2</sup>. NS-7

properties were used for absorptivity and emissivity values, and no convection losses were imposed. Therefore, regardless of what mass flow rate is chosen, all curves are expected to asymptotically approach 1000 °C if sufficient pipe length is given. This value can also be seen in figure 3.4.

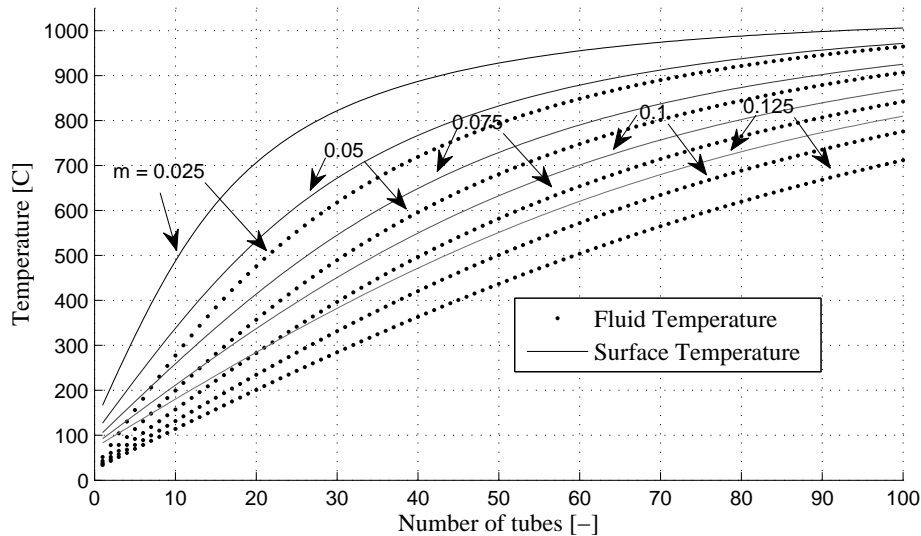


**Figure 3.7:** Sensitivity plot of a simplified receiver model subject to a variation in mass flow rate

Figure 3.7 shows that, compared to higher mass flow rates, when the mass flow rate is lowered, the asymptotic curvature approaches stagnation conditions faster. Additionally, the temperature difference between the fluid and the wall is higher with the low mass flow rates, which reveals the poor thermal properties of air, especially at lower Reynolds numbers. A receiver system should aim to increase the mass flow rate such that the difference between fluid and wall temperature is minimal. Such a design increases the thermal efficiency and, thus, also the absorbed power. For instance, consider the two cases in figure 3.7. In the first case, a fluid outlet temperature of 600 °C is obtained after 28 tube lengths with a mass flow rate of 0.025 kg/s. This corresponds to an absorbed power magnitude of about 29 kW. The second case uses the same number of tubes, but with a mass flow rate of 0.125 kg/s. Here, a fluid outlet temperature of 280 °C is obtained. This corresponds to an absorbed power of 32 kW. The problem, however, is that the temperature drops with an increase in mass flow rate.

### 3.6.2 Effect of Mass Flow Rate on Pressure Drop

In Brayton cycles, the work extracted from the turbine is not only provided by high temperature airflow. It also requires a certain pressure ratio of 5 to

20 in the turbine. The pressure ratio is typically affected by a pressure drop through the receiver, which in turn has a direct impact on the Brayton cycle efficiency.

The effect of the mass flow rate on the pressure drop is shown in figure 3.8. Notice that pressure drop increases exponentially with the mass flow rate and further increases with pipe length. Moreover the pressure drop curve for each mass flow rate flattens out. This is due to the variation in thermal properties as the air stream is heated along the pipe length, as illustrated in figure 3.7.

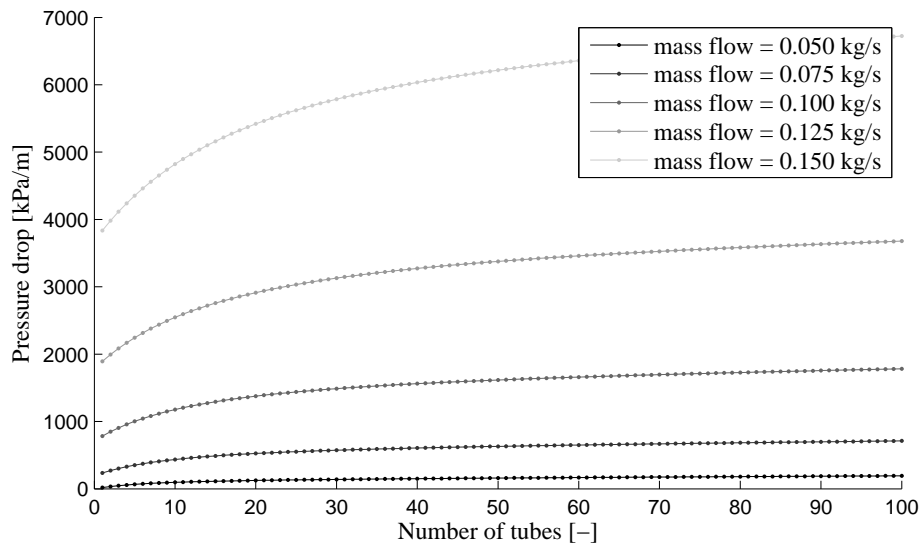


**Figure 3.8:** Sensitivity plot of a simplified receiver model illustrating the effect of the mass flow rate on pressure drop

The trade-off between effective heat transfer, which favours high mass flow rates, and pressure drop, which favours low mass flow rates, gives rise to an optimisation problem in which pipe length, pipe diameter and thermo-fluid properties play an important role. Such an optimisation is typically performed once the system boundary conditions are specified.

### 3.6.3 Effect of Heat Transfer Fluid Properties

The prerequisite for combined cycle power plants is that air is used for high temperature heat transfer fluid as it is directly fed into the gas turbine. It is well known, however, that air is a poor energy extractor. In many practical applications it is in fact used as an insulator. For this reason a sensitivity analysis on air compared to alternative heat transfer fluids was performed.

Figure 3.9 depicts the sensitivity of the fluid outlet temperature and the surface temperature versus the type of heat transfer fluid. Stine and Geyer (2001) states that the weight of a cavity air receiver for a  $380\text{ MW}_t$  tower

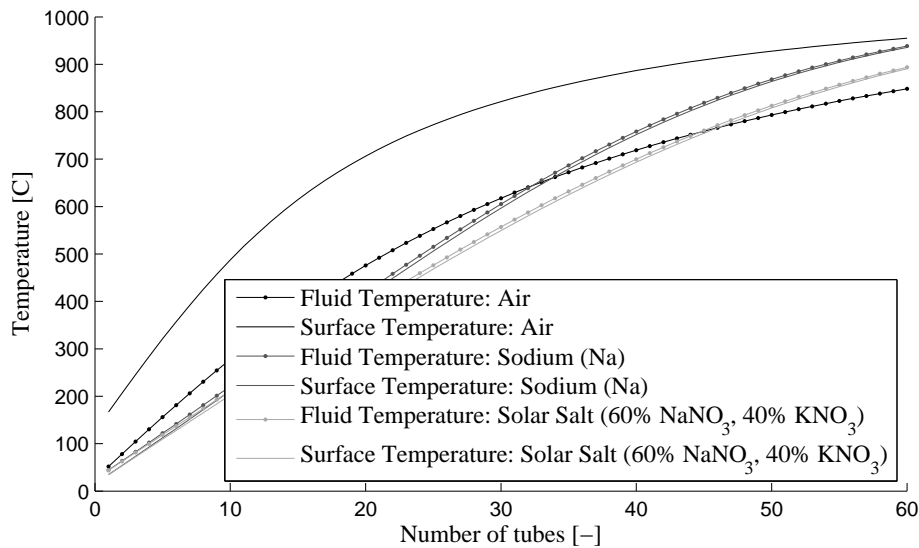


**Figure 3.9:** Illustration of the effect of changing the heat transfer fluid in a simplified receiver model

weighs  $2500 \times 10^3$  kg, compared to a liquid metal receiver at  $250 \times 10^3$  kg. The difference in weight is the result of the better thermal properties of liquid metal. Similar results were obtained in figure 3.9 where the use of solar salt and sodium showed good absorption. Almost no temperature difference between the surface temperature and fluid temperature was obtained. A similar analysis, performed by Boerema *et al.* (2012), shows that the effect of varying the tube thickness is also negligible.

For air, the temperature difference between the surface temperature and the air temperature is significantly higher. Tubular air receivers are, thus, subject to significantly higher thermal losses and low allowable flux densities.

### 3.6.4 Effect of Header System

The effect of using headers instead of tubes in series was investigated by developing models in Flownex where 2 sets of 3 tubes of equal diameter, length and tube thickness (model 1 as depicted in figure 3.10) in parallel were compared to 6 tubes in series with the same geometric specifications (see model 2 as depicted in figure 3.11). The mass flow rate, temperature and pressure at the inlet for both models were set equal. Also, the heat input for both models was set to a constant value of 575 W per tube length.

The analysis revealed that a significant pressure drop was experienced by model 2, namely 14.752 kPa, compared to model 1, where only 1.89 kPa was experienced. This variance resulted from the difference in mass flow rate in the two branches in model 1 compared to model 2. From the sensitivity analysis in section 3.6.2 it was shown that pressure drop is highly sensitive to the mass

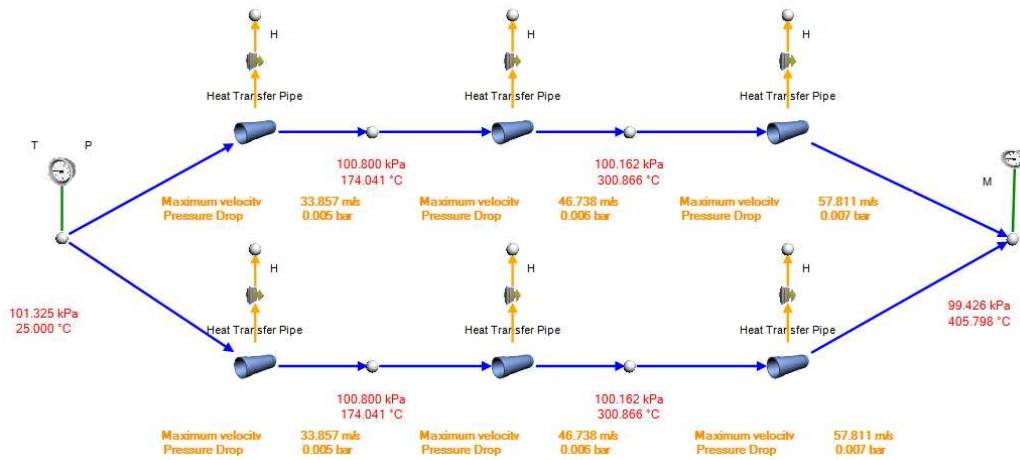


Figure 3.10: Flownex schematic of receiver model where pipes are placed in parallel

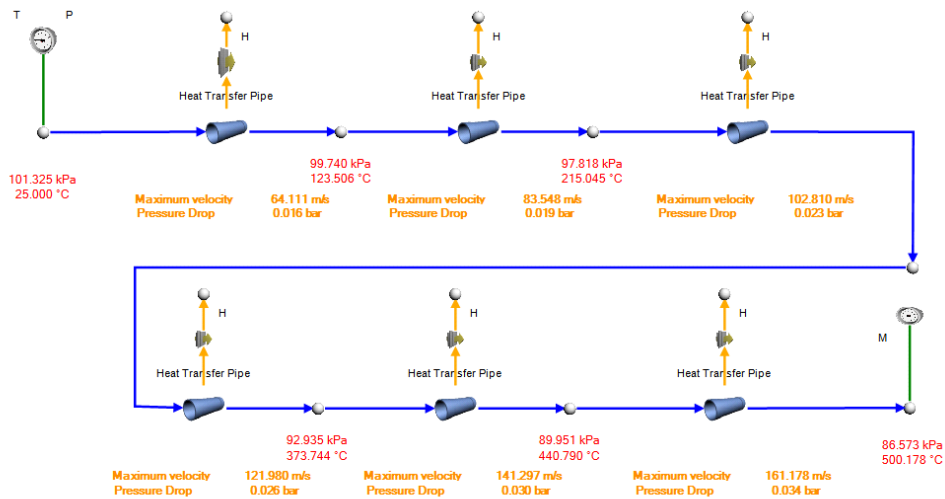


Figure 3.11: Flownex schematic of receiver model where pipes are placed in series



flow rate.

The thermal efficiency of model 2, however, was significantly higher. From the fluid outlet temperature (405.8 °C for model 1 and 500.2 °C for model 2) and equal mass flow rate ( $\dot{m} = 0.005$  kg/s), the absorbed power, and thus efficiency, was calculated. The efficiency of model 1 was 55.5 % while the efficiency of model 2 was calculated as 69.2 %. The higher efficiency was obtained because of the higher convective heat transfer coefficient on the interior of the tube for model 2, which reduces the surface temperature. By comparison, model 1 had significantly higher surface temperatures and thus higher losses.

### 3.7 Conclusion

The parametric analysis showed that there are many challenges involved in finding the optimum solution for a receiver design. Concentration ratio, aspect ratio, heat transfer, mass flow rate and pressure drop are all parameters that positively and negatively affect each other. For the scope of this project, the focus on the energy balance equation was prioritized, but the concept of entropy generation and exergy destruction are equally important. Chapter 4 presents the development of the receiver concept based on the energy balance equation.

## Chapter 4

# Hybrid Pressurized Air Receiver Concept

### 4.1 Introduction

Based on the findings from chapters 2 and 3, this chapter presents the conceptual idea of the HPAR. It further reveals the types of materials suitable for this concept. The expected benefits and drawbacks of the HPAR are also outlined followed by concluding remarks.

### 4.2 Concept Development

Chapter 2 revealed that tubular receivers are favoured over other receiver technologies based on their proven technology, reliability and simple geometry. Tubular receivers, however, lack efficiency and can only accommodate flux densities of around  $200 \text{ kW/m}^2$  (Stine and Geyer, 2001). It was further revealed that volumetric receivers have significantly higher allowable flux densities, but they also experience major limitations. For example, open volumetric receivers have limited applicability to alternative power cycles, and closed volumetric receivers have reliability issues using a pressurized quartz window. It was therefore decided to make use of the tubular technology that does not require the use of a complex pressurized quartz window. Yet, the fact that volumetric receivers can accommodate high flux densities remained attractive.

After several initial design concepts, the hybrid pressurized air receiver (HPAR) concept was derived. The HPAR consists of internally forced flow (typically inside tubes), which is indirectly-irradiated, and externally forced flow, which is directly irradiated. The internally forced flow can be an arbitrary fluid, whereas the externally forced flow is ambient air. In this way, the HPAR can be seen as a volumetric tube receiver, as shown in figure 4.1.

The concept was further developed by incorporating transparent glazing through which the forced airflow could pass and, thus, prevent the glazing

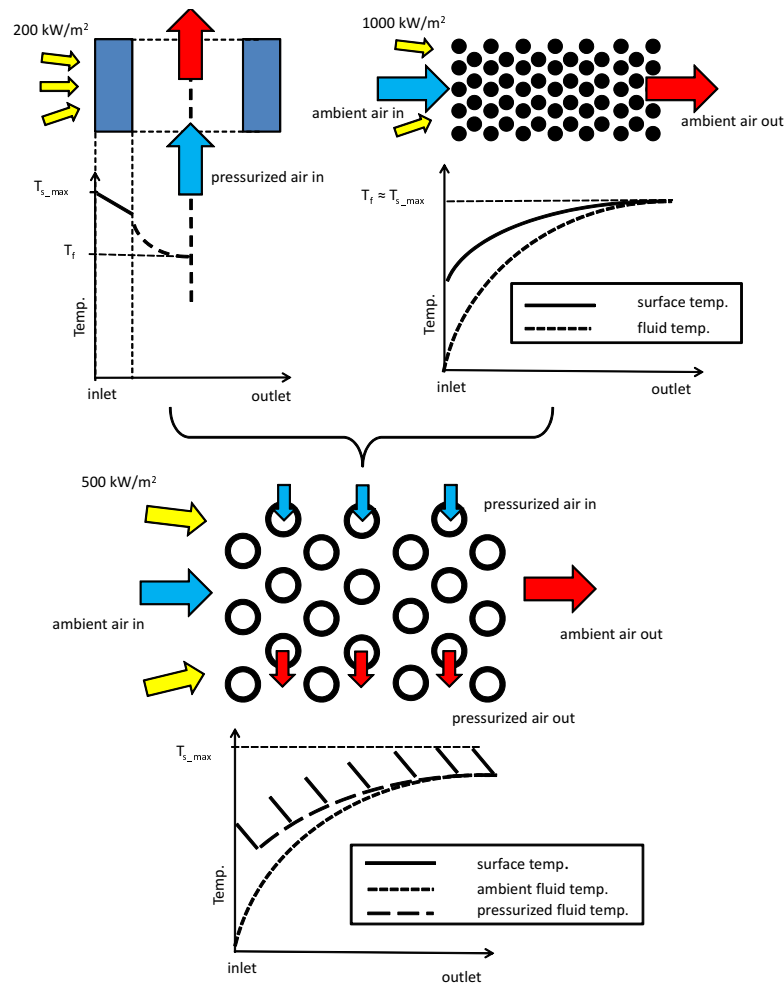


**Figure 4.1:** Illustrating of the development of the HPAR concept based on tubular and volumetric receiver technologies (adapted from Hoffschmidt *et al.* (2003))

from overheating. Based on the 'greenhouse effect', the purpose of the glazing is to minimize reradiation losses from the absorber tubes (Duffie and Beckman, 2006).

Because airflow was allowed through the glazing, the concept was further developed where the glazing actively takes part in the absorption process. This was done by adding multiple rows of transparent glass elements. For example, in figure 4.1 the front two or three rows of tubes were replaced by solid glass structures to emulate this effect. The idea is that the transmissivity of the absorber medium gradually varies from fully transparent at the front of the receiver to fully opaque at the back of the receiver.

The light transmission through the receiver follows the principle of Beers law where a parameter, called the extinction coefficient, controls the amount of light passing through a medium. The extinction coefficient is given by the following equation (Howell *et al.*, 2011),

$$\beta_\lambda = \kappa_\lambda + \sigma_\lambda \quad (4.1)$$

which is a combination of the spectral absorptivity coefficient ( $\kappa_\lambda$ ) and the spectral scattering coefficient ( $\sigma_\lambda$ ). The flux intensity is affected by the extinction coefficient as given in the integral,

$$\int_{I_\lambda=I_\lambda(0)}^{I_\lambda(S)} \frac{dI_\lambda}{I_\lambda} = - \int_{S^*=0}^S \beta_\lambda(S^*) dS^* \quad (4.2)$$

After integrating, the following expression is obtained,

$$I_\lambda(S) = I_\lambda(0) \exp(-\beta_\lambda S) \quad (4.3)$$

which shows that the extinction coefficient exponentially affects the flux intensity over depth ( $S$ ). When considering the depth of the receiver as the depth of the medium, the flux intensity follows a similar curve as expected for the volumetric effect, shown in figure 4.1. Figure 4.2 illustrates the concept of light extinction through the receiver by having a transmitting zone followed by an absorbing zone. Accordingly, it is expected that the high incident flux will be gradually converted to thermal energy and hot spots are less likely to occur. Also, the highest surface temperatures are expected deeper into the receiver, where the aggregated view factor is lower.

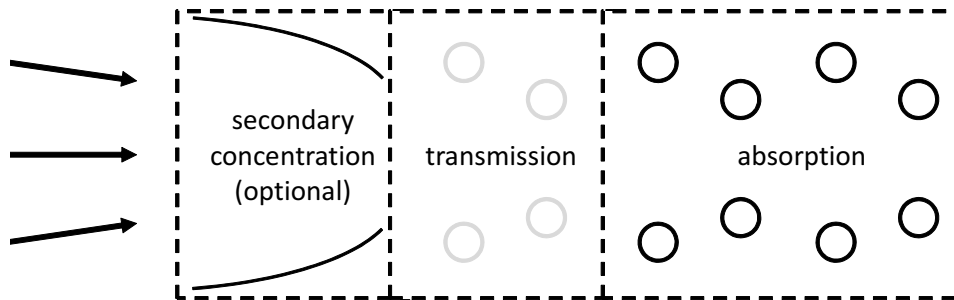


**Figure 4.2:** Illustration of HPAR concept in terms of the transmission zones

Figure 4.2 also depicts a secondary concentrating zone, which is an optional design feature of the HPAR. Secondary concentration is typically performed by means of a compound parabolic concentrator (CPC), which has been presented in numerous publications (Baranov, 1966; Winston, 1974; Winston and Hinterberger, 1975; Winston *et al.*, 2004; Heller *et al.*, 2006). The CPC is typically used to increase the flux density on the receiver.

Another design aspect added to the initial HPAR concept was to make use of an air return loop, as depicted in figure 4.3. Excess air from the heat recovery system (in this case a rock bed thermal energy storage system (TESS) which feeds a heat recovery steam generator (HRSG)) is fed back into the receiver at the front of the receiver aperture. Figure 4.3 is a schematic diagram of a potential application of the HPAR in a combined cycle as proposed by Heller and Gauché (2013).

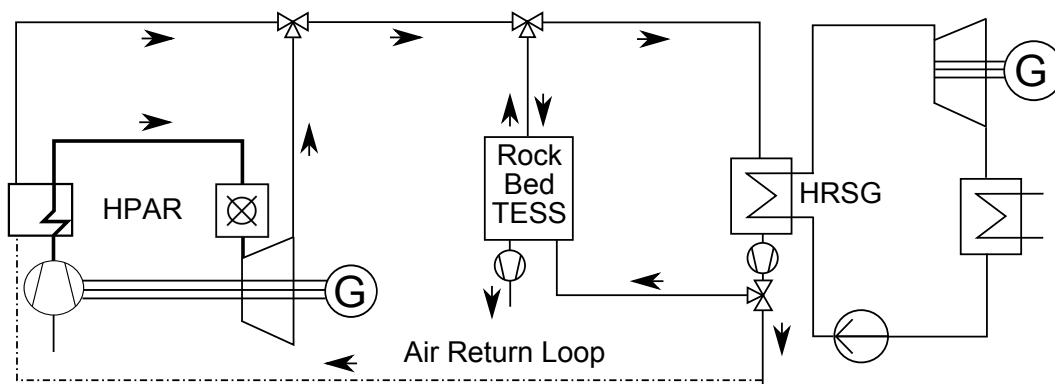


**Figure 4.3:** Schematic diagram of a combined cycle utilizing the HPAR (courtesy of L. Heller)

### 4.3 Material Considerations

Fused silica quartz is a state-of-the-art material suitable for the transmitting zone, which forms the low temperature region of the receiver. Based on the assumption that the surface temperature of the material in the transmitting zone is expected to be  $1/3$  of the highest temperature, fused silica quartz would still be adequate for a receiver reaching  $3000\text{ }^{\circ}\text{C}$  maximum temperature, as it can operate up to  $1050\text{ }^{\circ}\text{C}$ .

The fully opaque region with current state-of-the-art materials is comprised of either Silicon Carbide (SiC) ceramic panels or Inconel tubes. SiC absorber panels have been applied to solar applications in most recent publications. This ceramic material has a high strength, good thermal conductivity, very low thermal expansion coefficient, it is gas-tight and the design and construction of inner channels can be done easily. Problems involved with ceramic panels stem from the fact that, at the moment, the construction of these panels is limited to size ( $500\text{ mm}$ ). Additionally, the coupling between the ceramic and steel pipe at the turbine inlet is problematic due to thermal stresses.

Inconel tubes have been chosen for several solar projects over the last few years (Heller, 2011). Inconel is a super-alloy which can sustain temperatures up to  $950\text{ }^{\circ}\text{C}$ .

## 4.4 Expected Benefits of the HPAR Concept

In theory, the HPAR concept should provide several benefits, including better heat transfer to the working fluid, more controllability and higher efficiency.

Better heat transfer to the working fluid is expected because of the introduction of the externally forced airflow. Energy absorption is distributed over the volumetrically configured absorber tubes and, thus, allows the internal forced flow to gain energy over a longer path.

It is also expected that the external forced flow provides more controllability by means of regulating the allowable flux incident on the receiver aperture. That is, the ambient air flow can be increased if the hot irradiated tubes reach the maximum allowable surface temperature. As a result, more energy is transferred to the ambient air stream rather than further heating up the tubes. The hot air stream can then be used in a heat recovery system, either for recuperation purposes or thermal storage.

Because the externally forced flow is expected to increase the allowable flux density, the size of the receiver can be reduced, which reduces costs.

A further benefit includes the fact that the externally forced airflow aids in a more equalized temperature distribution around the periphery of the tubes. Hot air on the irradiated side of the tubes is dragged around the tubes to the shadowed side, thus heating up that side, while the irradiation side is cooled. In this way, thermal stresses on the tube material are reduced and buckling of tubes is minimized. These aspects aid in minimizing the generation of local hotspots.

The HPAR is expected to have higher efficiencies, compared to other tubular air receivers, because of reduced radiation losses, convection losses and reflection losses.

Radiation losses are expected to be lower due to the volumetric effect and the use of glazing. Light is allowed to penetrate deeper into the material, and the glazing is expected to provide a radiation shield such that reradiation is less likely to escape. For higher flux densities, the receiver size can be smaller, thereby reducing the surface area from which reradiation is emitted.

Convection losses are expected to be low as the externally forced airflow is designed to prevent buoyant plumes from escaping out of the receiver.

Although the HPAR manifestation in this project makes use of cylindrical quartz wafers and tubes, reflection losses can be minimized by instead using triangular prismatic shapes. If the sharp edges of the prisms are pointed towards the incident flux, most of the reflected rays are directed into the receiver. In contrast, cylindrical tubes are expected to experience higher reflection losses as the reflected rays at the frontal side of the tube are directed towards the surroundings.

## 4.5 Potential Drawbacks of the HPAR Concept

Since the HPAR is based on the volumetric and tubular receiver technologies, it inherits some of their drawbacks. Problems regarding tubular receivers include the poor heat transfer from the tube to the working fluid, especially when air is used, and this remains a challenge for the HPAR as well. Additionally, major temperature gradients are expected not only around the periphery of the tubes but also longitudinally. Pressurized tube receivers generally experience problematically high pressure drops, and the HPAR also faces this challenge. Volumetric receivers have less constrained fluid flow, which gives rise to flow instabilities that in turn tend to generate hotspots. The externally forced airflow might cause similar problems where certain parts of the tubes or quartz wafers are cooled more than others, and local overheating might occur.

Because the HPAR aims to provide more heat transfer of the tubes externally as well as internally, more friction and irreversibilities are generated. As a result, more exergy is destroyed, reducing the quality of energy.

## 4.6 Experimental Manifestation of the HPAR

An experimental manifestation of the HPAR is shown in figure 4.4, consisting of tube bundles volumetrically placed in a tapered cavity.

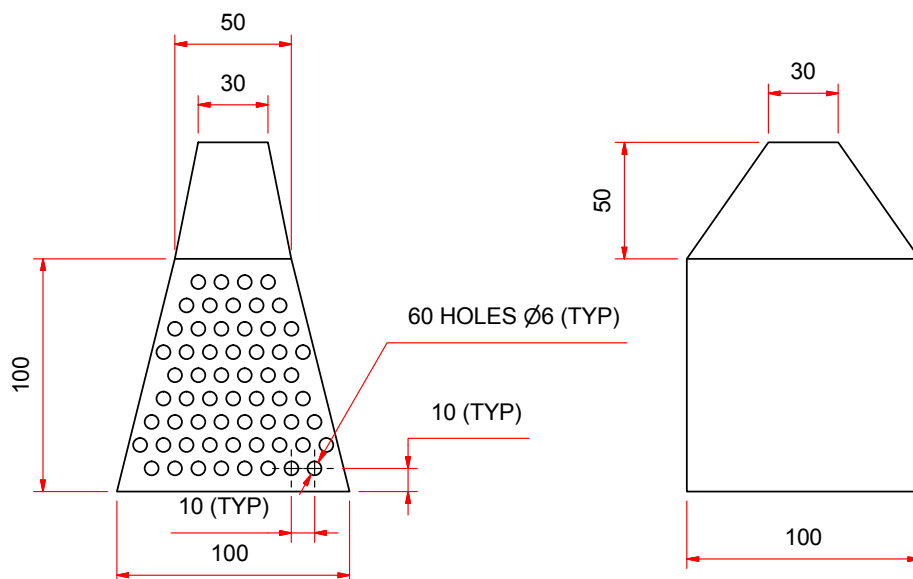


**Figure 4.4:** Sketch of the experimental manifestation of the HPAR.

Intuitively, a tapered cavity was chosen with the objective of suppressing an excessive development of the boundary layer. For a large boundary layer

thickness, the convective heat transfer coefficient in the near wall region is low. Tubes located in this region would face local overheating. The design of an optimal cavity shape and distribution of the tube bundles is beyond the scope of this project.

The tube configuration shown in figure 4.4 also allows for the use of headers. As pointed out in chapter 3, headers can be used as a means to reduce pressure drop, at the expense of heat transfer and high tube temperatures. Because forced air flow is applied on the tube exterior, the increase in tube temperatures is expected to be controllable and therefore material failure is less likely to occur.

## 4.7 Numerical Analysis and Validation Method

The following chapters will investigate whether the HPAR concept can effectively eliminate convective plumes escaping from the aperture by means of the externally forced air flow. Also, more insight on the impact of the externally forced flow on the fluid and wall temperatures is revealed.

From chapter 3 it is known that air is a poor energy extractor. If the wall temperatures are less likely to be affected by the forced airflow, ongoing research will have to investigate means to provide more controllability on the wall temperatures. These findings are, thus, crucial to the HPAR concept.

In section 4.3, quartz glass was proposed as a semi-transparent medium to perform the gradual extinction of light through the receiver. It is aimed to model and test this idea. The research should also investigate whether quartz glass acts as a thermal radiation shield or not. Additionally, the impact of quartz glass on reflection losses will be explored. The following chapters therefore aim to investigate the functionality of the HPAR concept.

A combination of ray-tracing, coupled natural convection and radiation heat transfer simulation tools were used to investigate the objectives. The ray-tracing was used to determine the amount of reflection losses experienced from the receiver and to quantify the solar flux incident on the wall surfaces of the receiver. These flux profiles were then mapped into a CFD software package where the effect of buoyancy-driven flow and radiation heat transfer was investigated.

The numerical results were compared against experiments to ensure validity. This was done by characterising a small-scale medium flux concentrator and using the solar concentrator to perform a parametric test on the receiver model. The characterisation of the flux concentrator is presented in appendix D where the solar concentrator was modelled in SolTrace with the receiver being a flat target. The flux and power magnitude on the flat target was quantified and compared against measured experiments. This method not only characterises the solar concentrator to determine how much power can be expected, but validates the use of SolTrace as a stand-alone numerical model.



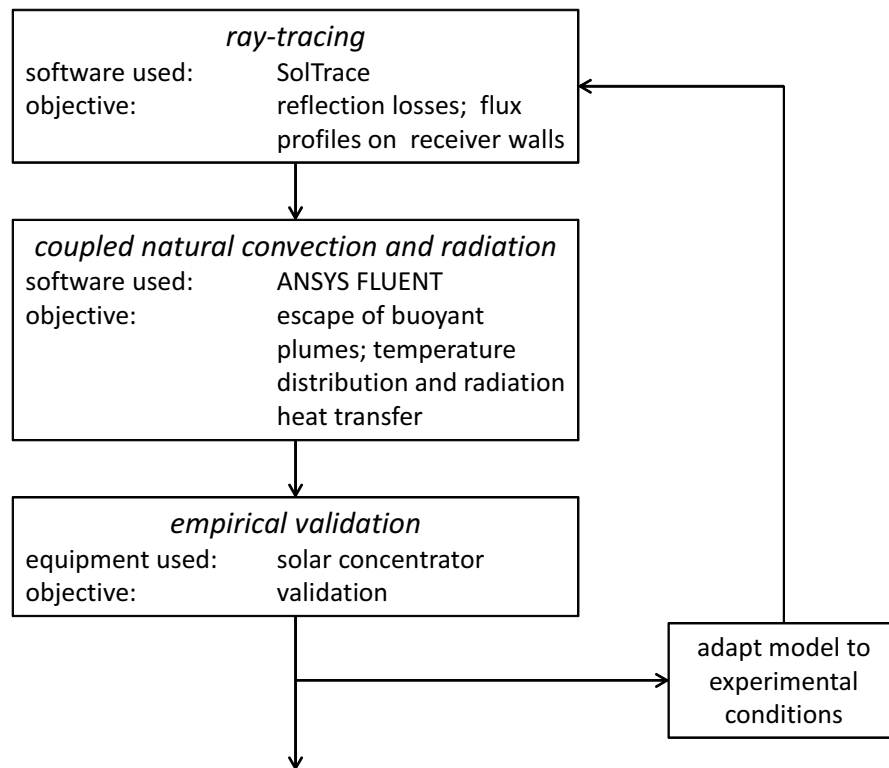


**Figure 4.5:** Outline of numerical simulation and validation method

The power on the concentrator was measured by constructing a cold-water flat plate calorimeter, as discussed in appendix C. The calorimeter was calibrated using a flat resistance heating element in which a quantified electrical power input was applied to the calorimeter and the thermal response was measured. This work was published by Kretzschmar *et al.* (2012).

Four cases were set up for investigation. These cases were conducted on a receiver model, as shown in figure 4.4. The receiver consists of 60 tubes arranged in nine rows, of which row 1 starts at the front of the receiver and row 9 on the rear tapered side of the receiver. Isometric views of the receiver model are shown in figures 5.1 and 6.2. The parametric test on the effect of eliminating the escape of buoyant plumes was investigated by applying an externally forced flow of 2.3 m/s to the receiver and comparing the results with a case where no forced airflow was applied. It was also expected to gain more insight on how efficient the forced airflow can cool down the tubes. In table 4.1, cases I and III depict the forced air flow condition and cases II and IV depict the stagnation condition.

Moreover, the impact of quartz glass was investigated by replacing the first three rows of the receiver module with infra-red graded fused silica quartz glass. Numerical modelling and empirical temperature measurements are expected to show whether a quartz receiver should gain preference over a fully packed

**Table 4.1:** Parametric case description to investigate the HPAR concept

Case Number	Flow Conditions	Tube Configuration
I	forced air flow (2.3 m/s)	row 1-9: stainless steel tubes
II	no flow	row 1-9: stainless steel tubes
III	forced air flow (2.3 m/s)	row 1-3: quartz wafers; row 4-9: stainless steel tubes
IV	no flow	row 1-3: quartz wafers; row 4-9: stainless steel tubes

tube receiver. Cases I and II depict the fully packed tube receiver and cases III and IV depict the quartz receiver.

## 4.8 Conclusion

Following the initial analysis, a review of the different types of receivers and an extensive concept development phase, the hybrid pressurized air receiver concept emerged. The combination of the respective features appears to give the concept merit, which, based on the analysis and validation method, is investigated in the following chapters.

# Chapter 5

## Ray-Tracing Analysis

### 5.1 Introduction

A ray-tracing analysis is often found in solar modelling applications where it is desired to model the resultant solar flux on a component or assembly of components, especially when concentrating mechanisms are involved. In this project, the ray-tracing analysis is used to predict the flux on receiver tubes generated by a medium flux concentrator. A brief description of the model is given, followed by a description of the modelling setup, ray-tracing results and the conclusions.

### 5.2 Description of Model

Figure 5.1 shows an illustration of the concentrator as modelled in SolTrace consisting of two stages, the heliostat field and the receiver. The heliostat field consists of 150 mirrors equally spaced on linear rails. The size of the heliostat field is 2 m by 2.5 m. The first 5 rows are spaced 200 mm apart, and the last 4 rows are spaced 250 mm apart.

The receiver stage consists of 60 tubes equally spaced in a staggered configuration inside a tapered cavity. The aperture size is 0.1 m by 0.1 m, the depth of the cavity is 0.1 m, and the rear width of the tapered cavity is 0.05 m. The tilt angle of the receiver was set to  $39^\circ$  from the global horizontal plane. The tilt angle was found by optimising it for maximum flux into the receiver. A spillage wall was defined in-line with the aperture to intercept all the off-target rays.

The central rear heliostat was omitted from the ray-tracing simulation because in practice it was used as the beam calibration heliostat. The beam calibration heliostat was used to perform the dual-axis tracking by moving the rig such that the heliostat pointed at the beam calibration target, while all other heliostats pointed at the receiver aperture. The beam calibration target was positioned 0.1 m below the aperture.

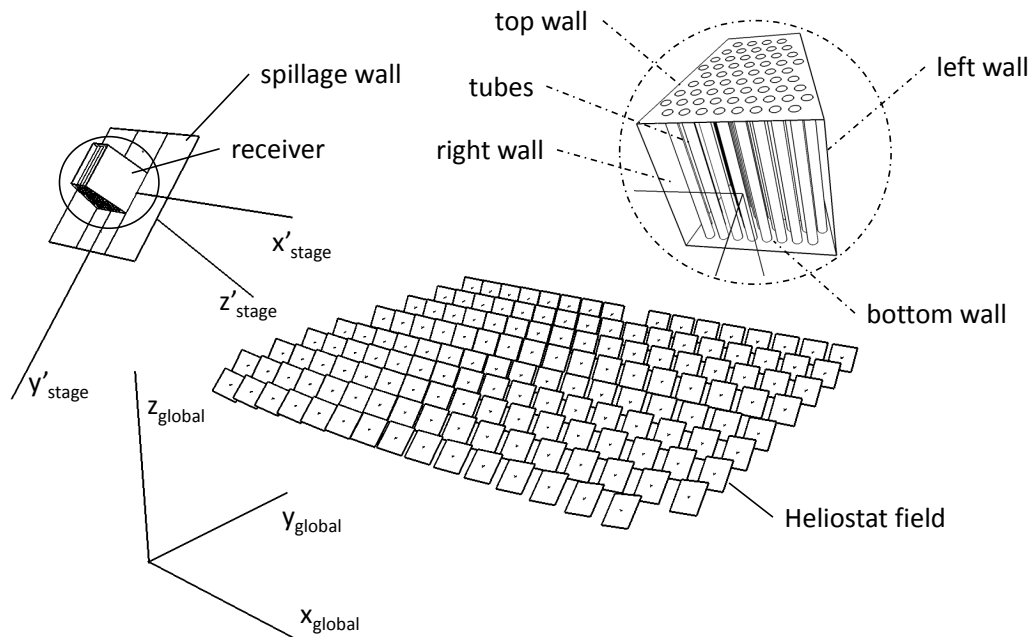


**Figure 5.1:** Illustration of a dual-axis tracking solar concentrator that simulates the performance of a heliostat field for a specific time of day and season

## 5.3 Modelling Setup

### 5.3.1 Matlab-SolTrace Coupling

SolTrace is a ray-tracer developed by the National Renewable Energy Laboratory (NREL, 2013). It was used in this study because of its rapid processing time, and because it is considered a benchmark ray-tracing tool for alternative software releases. SolTrace has a simple graphical user interface and good scripting capabilities. However, because the software does not provide automatic tracking a script had to be developed to, among other functions, calculate the aimpoints. It was decided to do the tracking calculations of the heliostats in Matlab and perform the data exchange between the Matlab code and the SolTrace script via \*.csv files, as shown in figure 5.2.

The main platform was coded in Matlab. SolTrace is considered as a 'black box' that is used to execute the ray-tracing and return the results. Figure 5.2 illustrates the data exchange between the two platforms. The sun's zenith angle was specified from which the sun's position in y- and z-coordinates are calculated and stored in the sundef.csv file (section 5.3.2). The data within this file is accessible to the SolTrace script once launched. The optical properties are defined in the SolTrace script, as they are treated as non-varying parameters. If a sensitivity analysis on the optical properties was performed, a new \*.csv

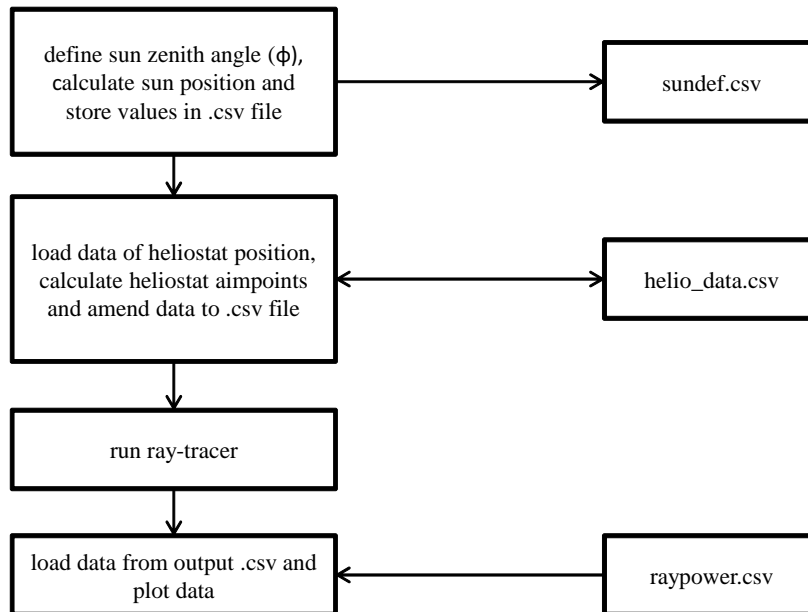


**Figure 5.2:** Illustration of the \*.csv file data exchange between the Matlab and SolTrace platforms

file would have to be set up for these parameters to be accessed. Section 5.3.3 presents the various optical parameters and values. The heliostat positions are read from the `helio_data.csv` file and stored into Matlab variables. A for-loop runs through each heliostat position and calculates the corresponding aimpoint, as discussed in section 5.3.4. The calculated aimpoints are stored back into the `helio_data.csv` file. Subsequently, the ray-tracer is launched from the Matlab code using a disc operating system (DOS) command prompt.

Within the SolTrace script the z-rotation angles, described in section 5.3.5, are calculated. Finally, after the trace has been executed, with a certain number of rays (see section 5.3.6), an output \*.csv file is updated with the trace results.

### 5.3.2 Sun Position and Shape

The sun position can be defined by using the global coordinate or by latitude, day and hour. When using the latitude, day and hour option, SolTrace defines the global x-, y- and z-axis such that the z-axis points due north, y-axis points to zenith and x-axis points west. In contrast, when using the global coordinates, the direction of the x-, y- and z-axis can be manually specified. For all simulations performed in this project, the latter option was chosen. The sun's position was calculated such that the global z-axis points to zenith, the global y-axis points south and the global x-axis points west.

SolTrace further allows defining the sun shape as a Gaussian distribution, a

pillbox shape or an arbitrary user-defined function. The solver then generates a sun shape profile accordingly. The pillbox shape is a rather simplistic approximation but adequate for systems where the distance between the target and the reflector is small. Therefore, the pillbox shape was used with a default sunshape parameter value of 4.65.

The sun's position for this model was set to the position when the actual rig was calibrated to empirically validate the numerical results, presented in section D.4. The rig was calibrated on 28 June 2013 such that the tilt angle of the rig was  $6^\circ$  at solar noon (12:48:00 PM). From the NREL's solar position algorithm (SPA) database developed by Reda and Andreas (2003), the zenith angle of the sun at solar noon was recorded as  $63^\circ$  (NREL, 2013), and the sun's elevation angle was calculated as  $21^\circ$  given by the formula

$$\theta_{\text{elv}} = 90 - \theta_Z - \theta_{\text{tilt}} \quad (5.1)$$

### 5.3.3 Optical Properties

Optical properties for mirror glass and carbon black coating are summarized in table 5.1.  $\rho$  and  $\tau$  depict the reflectivity and transmissivity values of the mirror and absorber paint, respectively.

**Table 5.1:** Optical properties of mirror glass and carbon black coated absorber materials (Tahboub *et al.*, 2012; Pompea and Breault, 1995)

Material	Parameter	Value	Unit
Mirror glass (front)	$\rho$	0.95	[-]
	$\tau$	0	[-]
	Slope error	0.9	mrad
	Specularity error	8.5	mrad
Mirror glass (back)	$\rho$	0	[-]
	$\tau$	0	[-]
	Slope error	0.9	mrad
	Specularity error	0.2	mrad
Absorber (front)	$\rho$	0.04	[-]
	$\tau$	0	[-]
	Slope error	0.9	mrad
	Specularity error	0.2	mrad
Absorber (back)	$\rho$	0.04	[-]
	$\tau$	0	[-]
	Slope error	0.9	mrad
	Specularity error	0.2	mrad

### 5.3.4 Aimpoint Calculation

The aimpoints for the heliostat positions were calculated based on the parallelogram rule in vector algebra, given the sun position, heliostat position and target position. Equations 5.2 to 5.7 are used to perform the algebra,

$$\hat{\mathbf{S}} = \frac{\mathbf{S}}{\|\mathbf{S}\|} = \frac{\mathbf{S}}{\sqrt{S_x^2 + S_y^2 + S_z^2}} \quad (5.2)$$

$$\mathbf{R} = \mathbf{T}_p - \mathbf{H}_p \quad (5.3)$$

$$\hat{\mathbf{R}} = \frac{\mathbf{R}}{\|\mathbf{R}\|} = \frac{\mathbf{R}}{\sqrt{R_x^2 + R_y^2 + R_z^2}} \quad (5.4)$$

$$\mathbf{N} = \hat{\mathbf{S}} + \hat{\mathbf{R}} \quad (5.5)$$

$$\hat{\mathbf{N}} = \frac{\mathbf{N}}{\|\mathbf{N}\|} = \frac{\mathbf{N}}{\sqrt{N_x^2 + N_y^2 + N_z^2}} \quad (5.6)$$

$$\mathbf{N}_{l \rightarrow r} = \mathbf{H}_p + \hat{\mathbf{N}} \quad (5.7)$$

where  $\mathbf{S}$  denotes the vector from the origin to the sun's position,  $\mathbf{H}_p$  the vector from the origin to the heliostat position and  $\mathbf{T}_p$  the vector from the origin to the target position.  $\hat{\mathbf{N}}$  is the calculated normal unit vector of the heliostat and  $\mathbf{N}_{l \rightarrow r}$  depicts the aimpoint vector stored back into the \*.csv file. The subscript  $l \rightarrow r$  denotes the transformation from the local reference frame of the heliostat to the global reference frame of the system, which is essential for the correct usage of the global, stage and element coordinate definition in SolTrace.

### 5.3.5 Z-Rotation Angles Calculation

The aimpoint vector is also accompanied by a certain angle of rotation around its axis. In SolTrace, this angle is termed the z-rotation angle. This is because SolTrace, by default, defines the local element coordinate system such that the z-axis points to the aimpoint. The z-rotation angle becomes significant when different tracking strategies are modelled, such as horizontal-azimuth tracking or spinning-elevation tracking (Chen and Buck, 2004). For the studies performed during this project the horizontal-azimuth tracking was relevant due to the physical constraints of the solar concentrating mirrors. The z-rotation angle is calculated such that the bottom mirror surface of each facet is flush with the global horizontal plane.

The rotation of a heliostat can have multiple solutions, and the choice of the order of the rotating angle has a major impact on the solution. For instance, if a heliostat is transformed from the initial position to the final

position, by first transforming the zenith angle, then the azimuth angle and finally the z-rotation angle, different results would be obtained when choosing an alternative order.

The Rodriguez formula and the Euler angle transformation strategies were considered. However, preference was given to the Euler angles strategy since SolTrace has a standard Euler function embedded in its library, where the choice of the order of the rotating angles is automatically performed. The Euler function simply outputs the Euler vectors; one being the x-axis unit vector and the other the y-axis unit vector.

The calculation is performed by assuming an initial z-rotation angle of zero. The result is then used to calculate the required z-rotation angle such that the x-axis unit vector is parallel to the x-y plane. To accomplish this, a new vector is defined pointing from the local heliostat position vertically upwards, i.e.,  $V = [001]$ . Then, the cross product between the local aimpoint vector and the vertical vector is obtained, which provides the desired x-axis unit vector. In other words, the original x-axis unit vector with zero z-rotation is rotated with a certain angle such that it is equal to the desired x-axis unit vector ( $\mathbf{U}_2$ ). The respective angle ( $\zeta$ ) is obtained taking the dot product between the two x-axis unit vectors and solving for the angle  $\zeta$ . The equations used are given below

$$\mathbf{N}_{r \rightarrow 1} = \hat{\mathbf{N}} - \mathbf{H}_p \quad (5.8)$$

$$\mathbf{U}_2 = \mathbf{V} \times \mathbf{N}_{r \rightarrow 1} \quad (5.9)$$

$$\zeta = \arccos \left( \frac{\mathbf{U}_2 \cdot \mathbf{U}_1}{\|\mathbf{U}_2\| \|\mathbf{U}_1\|} \right) \quad (5.10)$$

### 5.3.6 Trace Options

All final simulations were run at 2 million ray intersections and a maximum number of 20 million generated rays. Eight central processing units (CPU) were utilized with an automatically selecting seed value of -1. Optical errors were included for the simulations.

## 5.4 Numerical Results

Two cases were investigated in the ray-tracing simulation. The first case consisted of the receiver fully packed with absorber tubes, as tested on 30 July 2013. On 30 July an averaged DNI value of  $940 \text{ W/m}^2$  was recorded during the time of testing. Figure 5.3 illustrates the ray-paths and the ray intersections at the heliostat field and the receiver for the fully packed receiver case.



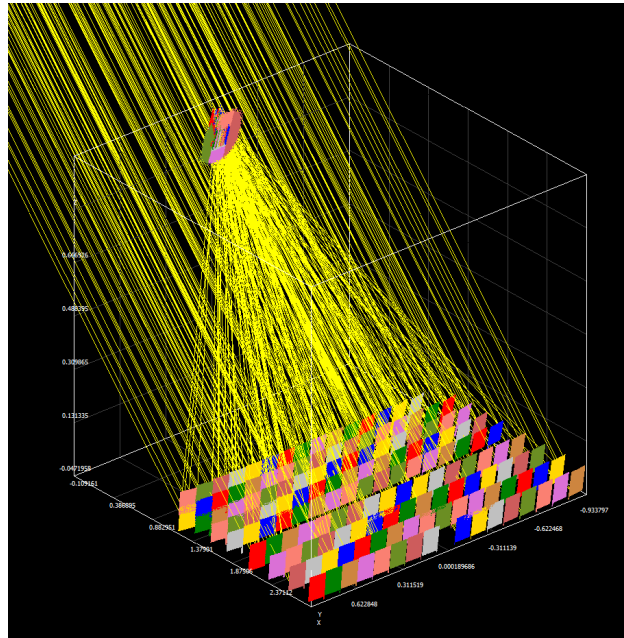


**Figure 5.3:** Illustration of the ray hitpoints and the ray paths for the dual-axis tracking solar concentrator, as modelled in SolTrace

The second case investigated the receiver where the first three rows of tubes were replaced by quartz wafers. Quartz was defined as a new optical property with a transmissivity of 0.9, reflectivity of 0.07 and refractive index of 1.45 (Tydex, 2013). Based on the transmission curve shown in figure 6.3, a constant transmissivity of 0.9 was used throughout the visible light spectrum. This receiver model was tested on 1 August 2013 where an averaged DNI value of  $830 \text{ W/m}^2$  was recorded. This DNI value was used for the second case.

Figures 5.4 and 5.5 illustrate the ray hitpoints for the fully packed tube receiver and the quartz receiver respectively.

One can clearly see that the quartz rows allow light to penetrate deeper into the receiver. Also the peak flux on the tubes differed significantly. For an incident peak flux of  $97\,000 \text{ W/m}^2$ , the highest flux in the fully packed tube receiver was experienced in the front row and amounted to  $89\,000 \text{ W/m}^2$ . The highest flux in the quartz receiver was obtained at the 4th row with  $38\,000 \text{ W/m}^2$ , followed by the left and right side walls with  $35\,100 \text{ W/m}^2$  and  $36\,000 \text{ W/m}^2$ , respectively. The fourth row in the quartz receiver is the first opaque tube row. The results therefore show that the use of quartz glass effectively reduces the flux densities on the receiver surfaces by gradually performing the extinction of light. Tables 6.2 and 6.3 summarize the wall fluxes obtained from SolTrace.

The amount of reflection losses for both cases was also investigated. This was done by adding a third virtual stage to the model, which is used to count the number of hitpoints exiting the receiver aperture. It was found that 1.4%

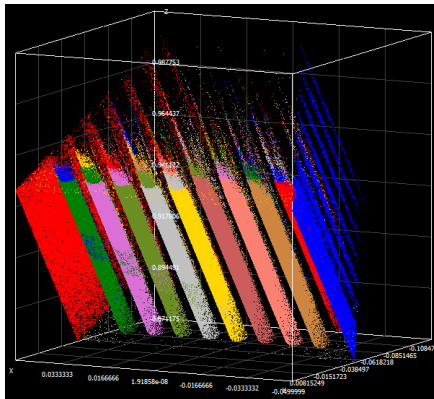


**Figure 5.4:** Ray hitpoints of fully-packed tube receiver

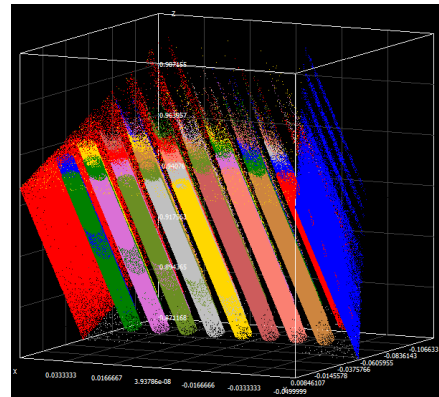


**Figure 5.5:** Ray hitpoints of receiver including quartz wafers

of reflection losses were experienced by the fully packed tube receiver, and 7.8 % were obtained for the quartz receiver. As mentioned in chapter 4, reflection losses can further be reduced by using triangular prismatic elements, where reflected rays are directed to the inside of the receiver. The investigation of the effect of triangular wafers, however, was considered beyond the scope of this project.

## 5.5 Conclusion

The ray-tracing simulation showed that the use of quartz glass allows rays to penetrate deeper into the receiver, compared to a fully packed tube receiver. Also, flux densities on the receiver surfaces are lowered and, thus, less likely to cause material failure. The quartz receiver, however, experiences more reflection losses. The ray-tracing results are further used in chapter 6 to investigate the coupled natural convection and radiation heat transfer.

## Chapter 6

# Coupled Natural Convection and Radiation Heat Transfer Simulation

### 6.1 Introduction

Very few studies have considered coupling the natural convection and radiation heat transfer (Kumar and Eswaran, 2010). This is due to radiation propagating at much faster speeds than convective fluxes. Because of the large separation of velocity scales, the radiation solver adjusts itself much quicker than the flow solver. Also, the radiation solution does not directly depend on the fluid velocity, so there is no specific need to use the coupling approach. The radiation solver, however, requires the spatial distribution of temperatures and species concentration, which at high temperature variations, forms a strong indirect coupling between the flow and radiation solver (Versteeg and Malalasekera, 2007).

Kumar and Eswaran (2010) and Moufekkik *et al.* (2013) briefly outline previous projects involved in coupled natural convection and radiation heat transfer simulation of generalized partially enclosed cavity shapes, such as square cavities and a few others. Nouanegue *et al.* (2008) lists more than 20 references found in literature that involve natural convection in partially enclosed cavities, imperial investigations, and some that have also considered conjugate heat transfer simulations.

To date no studies have investigated the effect of externally forced flow through a tapered cavity filled with volumetric tubes. This geometry definition is uniquely derived to meet the physical requirements of the HPAR concept. Additionally, limited publications exist that consider the coupling of a ray-trace utility to CFD (Uhlig, 2009; Garbrecht *et al.*, 2012).

The following sections highlight the fundamental background of natural convection and radiation heat transfer simulation in CFD, followed by a dis-

cussion of the most relevant modelling tools and assumptions, and finally a brief summary of the modelling results are shown.

## 6.2 Buoyancy-Driven Flow

### 6.2.1 Theory Background

Buoyancy-driven flow occurs as a result of density variation within a flow domain caused by temperature variation, which in turn changes when a heat input is applied to the domain. A flow motion is thus induced as gravity forces act on the density variation. Buoyancy-driven flows typically occur in natural convection problems and can be categorized by the Archimedes number (AR), which provides a ratio between buoyancy forces and inertial forces and, thus, momentum forces (Li, 2007). The Archimedes number is obtained by equation 6.3, which is dependent on the Grashoff number and the Reynolds number (Li, 2007). The numbers are given by the following equations,

$$\text{Gr} = \frac{g\beta\Delta TL^3}{\nu^2} \quad (6.1)$$

$$\text{Re} = \frac{VL}{\nu} \quad (6.2)$$

$$\text{Ar} = \frac{\text{Gr}}{\text{Re}^2} = \frac{g\beta\Delta TL}{V^2} \quad (6.3)$$

where  $g$  depicts the gravitational acceleration,  $\Delta T$  the temperature difference,  $L$  the characteristic length,  $\nu$  the kinematic viscosity,  $V$  the air velocity and  $\beta$  depicts the thermal expansion coefficient given by (ANSYS, 2012),

$$\beta = -\frac{1}{\rho} \frac{\partial \rho}{\partial T} \quad (6.4)$$

If the Archimedes number approaches unity or exceeds it, strong buoyancy forces can be expected. The strength of these buoyancy-driven flows is characterised by the Rayleigh number,

$$\text{Ra} = \frac{g\beta\Delta TL^3}{\nu^2\alpha} \quad (6.5)$$

where  $\alpha$  is the thermal diffusivity given by,

$$\alpha = \frac{k}{\rho c_p} \quad (6.6)$$

The parameters,  $\rho$ ,  $k$  and  $c_p$  depict the density, thermal conductivity and specific heat capacity, respectively. The Rayleigh number is used to investigate whether flow is turbulent or laminar. Laminar flow is expected for Rayleigh

numbers below  $10^8$ . The transition to turbulence occurs at  $10^8$  and extends over the range of  $10^8 < \text{Ra} < 10^{10}$ .

## 6.2.2 Modelling Buoyancy-driven Flow

For general purposes where buoyancy-driven flow is involved, a steady-state simulation using the Boussinesq model is usually adequate (ANSYS, 2012). The Boussinesq model specifies a constant density from which the mass flow can be obtained. However, the Boussinesq approximation is only valid for low to medium temperature differences. More specifically, given the Boussinesq approximation,

$$(\rho - \rho_0)g \approx -\rho_0\beta(T - T_0)g \quad (6.7)$$

where  $\rho_0$  depicts the operating density, it can be seen that the buoyancy term in the momentum equation,  $(\rho - \rho_0)g$  is approximated by the term on the right hand side of equation 6.7. The expression is formulated without the need to compute the operating density, but since it requires the operating temperature, large temperature differences will cause instability.

Alternatively, a transient simulation can be used where the density is computed from initial temperatures and pressures from which the density and, thus, mass flow can be computed. The operating density in the  $(\rho - \rho_0)g$  term of the momentum equation is computed from the following definition of pressure,

$$P'_s = P_s - \rho_0gx \quad (6.8)$$

and the solver finds the respective value for the operating density by averaging over the cells. For this method to work the initial density and pressure values need to be well defined. They need to be a good representation of the average value of all cells in the domain (ANSYS, 2012). The transient scheme is a robust method that can be used to solve developing flow as a 'first step' simulation, and once the flow has stabilised, the solver can be switched to steady state.

A more elegant solution is offered by using the pseudo-transient formulation. The pseudo-transient formulation is a steady-state formulation, but is more robust to account for complex plume developments. Good results were obtained using this model.

The pseudo-transient model, however, is only applicable to laminar flow. When transition flow or turbulent flow is modelled the default steady formulation or transient formulation is available.

To observe whether a formulation has converged, it is advised to not only investigate the monitor residuals but also the physical parameters, such as surface temperatures or flux imbalances (ANSYS, 2012).

## 6.3 Radiation Heat Transfer

### 6.3.1 Theory Background

The general radiative transfer equation (RTE) for an absorbing, emitting and scattering medium written in terms of its position vector and direction vector is given by,

$$\frac{\partial I(\mathbf{r}, \mathbf{s})}{\partial S} + (\alpha + \sigma_s)I(\mathbf{r}, \mathbf{s}) = \alpha n^2 \frac{\sigma T^4}{\pi} + \frac{\sigma_s}{4\pi} \int_0^{4\pi} I(\mathbf{r}, \mathbf{s}') \Phi(\mathbf{s} \cdot \mathbf{s}') d\Omega' \quad (6.9)$$

where,

$\mathbf{r}$  = position vector

$\mathbf{s}$  = direction vector

$\mathbf{s}'$  = scattering direction vector

$S$  = path length

$\alpha$  = absorption coefficient

$n$  = refractive index

$\sigma_s$  = scattering coefficient

$\sigma$  = Stefan-Boltzmann constant ( $5.669 \times 10^{-8} \text{ W/m}^2 \text{ K}^4$ )

$I$  = Radiation intensity

$T$  = local temperature

$\Phi$  = phase function

$\Omega$  = solid angle

The second, third and fourth term depict the radiation exchange due to absorption, emission and scattering.

### 6.3.2 Modelling radiation heat transfer

Two different radiation models were considered, namely the Surface-to-Surface (S2S) radiation model and the Discrete Ordinate (DO) model. The S2S model, as its name suggests, considers radiation exchange between surfaces where a view factor file is computed before the simulation is run. The view factor file is computed by means of an internal Monte Carlo ray-trace utility. The DO model makes use of the RTE equation as given by equation 6.9 and solves it for discretized values of the solid angle.

The S2S method is based on the principle that the net radiation energy incident on a surface,  $k$ , is obtained by summing the radiation energy contributed by all other surfaces,  $j$ , in the near surroundings.

$$Q''_{\text{in},k} = \sum_{j=1}^N F_{kj} Q''_{\text{out},j} \quad (6.10)$$

$F_{kj}$  denotes the 'surface-to-surface' view factor obtained from the integral, as given by,

$$F_{kj} = \frac{1}{A_k} \int_{A_k} \int_{A_j} \frac{\cos \theta_k \cos \theta_j}{\pi r^2} \delta_{kj} dA_k dA_j \quad (6.11)$$

where  $\delta_{kj}$  depicts the visibility function.  $\delta_{ij}$  is equal to one if  $dA_j$  is visible to  $dA_k$ , and zero if not. The energy leaving the respective surface is computed from equation 6.12.

$$Q''_{\text{out},k} = \epsilon_k \sigma_k T_k^4 + \rho_k \sum_{j=1}^N F_{kj} Q''_{\text{out},j} \quad (6.12)$$

The S2S model does not account for participating media and it treats all reflected radiation diffusely. A further limitation is that semi-transparent walls and non-grey radiation modelling cannot be performed. Since most of these features need to be incorporated, especially when modelling the effect of the quartz tubes, the DO model had to be utilized.

The DO model is the most advanced radiation model in FLUENT, which is the only model that can simulate non-grey, diffuse or specular radiation with opaque or semi-transparent walls and participating media.

The RTE equation solved by the DO model written in terms of non-grey radiation is depicted in equation 6.13,

$$\nabla \cdot (I_\lambda(\mathbf{r}, \mathbf{s}) \mathbf{s}) + (\alpha_\lambda + \sigma_s) I_\lambda(\mathbf{r}, \mathbf{s}) = \alpha_\lambda n^2 I_{b\lambda} + \frac{\sigma_s}{4\pi} \int_0^{4\pi} I_\lambda(\mathbf{r}, \mathbf{s}') \Phi(\mathbf{s} \cdot \mathbf{s}') d\Omega' \quad (6.13)$$

where the subscript  $\lambda$  denotes the wavelength and  $I_{b\lambda}$  the black body Intensity as found in Planck's spectral distribution of emissive power,

$$E_{b\lambda}(T) = \pi I_{b\lambda} = \frac{2\pi h c_o^2}{n^2 \lambda^5 \left[ \exp\left(\frac{hc_o}{nk_b \lambda T}\right) - 1 \right]} = \frac{2\pi C_1}{n^2 \lambda^5 \left[ \exp\left(\frac{C_2}{n\lambda T}\right) - 1 \right]} \quad (6.14)$$

$h$  denotes Planck's constant and has the value of  $h = 6.626\,068\,96 \times 10^{-34}$  J s. Boltzmann's constant is given by  $k_b = 1.380\,650\,4 \times 10^{-23}$  J/K. The auxiliary constants are defined as  $C_1 = hc_o^2 = 0.595\,521\,38 \times 10^8$  W  $\mu\text{m}^4/\text{m}^2$  sr and  $C_2 = hc_o/k_b = 14\,387.752$   $\mu\text{m}^4/\text{m}^2$  sr.

Equation 6.13 provides a value for  $I_\lambda \Delta\lambda$  after integrating over each respective wave-band, which is the radiation energy for that specific wave-band. Each wave-band is treated as grey radiation and the non-grey total radiation energy is a summation of the integrated grey radiation energy terms, as given by equation

$$I(\mathbf{r}, \mathbf{s}) = \sum_k I_{\lambda_k}(\mathbf{r}, \mathbf{s}) \Delta\lambda_k \quad (6.15)$$

The major limitation of the DO model is that it is computationally expensive, especially when the solid angle discretization is set to smaller octant values (ANSYS, 2012).

## 6.4 Flux Mapping Strategies

To date, FLUENT does not have built-in solar modelling capabilities that can be used for CSP applications. A solar load model has been developed but is restricted to general purpose applications such as flat plate collectors. The computational expense of setting up an entire heliostat field in FLUENT would be too high. Thus, the solar ray-tracing is typically performed using external platforms and the ray data imported into FLUENT.

The first modelling approach used was a highly simplified version. A script was written in SolTrace where a \*.csv file was generated that contained all the ray hitpoints on each tube element. The averaged flux was then set as the heat flux boundary condition in FLUENT, on the respective tube elements. Accordingly, the fluxes were set as uniform fluxes around the periphery of the tubes. Over-predicted surface temperatures were obtained for this method, especially on the rear side of each tube. In practice, only the front side of the tubes was irradiated, which caused the inaccuracy.

Further investigation was done on applying the collimated rays as the boundary condition in the DO model. In this case, the raw ray data from SolTrace could be applied as a single ray file into FLUENT without the need to set the boundary conditions on individual tube surfaces. This method, however, is considered to be highly inaccurate (Barbato, 2013). This is because even though a beam direction can be set in the DO model, the nature of the model causes the beam to dissipate.

According to Buck (2013), the German Aerospace Centre (DLR) has developed a specialised data transfer tool that couples Finite Element Mesh and CFD codes to their ray-trace utility by transferring the mesh data, called Finite Element Mesh Ray-tracing (FEMRAY) (Uhlig, 2009). The grid information is exported to the ray-tracer, and the flux information is transferred back into ANSYS. The DLR, however, does not distribute this software freely.

The method employed in this project was to generate the shadowing effect by means of flux projections along the tube surface. This was done by setting up a user-defined function (UDF) in FLUENT that loops over all the mesh faces on a tube element, gets the area vector, which is a Cartesian vector pointing normal to the respective face area, and multiplies the peak flux vector with the normalized area vector. The result is a projected flux vector  $[I_{xx}, I_{yy}, I_{zz}]$  parallel to the peak flux vector applied onto the local face area. The magnitude of the projected flux starts at unity, with the peak flux for face areas pointing normal to the incident peak flux vector, and decreases around the periphery of the tube until it is zero at face area vectors orthogonal to the



incident peak flux vector. The rear side of the tubes remain at zero. Figure 6.1 illustrates the method, where  $A$  depicts the area vector and  $I_y$  is the incident peak flux vector.

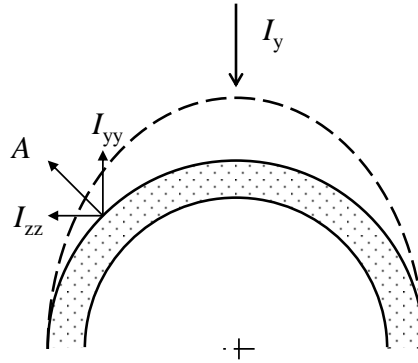


**Figure 6.1:** Illustration of flux projection of peak flux vector around periphery of tube

The equations for  $I_{xx}$ ,  $I_{yy}$  and  $I_{zz}$  are given as follows,

$$I_{xx} = I_x \frac{A_x}{\sqrt{A_x^2 + A_y^2 + A_z^2}} \quad (6.16)$$

$$I_{yy} = I_y \frac{A_y}{\sqrt{A_x^2 + A_y^2 + A_z^2}} \quad (6.17)$$

$$I_{zz} = I_z \frac{A_z}{\sqrt{A_x^2 + A_y^2 + A_z^2}} \quad (6.18)$$

## 6.5 Modelling Setup

Figure 6.2 depicts the receiver model, as used in ANSYS, with the accompanying named selections. It also shows the fluid domain inside the receiver. The domain boundaries were further extended (not shown in figure 6.2) out of the receiver to capture the buoyant plume development.

The top, bottom, left and right walls were discretized based on the ray-tracing results. The flux magnitudes from SolTrace were only applied to these parts of the walls. The rear cavity wall faces and duct wall faces were shadowed; thus the flux values absorbed by these walls were neglected. The rear cavity walls were assumed adiabatic, and the duct walls were given an external convective heat transfer coefficient of  $5 \text{ W/m}^2 \text{ K}$ . No windy conditions were assumed.

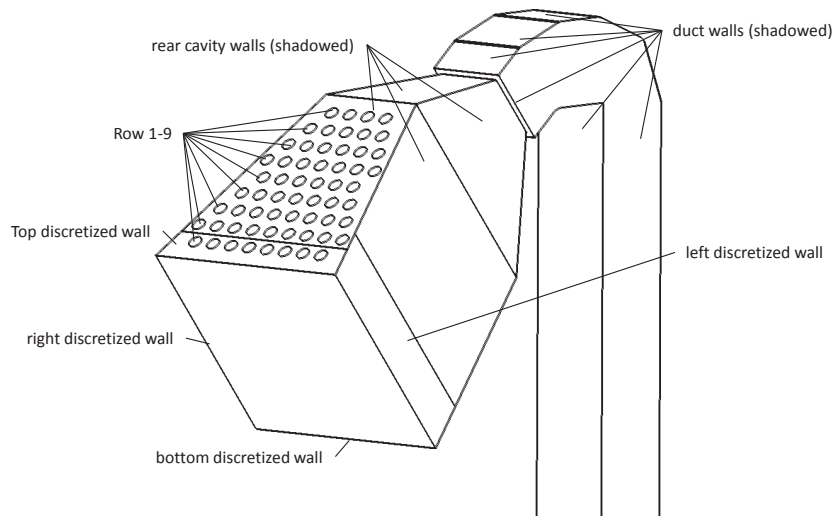


**Figure 6.2:** Illustration of named selections used in numerical model

### 6.5.1 General Assumptions

For the FLUENT model, it was initially assumed that laminar flow can be modelled. Here the laminar viscous model with the pseudo transient formulation was used. The solution converged quickly, and the solver did not reveal major stability issues while iterating. The solution was then used to investigate the validity of the assumption by means of computing the Rayleigh numbers, as discussed in section 6.2.1. This was done by defining a custom field function in FLUENT according to equation 6.5. The vertical height of the cavity was chosen as the characteristic length in the Rayleigh number equation. The other parameters, such as temperature and molecular viscosity, were defined as field functions such that FLUENT implements these values based on the local cell data.

The Rayleigh number contours showed that the flow exceeded the critical Rayleigh number of  $10^8$ , especially within the cavity. Based on the theory from section 6.2.1, the flow should be therefore modelled as transitional to turbulent flow. Accordingly, the realizable k-epsilon turbulence model was used.

The two-equation k-epsilon turbulence model is the most widely used turbulent model. It has three submodels, namely the standard k-epsilon model, the Renormalization Group theory (RNG) k-epsilon model and the realizable k-epsilon model. The realizable k-epsilon model was chosen over the other two because it more accurately predicts rotating flows, boundary layers under strong adverse pressure gradients, separation and recirculation (ANSYS,

2012). Recent experiences have shown that the realizable k-epsilon model provides the best performance of all k-epsilon models for flows with complex secondary flow features (ANSYS, 2012).

The results for both laminar and turbulent models, however, were compared to investigate the impact on the physical nature of the problem when changing between the two models. This is presented in chapter 7.

The radiation exchange between opaque surfaces is treated as diffuse, grey radiation. The quartz wafers are modelled as semi-transparent media with non-grey wave-bands. The non-grey nature of the quartz is essential in determining whether quartz is capable of acting as a radiation shield or not. Air is modelled as participating media, even though the impact of air on the radiation exchange is not expected to have a significant influence. The relevant equations for modelling the radiative heat transfer were outlined in section 6.3.2.

### 6.5.2 Meshing

For all receiver models the proximity-based meshing method was used. Because all the tubes and cavity walls are in close proximity compared to the domain boundaries, the software automatically generated the mesh sizes accordingly. Inflation layers were added onto the tube boundaries to ensure sufficient face cells for the radiation solver and to provide sufficient volume cells for the near wall boundary layer flow computation. The number of nodes and elements were in the order of 1 million. A mesh sensitivity analysis was performed to investigate the validity of the mesh. 1 million cells provided acceptable accuracies and were close to the highest number cells that the machine could account for without major delays during the model setup.

### 6.5.3 Material Properties

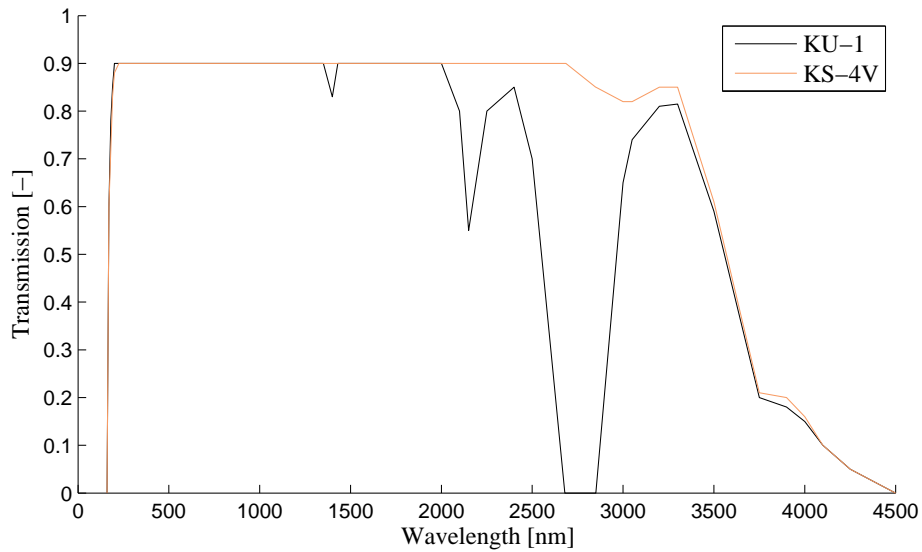
The optical properties for the mirror glass were chosen as presented in table 5.1. Since the absorber tubes are coated with carbon black paint (NS-7) the optical properties for the absorber tubes were obtained from the specifications of NS-7, i.e. reflectivity of 4% and transmissivity of zero (Pompea and Breault, 1995). The reflectivity of the quartz was modelled as 7% and the transmissivity within the visible light spectrum was modelled as 90%, as obtained from Tydex (2013). The reflectivity of stainless steel was chosen as 0.6. It is difficult to predict this value as it ranges from 0.4 to 0.7 for wavelengths of 400 nm to 700 nm according to Okić *et al.* (1987), and it is highly dependent on surface finishes. The material specifications for the setup in FLUENT is highlighted in table 6.1.

Four wave bands were defined for the non-grey radiation model as discussed in chapter 7. The first wave band ranged between 0.001  $\mu\text{m}$  and 2.75  $\mu\text{m}$  with a transmissivity value of 0.9, the second wave band ranged between 2.75  $\mu\text{m}$  and 3.25  $\mu\text{m}$  with a transmissivity value of 0.82, the third wave band ranged

**Table 6.1:** Material properties of quartz glass , ceramic insulation and stainless steel as used in FLUENT (Kitamura *et al.*, 2007; Tydex, 2013; Omega, 2013; Nutec, 2009; ANSYS, 2012))

Property	Unit	Quartz	Ceramic	Steel
density	[kg/m <sup>3</sup> ]	2203	1260	-
thermal conductivity	[W/m K]	1.3	0.19	-
specific heat capacity	[J/kg K]	703	1500	-
refractive index	[-]	1.45	-	-
absorption coefficient	[-]	gray-band	-	-
emissivity	[-]	0.9	-	0.88

between 3.25  $\mu\text{m}$  and 3.75  $\mu\text{m}$  with a transmissivity value of 0.5 and the last wave band ranged between 3.75  $\mu\text{m}$  and 100  $\mu\text{m}$  with a transmissivity value of 0.1. The transmission curve for infra-red graded (KS-4V) and ultra-violet graded (KU-1) fused silica quartz, as obtained from Tydex (2013), is presented in figure 6.3. The curves are given based on a sample thickness of 10 mm.

**Figure 6.3:** Transmission curve of fused silica quartz glass as obtained from Tydex (2013)

The absorption coefficient for each wave band was then calculated from the equation given below (Ho, 2008),

$$\alpha = \left[ -\ln(\tau) \frac{1}{6} \frac{1000}{1} \right] 1/\text{m} \quad (6.19)$$

where  $\tau$  depicts the transmissivity and 166 is used to convert from  $\text{cm}^{-1}$  to  $\text{m}^{-1}$ . The quartz wafers had a diameter of 6 mm.

The fluid properties of air were taken from the FLUENT database. All properties were kept as default, apart from the density which was changed from constant to an incompressible ideal gas. Thus, density variation is computed from change in local temperature and pressure, which is essential for modelling buoyancy-driven flow.

### 6.5.4 Boundary Conditions

The boundary conditions for the far field domain boundaries were set at pressure outlet boundaries. This gave rise to some solving uncertainty as some of the boundary faces experienced reverse flow. Two ways to overcome this problem is to either introduce a small breeze that forces the flow into one direction or to further enlarge the entire domain and set the boundaries as wall boundaries. The latter option would provide better mass conservation, and thus the continuity residuals would further decrease. Preference, however, was given to the use of a smaller domain with fewer cells and nodes. The residuals also converged to an order of  $10^{-3}$ , which is sufficient. The wall flux boundary conditions were obtained from SolTrace with a DNI of  $940 \text{ W/m}^2$ , as recorded on 30 July 2013 for the receiver excluding the quartz wafers, and  $830 \text{ W/m}^2$ , as recorded on 1 August 2013 for the receiver including the quartz wafers. The fluxes are presented in tables 6.2 and 6.3.

**Table 6.2:** Flux profiles for wall boundary conditions of fully packed tube receiver as recorded on 30 July with a DNI value of  $940 \text{ W/m}^2$  for the fully packed receiver model

Wall ID	Peak Flux [ $\text{W/m}^2$ ]	Average Flux [ $\text{W/m}^2$ ]
wall_row_1	89 068.7	-
wall_row_2	56 374.35	-
wall_row_3	19 905.95	-
wall_row_4	5525.026	-
wall_row_5	3936.5	-
wall_row_6	2905.9	-
wall_row_7	1687.5	-
wall_row_8	1295.8	-
wall_row_9	899.1	-
wall_bottom	-	200
wall_top	-	180
wall_left	-	11 290
wall_right	-	11 180

**Table 6.3:** Flux profiles for wall boundary conditions of the quartz receiver as recorded on 1 August with a DNI value of  $830 \text{ W/m}^2$ 

Wall ID	Peak Flux [ $\text{W/m}^2$ ]	Average Flux [ $\text{W/m}^2$ ]
wall_row_1	10 515	-
wall_row_2	10 044	-
wall_row_3	7720	-
wall_row_4	38 465	-
wall_row_5	13 639	-
wall_row_6	7218	-
wall_row_7	2720	-
wall_row_8	1977	-
wall_row_9	1237	-
wall_bottom	-	37
wall_top	-	32.7
wall_left	-	4550
wall_right	-	4380

### 6.5.5 Solution Methods

The coupled scheme was chosen for the laminar model with pseudo transient formulation. This is to enable the pressure-velocity coupling. The simple scheme was chosen for the realizable k-epsilon model. In both models the body-force weighted pressure discretization was enabled, which is typical for buoyancy-driven flow modelling. First order implicit schemes were given preference to the momentum discretizations where the solver might experience some stability issues, and the second order implicit schemes were chosen for the energy and DO intensity discretizations, where fewer stability issues are expected.

### 6.5.6 Residuals

The residuals for the turbulent model with an externally forced airflow of  $2.3 \text{ m/s}$  reached the convergence criteria of 0.001 after about 350 iterations for the energy and DO intensity equations, and after about 700 for the momentum equations. The mass and energy balances, discussed in section 6.6.2, also revealed that the solver converged.

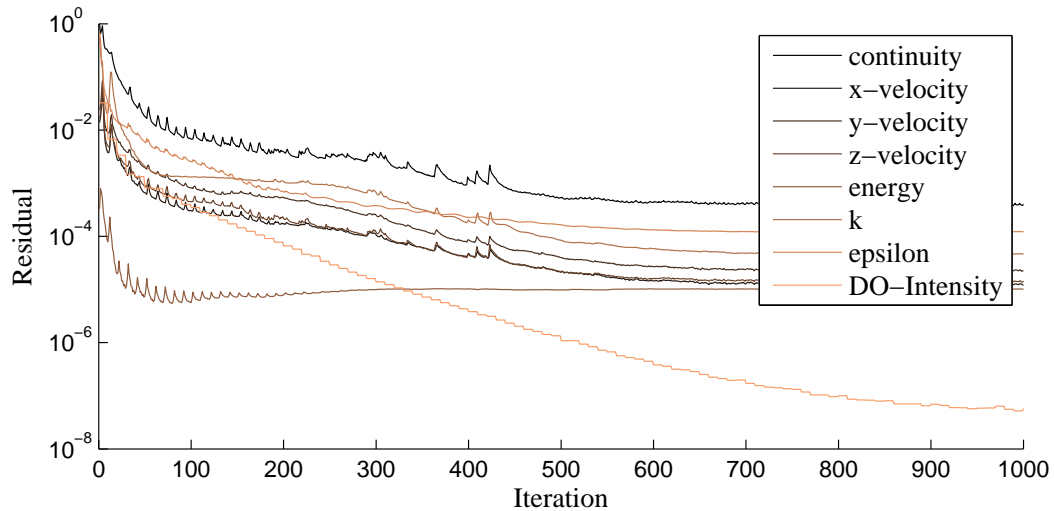


**Figure 6.4:** Residual plot of simulation run for externally forced airflow conditions of receiver as recorded on 30 July 2013 with a DNI value of  $940 \text{ W/m}^2$ , with the k-epsilon turbulent model

## 6.6 Numerical Results

### 6.6.1 Contour Plots

Figure 6.5 and figure 6.6 illustrate the temperature contour plot of the receiver for case I and case II, as tested on 30 July with a DNI value of  $940 \text{ W/m}^2$ .

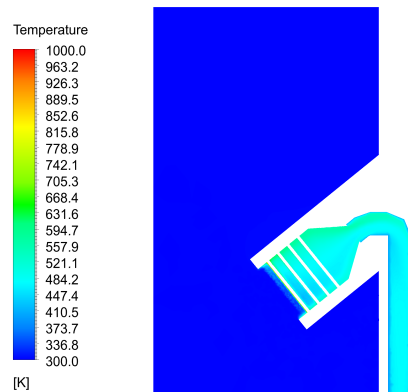


**Figure 6.5:** Temperature contour plot of receiver with forced airflow and no quartz wafers (case I)

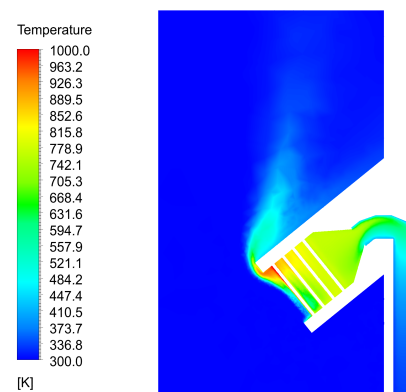


**Figure 6.6:** Temperature contour plot of receiver without forced airflow and no quartz wafers (case II)

The contour planes are defined at the centre of the receiver. The cavity wall and tube surfaces are not included. The temperature range of the contours

was fixed to 300 K and 1000 K as upper and lower limit, for better comparison.

One can see that the forced airflow effectively removes the buoyant plumes from escaping the receiver. The energy carried by the plumes would be lost to the environment, but is instead recovered for use in a thermal storage or other applications. It was also found that the fluid temperatures through the receiver reduced from 800 K to 500 K. This is because the cavity no longer has stagnating zones.

Figures 6.7 and 6.8 illustrate the temperature contour plots of the quartz receiver, as given by cases III and IV respectively.

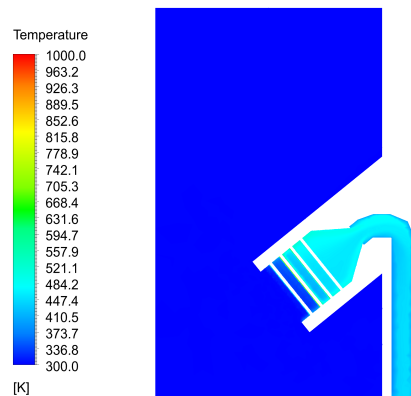


**Figure 6.7:** Temperature contour plot of receiver including quartz wafers and forced airflow (case III)

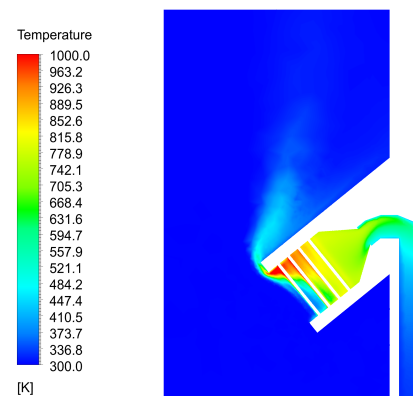


**Figure 6.8:** Temperature contour plot of receiver including quartz wafers and no forced airflow (case IV)

When comparing figure 6.5 with figure 6.7 one can see that, for the quartz receiver, air temperatures only start increasing at a certain depth into the receiver. In contrast, case I already experiences hot airflow after the first row. Similarly, when comparing case II in figure 6.6 with case IV in figure 6.8, one can see that more hot air gathers inside the quartz receiver than the fully packed tube receiver. Again, energy is allowed to penetrate deeper into the cavity and, thus, the escape of hot plumes is less likely to occur.

It should further be noted that cases III and IV were modelled with a DNI value of  $830 \text{ W/m}^2$ , as tested on 1 August 2013 for the quartz receiver. The total energy applied to the quartz model was, therefore, 12% less than the total energy applied to fully packed receiver model, which was modelled with a DNI value of  $940 \text{ W/m}^2$ .

## 6.6.2 Flux Reports

The flux reports in FLUENT have shown that the quartz receiver, as depicted by case III, showed significant improvements on the efficiency of the receiver,



compared to the fully packed receiver from case I. The radiation heat transfer rate across the external domain boundaries was much lower for case III than for case I. The convection heat transfer rate across the boundaries, on the other hand, was almost identical for both cases. The total heat transfer rate for cases II and IV, across the external domain boundaries, added up to a value similar to the incident power predicted by SolTrace. This is because no energy is extracted from the receiver.

The flux maps further showed that for case III and case IV, row 4 emitted the highest power followed by row 5 and row 6. In contrast, the model excluding the quartz tubes showed that the highest emissive power is experienced in the first row, and ,thus, significant radiation losses are obtained.

## 6.7 Conclusion

The work presented in this chapter included a brief theoretical background on buoyancy-driven flow and radiation heat transfer and how this is typically modelled in computational fluid dynamics. Various flux mapping strategies have been outlined, of which one was chosen that formed a simple and intermediate solution to the problem. Future projects would have to consider developing more extensive flux mapping tools for better accuracy. Finally, the modelling setup and numerical results have been presented.

It was shown that the HPAR concept successfully eliminates convection losses by means of an externally forced flow. Flux reports have further shown that significant improvements are expected when the HPAR concept makes use of quartz glass wafers. Chapter 7 addresses the validity of these numerical results.

# Chapter 7

## Empirical Validation

### 7.1 Introduction

The numerical results were validated experimentally with a model of the receiver. The flux source for the receiver was obtained using a locally developed solar concentrator. The description and characterisation of the concentrator was presented in chapter 5. The work presented in this chapter provides a comparison between the empirical results and the numerical results from chapter 6.

### 7.2 Experimental Setup

To provide an externally forced airflow on the receiver model a small-scale tower facility was designed and constructed utilizing an in-line duct fan. Because the fan was limited to air temperatures of 40 °C, the test setup further included a thermal storage that cooled down the air temperature, prior to entering the fan. It was decided to make use of a small-scale rockbed. This would allow tests to be conducted for about 20 min. A fan speed controller was also added to the system to regulate the flow velocity. The fan size was chosen based on the system impedance calculations presented in appendix E. Moreover, a venturi flow meter was designed, constructed and calibrated. This work is also presented in appendix E.

A circular guide rail was constructed to allow more accurate azimuth-tracking of the concentrator. Figure D.11 in appendix D shows that the tracking was successfully performed. A screw mechanism was used to provide the zenith tracking. Unfortunately, the screw mechanism has a limited range which only allowed operation for 2 h before and after solar noon. Also, the mirrors of the concentrator require recalibration every 4-6 weeks due to the sun's varying orbit. The testing time for all the experiments was therefore limited.

The experimental data was obtained from 5 thermocouple probes placed on the interior of the tubes. The 5 thermocouples were positioned at the central positions of rows 1, 2, 4, 6 and 9.

Figure 7.1 is a photograph of the rig, illustrating the different components used in the experiments.

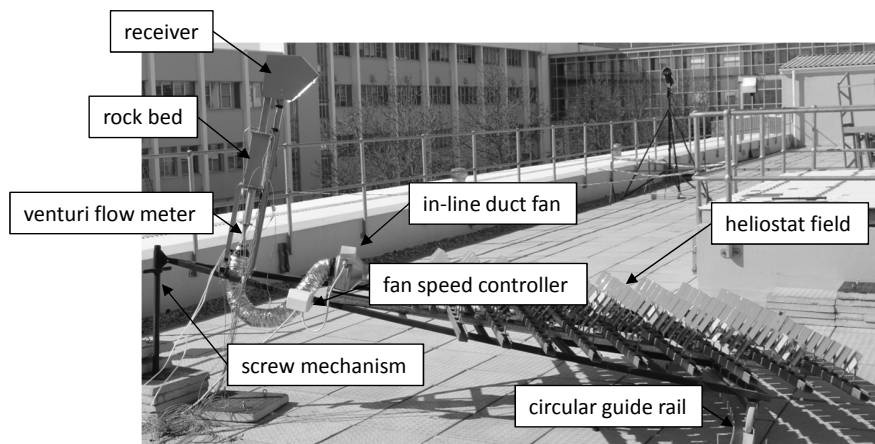


**Figure 7.1:** Image of medium flux solar concentrator

### 7.3 Experimental Results

Chapter 6 highlighted that buoyancy-driven flow is often modelled using laminar flow models, and turbulent models should be considered only if the Rayleigh number exceeds  $10^8$ . Initially, a laminar model was used, for which reasonable results were obtained, even though the Rayleigh numbers exceeded  $10^8$ . For this reason, a turbulent model was also considered. The comparison between the two models showed that for the flow conditions in this project, both models provide similar results, as can be seen in figure 7.2.

The plot shows averaged tube temperatures plotted against tube rows from row 1 at the front of the receiver to row 9 at the rear of the receiver. The two models correspond well with the empirical data obtained for the receiver model as tested on 30 July, including a reverse air flow of 2.3 m/s (case I from section 4.7).

Less accurate results have been obtained for the same receiver setup without quartz wafers but also without the external forced air flow (case II). Figure 7.3 illustrates that the turbulent and laminar models deviate slightly from each other in the rear section of the receiver, but significant deviation occurs between the empirical data and the numerical results.

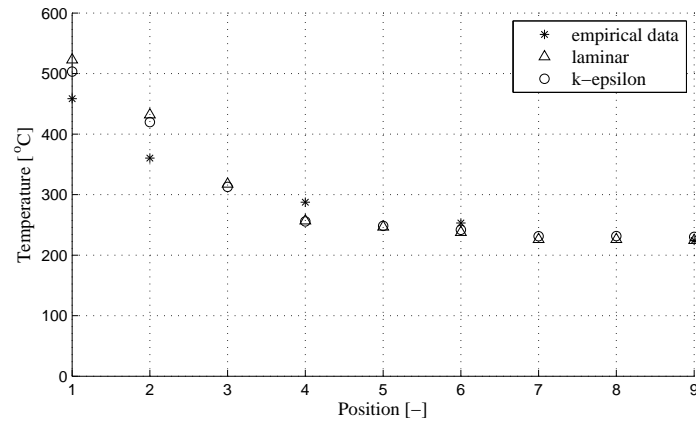


**Figure 7.2:** Surface temperature distribution of receiver excluding quartz rows as tested on 30 July 2013 with a DNI value of  $930 \text{ W/m}^2$  and reverse air flow of  $2.3 \text{ m/s}$  (case I)

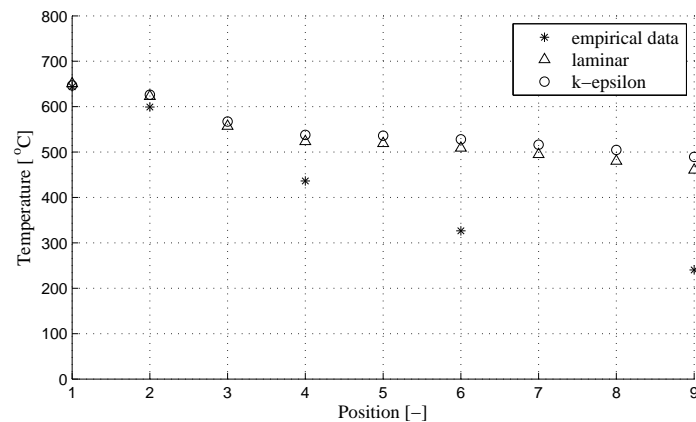


**Figure 7.3:** Surface temperature distribution of receiver excluding quartz rows as tested on 30 July 2013 with a DNI value of  $940 \text{ W/m}^2$  and no forced airflow (case II)

The major cause for the deviation between the empirical data and the numerical results is believed to be that the system takes longer than the test duration to reach steady state at stagnation conditions. The transient response curves for case I and case II show that the system indeed did not fully reach steady state, especially in the rear portion of the receiver. These curves are depicted in figures 7.4 and 7.5.

One can see that the first 4 rows of the receiver reached 'near' steady state more rapidly than the rows situated deeper into the receiver. Accordingly, even though the tests were conducted for a longer period of time for the receiver without the external forced flow, 1800 s compared to 1200 s, the rear tube temperatures did not fully reach steady state. The presence of the rear ducting system further increased the transient time as continuous cool air

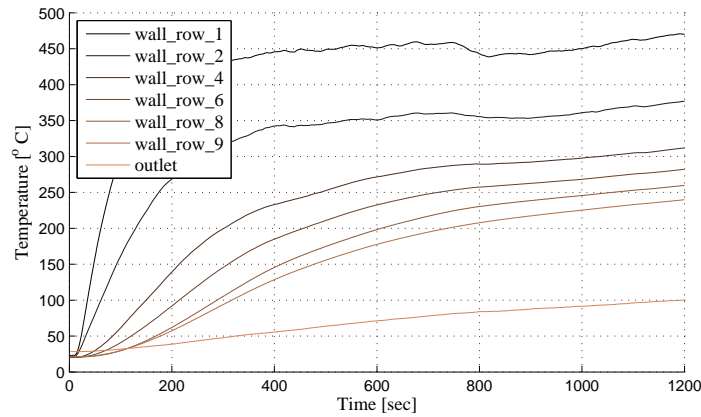


**Figure 7.4:** Transient response of fully packed receiver as tested on 30 July at 12:17:52 PM for 1200 sec with an averaged DNI value of  $930 \text{ W/m}^2$  and forced airflow of  $2.3 \text{ m/s}$  (case I)

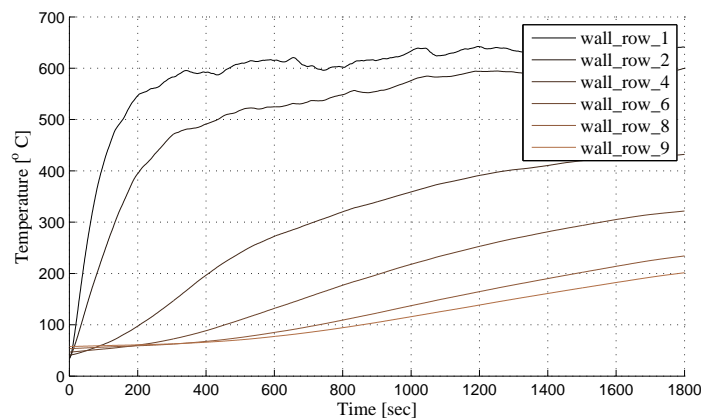


**Figure 7.5:** Transient plot of fully packed receiver as tested on 30 July at 13:19:09 PM for 1800 sec with an averaged DNI value of  $940 \text{ W/m}^2$  and no forced airflow (case II)

slowly entered the cavity from the ducting system.

The tests further showed that the maximum temperatures in the receiver occurred in the front row of the receiver and amounted to about  $450 \text{ }^\circ\text{C}$  to  $500 \text{ }^\circ\text{C}$  for the case where a reverse air flow of  $2.3 \text{ m/s}$  was applied and approximately  $650 \text{ }^\circ\text{C}$  for the case where stagnation conditions existed. It should be noted that neither the temperature data points of the empirical data nor the temperature data points of the numerical results showed the aspired volumetric effect curve from chapter 4.

As discussed earlier, a thermal rockbed had to be included in the design because the suction fan was restricted to air temperatures below  $40 \text{ }^\circ\text{C}$ . The 'outlet' curve in figure 7.4 shows the temperature measurement of the air flow

entering the rockbed. Air temperatures of about  $100\text{ }^{\circ}\text{C}$  were measured after 1200 s of testing. The fan then was switched off as the temperature of the air stream at the outlet of the rockbed started to rise towards  $40\text{ }^{\circ}\text{C}$ .

In comparison, the 'outlet' curve for the receiver model as tested on 1 August, presented in figure 7.6, shows that about  $94\text{ }^{\circ}\text{C}$  were reached within that time frame when the quartz glass wafers are included.

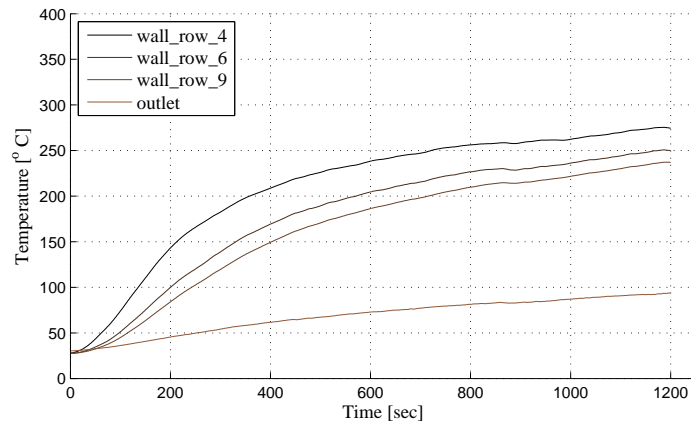


**Figure 7.6:** Transient response of receiver with quartz rows as tested on 1 August 2013 with a DNI value of  $830\text{ W/m}^2$  and reverse airflow of  $2.3\text{ m/s}$  (case III)

These results were obtained for a DNI value of  $830\text{ W/m}^2$ , averaged over the time of testing. The maximum temperatures for this case were recorded in row 4 and amounted to  $285\text{ }^{\circ}\text{C}$ . Unfortunately, the temperature of the quartz glass wafers could not be measured. However the numerical results, shown in figure 7.7, suggest that the temperatures of the quartz wafers are not expected to exceed the temperatures of the opaque tubes.

It can be assumed that the maximum temperatures in the quartz receiver for case III are significantly lower than the temperatures in case I, i.e.  $285\text{ }^{\circ}\text{C}$  compared to  $500\text{ }^{\circ}\text{C}$ , respectively. The implication of this finding is that the receiver model including quartz wafers would still be suitable for much higher flux densities.

For the sake of discussion, assuming a limited material temperature of  $500\text{ }^{\circ}\text{C}$ , the flux density on the fully-packed receiver from case I would be at its maximum and a fluid outlet temperature of around  $100\text{ }^{\circ}\text{C}$  would be obtained. The quartz receiver from case III, however, would be able to accommodate much higher flux densities because its material temperature can be increased from  $285\text{ }^{\circ}\text{C}$  to the upper limit of  $500\text{ }^{\circ}\text{C}$ . For  $500\text{ }^{\circ}\text{C}$  material temperature in the quartz receiver, much higher fluid outlet temperatures can be expected, which makes the quartz receiver type from case III the better option.

Figure 7.7 further shows the comparison between the empirical data and the numerical model. Here, a non-grey radiation model was used where the quartz

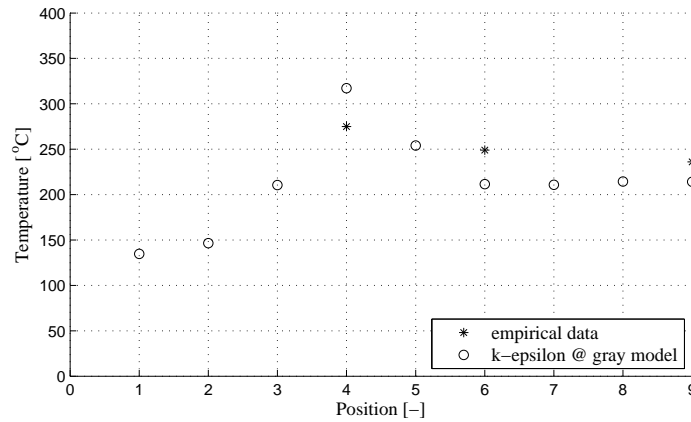


**Figure 7.7:** Surface temperature distribution of receiver including the first three rows of quartz as tested on 1 August 2013 with a DNI value of  $830 \text{ W/m}^2$  and reverse air flow of  $2.3 \text{ m/s}$  (case III)

wafers were modelled as semi-transparent media. Four different wave bands were defined based on the transmission curve of quartz glass, as discussed in section 6.5.3. Fair agreement between the numerical model and the empirical data was obtained.

Similar results have been obtained for the receiver, including quartz wafers at stagnation conditions, as shown in figure 7.8.

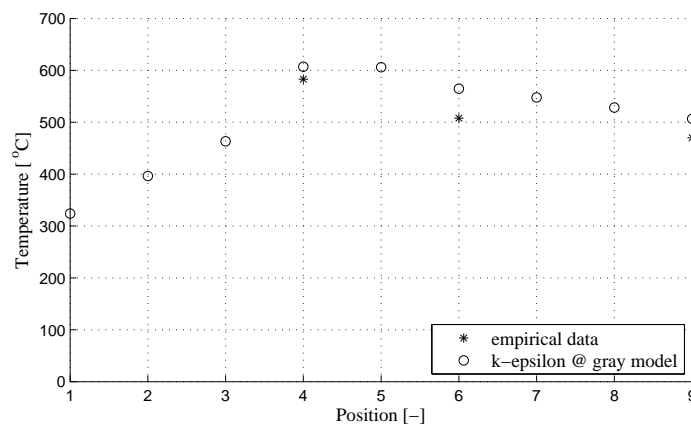


**Figure 7.8:** Surface temperature distribution of receiver including the first three rows of quartz as tested on 1 August 2013 with a DNI value of  $830 \text{ W/m}^2$  and no forced airflow (case IV)

When comparing figure 7.8 with figure 7.5 one can see that case IV provides better agreement with the empirical data than case II. This is because a longer testing time of up to  $6000 \text{ s}$  was conducted, compared to  $1800 \text{ s}$  for case II. The transient response of case IV is depicted in figure 7.9.

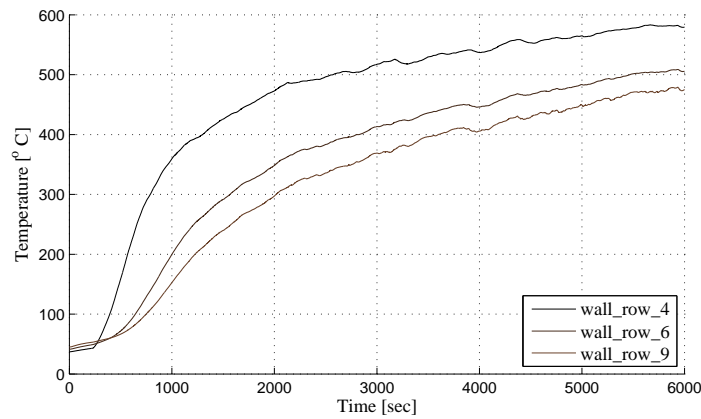


**Figure 7.9:** Transient response of receiver with quartz rows as tested on 1 August 2013 with a DNI value of  $830 \text{ W/m}^2$  and no forced airflow (case IV)

## 7.4 Conclusion

Based on visual inspection during testing, it was found that the reverse air flow eliminates the escape of buoyant plumes. The empirical results further showed that for similar air outlet temperatures between the receiver module including the quartz wafers and the receiver module excluding the quartz wafers, the maximum temperatures inside the receiver were significantly lower for the case where quartz wafers were included.

The numerical results have generally correlated well with the empirical data, although further research is required to refine the numerical model for more accurate results.



# Chapter 8

## Conclusion

### 8.1 Conclusion

An extensive review has shown that there is room for improvement on current receiver technologies for power towers. The HPAR concept was derived from the information found in literature combined with the results obtained from a parametric analysis. Sensitivities on how to improve the efficiency of a central receiver revealed the importance of the view factor and the external heat transfer coefficient. Additionally, higher flux densities contribute to higher efficiencies as the receiver size can be reduced.

Coupled natural convection and radiation heat transfer simulations demonstrated that the HPAR successfully removes major convection losses by an external forced convection flow into the receiver. The reverse air flow further provides control over the allowable flux densities as the frontal absorber tubes are effectively cooled. The numerical model also investigated the effect of replacing the front absorber tubes with semi-transparent fused quartz wafers. Results showed that extinction of light occurs more gradually along the depth of the receiver.

Empirical results revealed that for similar air outlet temperatures, the maximum surface temperature inside the receiver, including the quartz wafers, was significantly lower than for the case where no quartz wafers were used. These findings validated that the HPAR concept can accommodate higher flux densities.

### 8.2 Research Contribution and Outlook

The research output from this project has resulted in two conference papers and a full international patent (Kretzschmar and Gauché, 2012; Kretzschmar *et al.*, 2012). The conference papers were presented at the South African Solar Energy Conference (SASEC) in Stellenbosch (South Africa) in May 2012 and at SolarPACES in Marakech (Marocco) in September 2012, respectively. Further

publications related to the HPAR concept and work presented in this thesis can be found in Mouzouris *et al.* (2012), Heller and Gauché (2013) and Craig *et al.* (2013).

A research program was created at the University of Pretoria that, among other projects, aims to further investigate the HPAR concept on performance and cost. Several MEng and PhD projects that address these issues are currently in progress. An additional provisional patent was submitted regarding an idea of a dual-pressure power cycle which was derived from the SUNSPOT cycle. The HPAR could potentially feature in this idea. This power cycle is currently being investigated in a PhD project at the Stellenbosch University.

### 8.3 Recommendations

The work presented in this project investigated the HPAR concept based on its functionality. The optimisation of the design has not been considered. It is therefore recommended that optimisation strategies are applied to the HPAR where the objective function is set for maximum heat transfer and exergetic efficiency.

More extensive research should be conducted on the use of quartz glass as a radiation shield. The work presented in this study considered round cylindrical quartz wafers. Alternatively, triangular prismatic geometries should be investigated where the sharp edges are pointed towards the incident flux. The idea is that reflection losses can be minimized.

The HPAR patent includes a feature for allowing the excess heat contained in the outlet air stream from the heat recovery system to be re-injected into the receiver air-return loop. This feature was considered beyond the scope of this project, and thus research is required to find an optimum air-return loop system.

Based on the results obtained from this project, the use of headers allows the HPAR to have a distinctive advantage over other receivers. Typical tubular receivers generally face burnout if the mass flow rate inside the tubes is too low. For the HPAR, however, the surface temperature on the tubes can be additionally regulated by varying the external flow. It is therefore recommended to consider a HPAR tower design where headers are used.

Numerical models should further consider the scale-up of the HPAR to MW sizes, and the concept should be tested on an actual pilot plant.

# Appendices

# Appendix A

## Correlations for Fluid Properties

This section presents the correlations for the thermal fluid properties of air, sodium and solar salt.

### A.1 Air

#### A.1.1 Density

The correlation for the density of air was taken from the ideal gas law, based on the assumption that air remains an incompressible fluid. It is given in units of [kg/m<sup>3</sup>].

$$\rho = \frac{P_{\text{atm}}}{R_{\text{air}}T} \quad (\text{A.1})$$

#### A.1.2 Dynamic Viscosity

The correlation for the dynamic viscosity of air was obtained from Kröger (2004). It is given in units of [Pa s].

$$\mu = 2.288 \times 10^{-6} + 6.259\,793 \times 10^{-8}(T/\text{K}) - 3.131\,956 \times 10^{-11}(T/\text{K})^2 + 8.150\,38 \times 10^{-15}(T/\text{K})^3 \quad (\text{A.2})$$

#### A.1.3 Conductivity

The correlation for the conductivity of air was obtained from Kröger (2004). It is given in units of [W/m K].

$$k = -4.937\,787 \times 10^{-4} + 1.018\,08 \times 10^{-4}(T/\text{K}) + 4.627\,937 \times 10^{-8}(T/\text{K})^2 + 1.250\,603 \times 10^{-11}(T/\text{K})^3 \quad (\text{A.3})$$

### A.1.4 Specific Heat

The correlation for the specific heat of air was obtained from Kröger (2004). It is given in units of [J/kg K].

$$c_p = 1045.356 - 0.316\,178\,3(T/\text{K}) + 7.083\,814 \times 10^{-4}(T/\text{K})^2 - 2.705\,209 \times 10^{-7}(T/\text{K})^3 \quad (\text{A.4})$$

## A.2 Sodium

### A.2.1 Density

The correlation for the density of sodium was obtained from Boerema *et al.* (2012). It is given in units of [kg/m<sup>3</sup>].

$$\rho = 219 + 275.32(1 - T/2503.7 \text{ K}) + 511.58(1 - T/2503.7 \text{ K})^{0.5} \quad (\text{A.5})$$

### A.2.2 Viscosity

The correlation for the viscosity of sodium was obtained from Boerema *et al.* (2012). It is given in units of [Pas].

$$\mu = \exp(-6.4406 - 0.3958 \log(T/\text{K}) + 556.835 \text{ K}/T) \quad (\text{A.6})$$

### A.2.3 Thermal Conductivity

The correlation for the thermal conductivity of sodium was obtained from Boerema *et al.* (2012). It is given in units of [W/m K].

$$k = 124.67 - 0.11381(T/\text{K}) + 5.5226 \times 10^{-5}(T/\text{K})^2 - 1.1842 \times 10^{-8}(T/\text{K})^3 \quad (\text{A.7})$$

### A.2.4 Specific Heat

The correlation for the specific heat of sodium was obtained from Boerema *et al.* (2012). It is given in units of [J/kg K].

$$c_p = (1.6582 - 8.4790 \times 10^{-4}(T/K) + 4.4541 \times 10^{-7}(T/K)^2 - 2992.6(T/K)^{-2})1000 \quad (\text{A.8})$$

## A.3 Solar Salt

The thermal properties and correlations for solar salt have been obtained from Wagner (2008).

### A.3.1 Density

The correlation for the density of solar salt was obtained from Wagner (2008). It is given in units of [kg/m<sup>3</sup>].

$$\rho = -0.6481(T/K) + 2269.4 \quad (\text{A.9})$$

### A.3.2 Viscosity

The correlation for the viscosity of solar salt was obtained from Wagner (2008). It is given in units of [Pa s].

$$\mu = (22.714 - 0.12t/^{\circ}\text{C} + 0.0002281(t/^{\circ}\text{C})^2 - 0.0000001474(t/^{\circ}\text{C})^3)/1000 \quad (\text{A.10})$$

### A.3.3 Thermal Conductivity

The correlation for the thermal conductivity of solar salt was obtained from Wagner (2008). It is given in units of [W/m K].

$$k = 0.443 + 0.00019t/^{\circ}\text{C} \quad (\text{A.11})$$

### A.3.4 Specific Heat

The correlation for the specific heat of solar salt was obtained from Wagner (2008). It is given in units of [J/kg K].

$$c_p = (1.443 + 0.000172t/^{\circ}\text{C})1000 \quad (\text{A.12})$$

## Appendix B

# Development of an Internal Pipe Flow Model and Validation

### B.1 Introduction

The work presented here was used in chapter 3 to investigate the effect of varying certain parameters on the internal heat transfer of a tubular receiver. It consists of three sections. In the first section the mathematical equations are presented. These are followed by the program structure and also a description on how the program was validated.

### B.2 Mathematical Model

A system's performance can be evaluated by considering incoming and outgoing energy terms. Based on the conservation of energy principle these terms always add up to zero. Therefore, for a certain incident energy, if losses are minimized more useful energy can be extracted. The most simplified energy equation is given by,

$$\dot{Q}_u = A_r S - \dot{Q}_l \quad (\text{B.1})$$

where,

$\dot{Q}_u$  = useful energy absorbed [W]

$A_r$  = area of the collective absorber tube [m<sup>2</sup>]

$S$  = Incident solar flux per unit area [W/m<sup>2</sup>]

$\dot{Q}_l$  = heat losses [W]

The area of the concentrating aperture constitutes the sum of all the heliostat mirrors. The optical losses from the heliostats are included in the overall solar flux term. Figure B.1 illustrates these incoming and outgoing energy terms on the receiver.

The overall heat losses can be further defined by

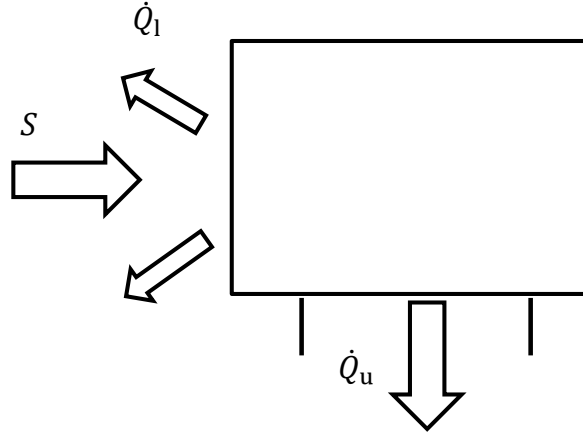


**Figure B.1:** Illustration of major energy terms incident and emitted from the receiver

$$\dot{Q}_1 = U_1 A_r (T_s - T_a) \quad (\text{B.2})$$

where,

$U_1$  = Overall heat loss coefficient [W/m K]

$T_s$  = Average surface temperature of absorber tubes [K]

$T_a$  = Temperature of the surrounding air [K]

Equation B.1 can therefore be combined with equation B.2 to give

$$\dot{Q}_u = A_r [S - U_1 (T_s - T_a)] \quad (\text{B.3})$$

Equation B.3 is a formulation of the energy terms for the external portion of the absorber tubes. The heat transfer, however, can also be formulated in terms of the energy transfer towards the working fluid on the interior of the tube, given by

$$\dot{Q}_u = U_o A_r (T_s - T_f) \quad (\text{B.4})$$

where  $T_f$  denotes the local fluid temperature. The overall internal loss coefficient is developed by considering thermal resistances through the tube wall and, thus,  $U_o$  is obtained as,

$$U_o = \left[ \frac{D_o}{h_{fi} D_i} + \frac{D_o \ln(D_o/D_i)}{2k} \right]^{-1} \quad (\text{B.5})$$

where,

$D_o$  = outside tube diameter [m]

$D_i$  = inside tube diameter [m]

$h_{fi}$  = fluid convective heat transfer coefficient [W/m K]



$k$  = thermal conductivity of the fluid [W/m K]

The internal heat transfer coefficient is calculated based on the well developed correlations for internal pipe flow. For a given mass flow rate, temperature dependant fluid properties and internal tube diameter, the Reynolds number can be obtained. Subsequently, the Nusselt number is obtained from

$$\text{Nu} = 0.023\text{Re}^{1/2}\text{Pr}^{1/3} \quad (\text{B.6})$$

for  $\text{Re} > 2300$ .  $\text{Pr}$  is the Prantdl number at the respective fluid temperature. This equation is also called the Dittus Boehlter equation (Cengel, 2006). Finally, the internal heat transfer coefficient is obtained by

$$h_{\text{fi}} = \frac{k\text{Nu}}{D_i} \quad (\text{B.7})$$

For Reynolds number  $\text{Re} < 2300$ , the Nusselt number is given a value of 3.6.

### B.2.1 Collector Efficiency Factor

Since the surface temperature of the absorber tube varies significantly with the concentrated solar flux as well as the mass flow rate through the tubes, its value is not easily accessible. Therefore, equation B.4 is rearranged and substituted into equation B.3 , and thus equation B.8 is obtained.

$$\dot{Q}_u = A_r \left\{ S - U_1 \left[ \left( \frac{\dot{Q}_u}{U_o A_r} + T_f \right) - T_a \right] \right\} \quad (\text{B.8})$$

After simplifying, the following expression is obtained,

$$\dot{Q}_u = A_r F' [S - U_1(T_f - T_a)] \quad (\text{B.9})$$

where,  $F'$  is given by

$$F' = \frac{1/U_1}{\frac{1}{U_1} + \frac{D_o}{h_{\text{fi}} D_i} + \frac{D_o \ln(D_o/D_i)}{2k}} \quad (\text{B.10})$$

$F'$  is typically termed the collector efficiency factor (Duffie and Beckman, 2006). It corresponds to the ratio of the thermal resistance between the absorber and ambient air side, as well as the absorber and the working fluid side. The maximum value of the collector efficiency factor is unity, which would occur if the absorber would have the same temperature as  $T_f$ . In practice this is not achievable and, thus, the collector efficiency factor is always less than one.

### B.2.2 Heat Removal Factor

Equation B.9 is further used to develop an expression for the incremental temperature increase of the fluid with the respect to an elementary slice thickness ( $dx$ ), as shown in figure B.2.

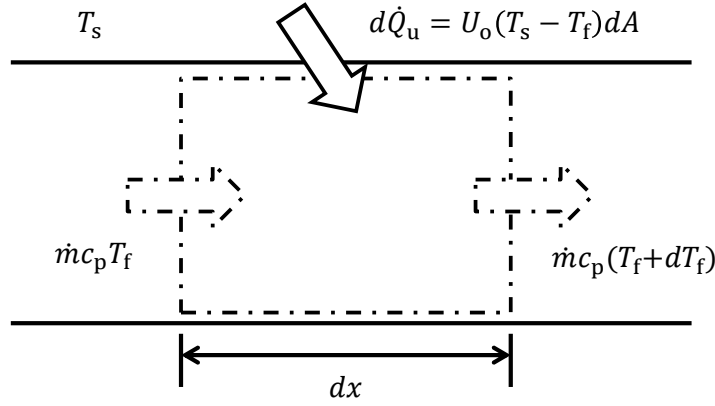


**Figure B.2:** Differential control volume of tube element

By placing a differential control volume around the element, and using the equation for the rate of energy absorbed within the fluid, combined with equation B.9, equation B.11 is obtained.

$$\dot{m}c_p \frac{dT_f}{dx} = F' [S - U_1(T_f - T_a)] \pi D_o \quad (\text{B.11})$$

where,

$c_p$  = specific heat capacity of fluid [kJ/kg K]

$\dot{m}$  = mass flow rate [kg/s]

$dx$  = elementary tube length [m]

Note that the area in equation B.9 can be written as  $A_r = \pi D_o L$  and, thus, in differential terms can be written as  $dA_r = \pi D_o dx$ . Once integrated over the differential thickness ( $x_2 - x_1$ ) equation B.12 is obtained.

$$\int \frac{1}{\left[\left(\frac{S}{U_1} + T_a\right) - T_f\right]} dT_f = \int \frac{F' \pi D_o U_1}{\dot{m}c_p} dx \quad (\text{B.12})$$

after integration, the integral constant is solved, given the boundary condition,

$$T_f(x)|_{x=L} = T_{fo} \quad (\text{B.13})$$

After rearranging,

$$\frac{\left[\left(\frac{S}{U_1} + T_a\right) - T_{fo}\right]}{\left[\left(\frac{S}{U_1} + T_a\right) - T_{fi}\right]} = \exp\left\{-\frac{F'\pi D_o U_1 x}{\dot{m}c_p}\right\} \quad (\text{B.14})$$

Subsequently, a formulation of the fluid outlet temperature is obtained without the requirement of knowing the tube surface temperature, as shown in equation B.15.

$$T_{fo} = -\left[\left(\frac{S}{U_1} + T_a\right) - T_{fi}\right] \exp\left\{-\frac{F'\pi D_o U_1 x}{\dot{m}c_p}\right\} + \frac{S}{U_1} + T_a \quad (\text{B.15})$$

Equation B.14 can also be reformulated by subtracting both sides from unity and thus obtaining,

$$\frac{\left[\left(\frac{S}{U_1} + T_a\right) - T_{fi}\right]}{\left[\left(\frac{S}{U_1} + T_a\right) - T_{fi}\right]} - \frac{\left[\left(\frac{S}{U_1} + T_a\right) - T_{fo}\right]}{\left[\left(\frac{S}{U_1} + T_a\right) - T_{fi}\right]} = 1 - \exp\left\{-\frac{F'\pi D_o U_1 x}{\dot{m}c_p}\right\} \quad (\text{B.16})$$

After simplifying, the change in fluid temperature can be written as,

$$T_{fo} - T_{fi} = \left[\left(\frac{S}{U_1} + T_a\right) - T_{fi}\right] \left[1 - \exp\left\{-\frac{F'\pi D_o U_1 x}{\dot{m}c_p}\right\}\right] \quad (\text{B.17})$$

Using this term to obtain the useful heat gain,

$$\dot{Q}_u = F_R A_r [(S - U_1(T_{fi} - T_a))] \quad (\text{B.18})$$

where  $F_R$  is given by,

$$F_R = \frac{\dot{m}c_p}{U_1 A_r} \left[1 - \exp\left\{-\frac{F' U_1 A_r}{\dot{m}c_p}\right\}\right] \quad (\text{B.19})$$

$F_R$  is commonly known as the heat removal factor (Duffie and Beckman, 2006). This parameter is a critical parameter when selecting a heat transfer fluid. Gasses, for example, have a much lower heat removal factor than fluids.

### B.2.3 External Heat Losses

The external heat losses from a tube element primarily constitute of radiation and convection losses. Conduction losses are neglected at this stage and reflection losses are accounted for within the incident flux on the tube. The external heat losses are given by,

$$\dot{Q}'_{\text{loss}} = h_w \pi D_o (T_s - T_a) + \sigma \epsilon \pi D_o (T_s^4 - T_{\text{sky}}^4) \quad (\text{B.20})$$

where,

$h_w$  = external heat transfer convection coefficient [W/m K]

$\sigma$  = Stefan Boltzmann's constant [W/m<sup>2</sup> K<sup>4</sup>]

$\epsilon$  = emissivity of tube [-]

$T_{\text{sky}}$  = sky temperature [K]

### B.3 Program Structure

Figure B.3 depicts a flow diagram of the internal pipe flow code. The main section of the code is divided into several smaller functions. These include the collector efficiency function, heat removal function, useful heat gain function and the heat loss function. Further functions were developed that calculate the fluid properties according to the correlations from Appendix A. These include the specific heat, thermal conductivity, dynamic viscosity and the fluid density of the working fluid.

Within the main section, a for-loop was written in which the heat transfer calculations were performed. The loop runs  $N$ -number of times, depending on how many tube elements are specified. For this section all tubes are aligned in series with equal amount of incident power. The inlet fluid temperature of the downstream tube element is, thus, equated to the exit fluid temperature of the upstream tube element.

The main program is based on assuming an overall heat loss coefficient, calculating the heat transfer functions, recalculating the overall heat loss coefficient and finally adapting the assumed heat loss coefficient value with the recalculated value, until convergence is reached.

The heat transfer functions include the calculation of  $F'$  from equation B.10,  $F_r$  based on equation B.19 and the useful heat gain calculation, as given by equation B.18. The results obtained were used to determine a value for  $T_{fo}$  from equation D.1.

A value for the external heat losses was then calculated by equation B.1. The result was used to obtain a value for the surface temperature from equation rearranging equation B.2. Once the surface temperature is known, the actual heat losses are determined by equation B.20. This value was then substituted back into equation B.2 to calculate a new overall heat loss coefficient. The initial overall heat loss coefficient was adapted with the calculated overall heat loss coefficient. A while-loop iteratively performed the adaptation until convergence was obtained, given by equation B.21.

$$\left| \frac{U_{l,\delta_{\text{err}}} - U_{l,o}}{U_{l,o}} \right| > 0.1 \quad (\text{B.21})$$

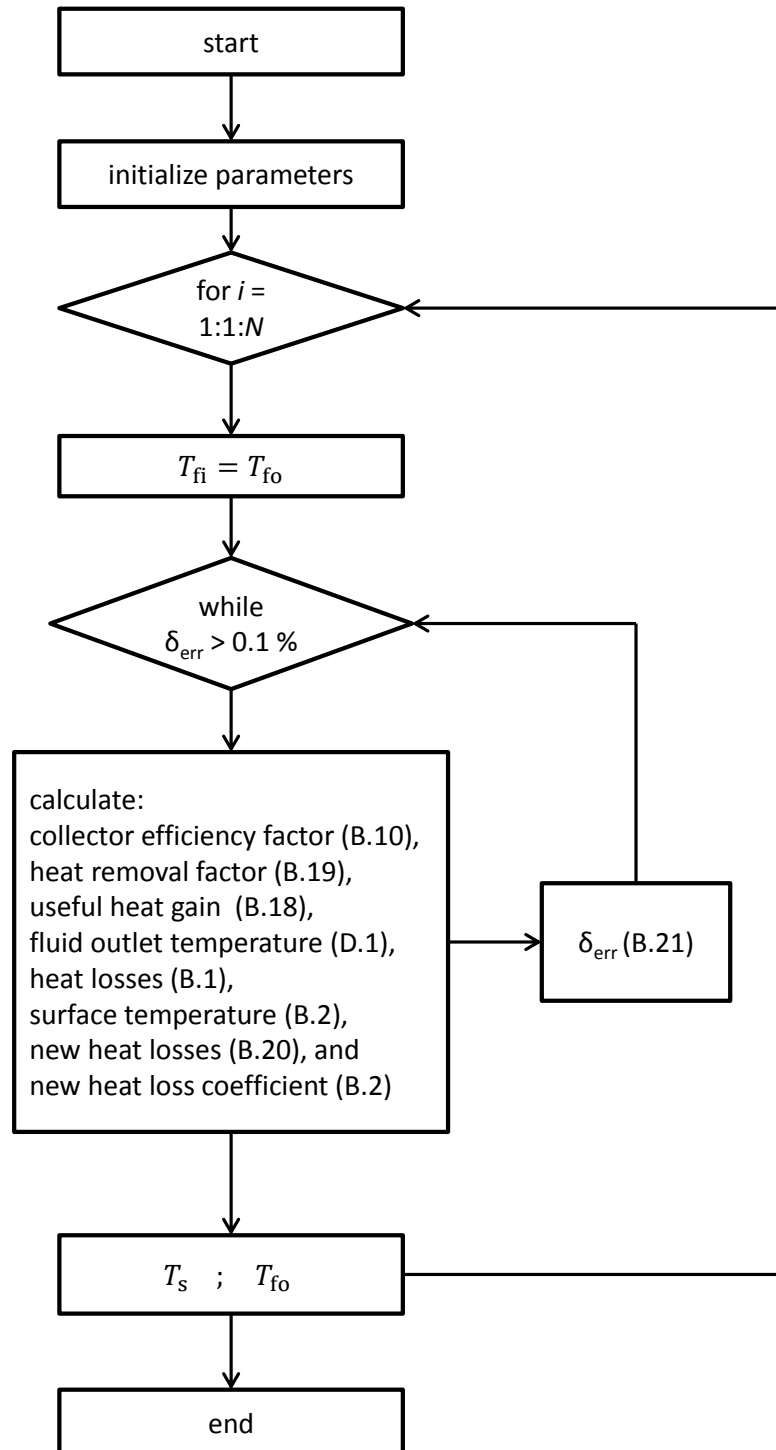


**Figure B.3:** General program structure of thermal analysis, written in MATLAB, where the surface temperature and local fluid temperatures are calculated

## B.4 Program Validation

The program was validated using a commercially available code, called Flownex Simulation Environment (SE). Flownex is a thermal-fluid simulation code typically used for plant modelling.

Flownex, has excellent internal pipe flow modelling capabilities with extensive component libraries such as turbines, pumps, heat exchangers, ect. It solves the partial differential equations for mass, momentum and energy conservation to obtain pressures, mass flow rates and temperatures. The Solver uses the Implicit Pressure Correction Method (IPCM) to solve for the governing equations. IPCM is known to be a robust, fast and unconditionally stable method.

The developed model consisted of a series of solar heated pipes exposed to convection and radiation losses, as depicted in figure B.4.

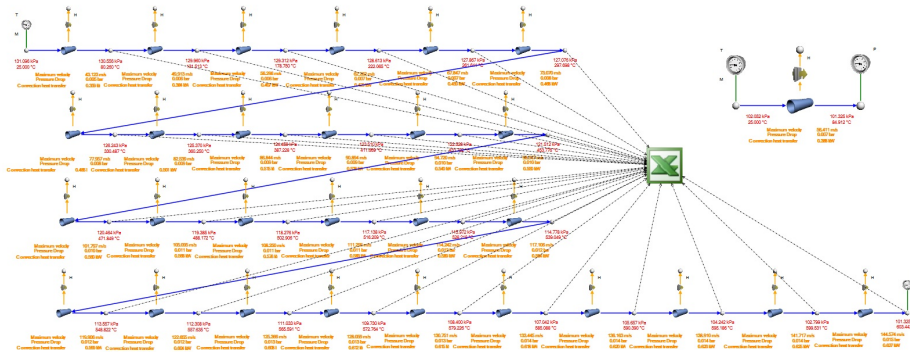


**Figure B.4:** Fluid-flow network model of receiver tubes in Flownex

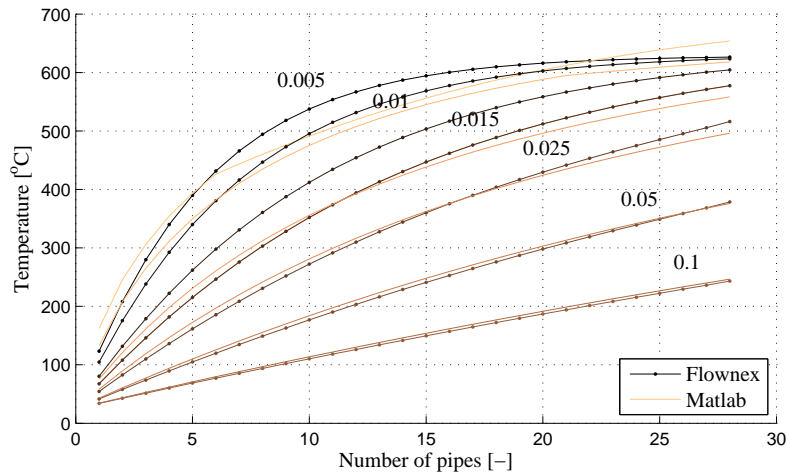
It was decided to use the general heat transfer element in Flownex. Relevant heat transfer modes included convection from the solid node of the pipe to the fluid and convection and radiation from the solid node of the pipe to ambient. The convection heat transfer to the fluid was specified at the upstream node. The heat transfer convection coefficient was to be calculated by equation B.6 and equation B.7. The transition Reynolds number was specified as 2000. For the downstream node convection and radiation are specified. This node represents the outer surface of the pipe element. The solar heat input was also applied on the downstream node of the heat transfer element.

All the pipe elements were specified as copper pipes to minimize the effect of conduction in radial and axial directions. The heat transfer fluid was specified as air with fluid properties as given by the correlations from appendix A. The boundary conditions on the system were set as mass flow and temperature inlet boundaries and pressure outlet boundary of  $P_{\text{atm}} = 101.325 \text{ kPa}$ . Further network specifications are highlighted in table B.1, where C, M and N depict the coefficients for the Dittus Boehler equation from equation B.6.

**Table B.1:** Parametric values used in Flownex pipe network model to validate against Matlab code

Parameter	Value	Unit
$D_o$	0.015	m
$D_i$	0.014	m
$dx$	0.2	m
$\epsilon$	0.9	-
$k_{cu}$	400	$W/m^2.K$
$T_a$	25	$^{\circ}C$
$T_{fi}$	25	$^{\circ}C$
$T_{sky}$	299.06	K
$h_w$	100	$W/m.K$
$C$	0.023	-
$M$	0.8	-
$N$	0.4	-
$N_{lam}$	3.66	-
$F$	1	-

The mass flow rate was adjusted several times for several simulation runs. The fluid temperatures were obtained at the flow nodes downstream the pipe elements and recorded in an excel file, as depicted in figure B.4. The results were compared with results obtained from the Matlab code. The validation results are presented in figure B.5.

**Figure B.5:** Validation of Matlab program with Flownex network for mass flow rates ranging between 0.1 kg/s and 0.005 kg/s

The fluid temperatures are plotted against the number of tube elements in

*APPENDIX B. DEVELOPMENT OF AN INTERNAL PIPE FLOW MODEL  
AND VALIDATION***86**

series for mass flow rates ranging between 0.005 kg/s and 0.1 kg/s. One can see that Matlab code correlates well with the Flownex model, especially for higher mass flow rates. At lower mass flow rates the solver, however, revealed some convergence issues. Nonetheless, by iterating the overall heat loss coefficient a more robust routine was obtained, compared to the iteration of the surface temperatures.



# Appendix C

## Design and Calibration of a Cold Water Flat Plate Calorimeter

### C.1 Introduction

Various tools, such as radiometers, Lambertian plates with charge coupled device (CCD) cameras, or calorimeters are applicable to measure concentrated solar flux. The Gardon sensor is a type of radiometer that measures the radial temperature difference by means of a differential thermocouple to produce a voltage output (Estrada *et al.*, 2007). The Lambertian plate reflects back the concentrated sunlight for a CCD camera to capture the flux levels with high resolution images (Ballestrín *et al.*, 2003). However, most of these devices are in fact calibrated using a calorimeter. Also, the devices are costly and therefore a low cost calorimeter was locally constructed and tested.

This section provides an overview of the design procedure and the calibration experiments as published in Kretzschmar *et al.* (2012).

### C.2 Calorimeter Design

The calorimeter consists of 3 major components (nylon PA6 C cup housing, nylon PA6 C spreader disk and the copper absorber plate), as illustrated in figure C.1. The spreader disk is press-fitted into the cup housing. The copper plate was coated with heat resistant NS-7 paint and screws against the cup housing with M6 cap screws. A high temperature O-ring and gasket sealer are used to prevent the calorimeter from leaking.

The design presented in this project differs from previous work in that only nylon insulation material was used in the main body of the calorimeter (Jaramillo *et al.*, 2008; Mouzouris *et al.*, 2002). Jaramillo *et al.* (2008) reports that of the calorimeter's 13.5 % efficiency loss, 12.6 % is due to internal losses. Here, an AISI 316 stainless steel housing and a stainless steel spreader disk

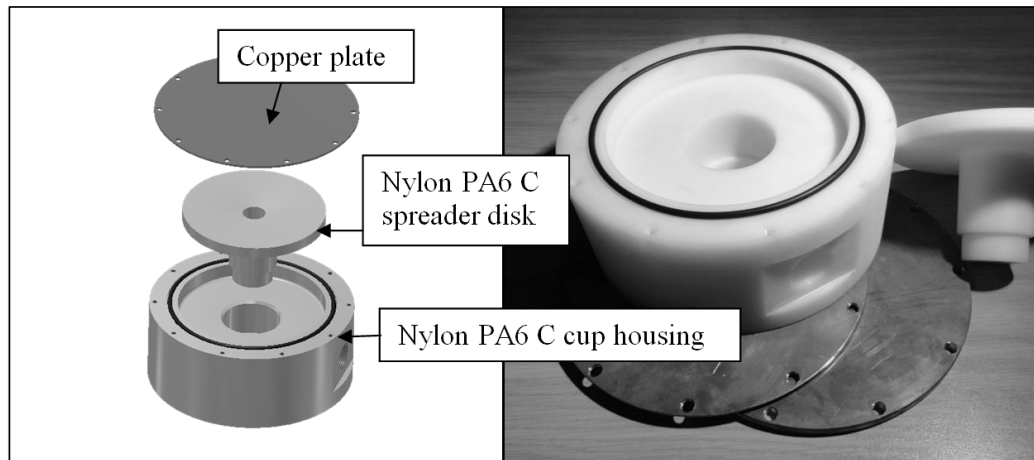


**Figure C.1:** Flat plate calorimeter including the copper plates, the Nylon PA6 C cup housing and spreader disk

were used. Therefore, for the design presented in this paper, only nylon PA6 C material was used. The aim is to improve on the internal losses of the device.

Since the highest incident flux is experienced at the central region of the absorber plate, the calorimeter makes use of a design where the flow stream directly impinges on the hottest point of the plate. Also, the cold water stream is injected first at the high flux region and then spreads out radially along the copper plate. As a result, the highest local surface temperature is reduced not only by means of the coolest fluid temperature but also due to the highest convection heat transfer coefficient.

The design makes provision for the elimination or reduction of fluid flow pre-heating. The local fluid temperature incident on the absorber plate would be higher if the cold inlet flow stream experienced energy exchange from the hot outlet flow stream. Thus, the effective heat transfer to the fluid would be reduced, and the hot fluid stream temperature would drop due to the energy exchange. The wall thickness of the nylon insulation material that separates the flow streams was therefore enhanced.

Future designs might consider improving the heat transfer surface area of the copper plate. For example, a thicker copper plate could be used where radial slots are milled into the material. These slots would act as fins, and the heat transfer to the fluid would be increased. The slots would also improve on the overall convective heat transfer coefficient by generating more turbulence. Furthermore, jet impingement heat transfer could be improved by reducing the size of the inlet diameter. However, the calorimeter would then require a higher inlet pressure and thus be subject to leakages. The tolerable incident flux magnitude would become less, and therefore, the device might not be suitable for measuring fluxes of larger concentrating systems in planning.

## C.3 Calibration

The calibration procedure consisted of developing an internal loss model and empirically comparing the model with experiments.

### C.3.1 Calibration Setup

The performance of the calorimeter was investigated by conducting experiments in a controlled environment using electric power as a heat input, as depicted in figure C.2. The setup consists of a 750 W DC Power supply cou-

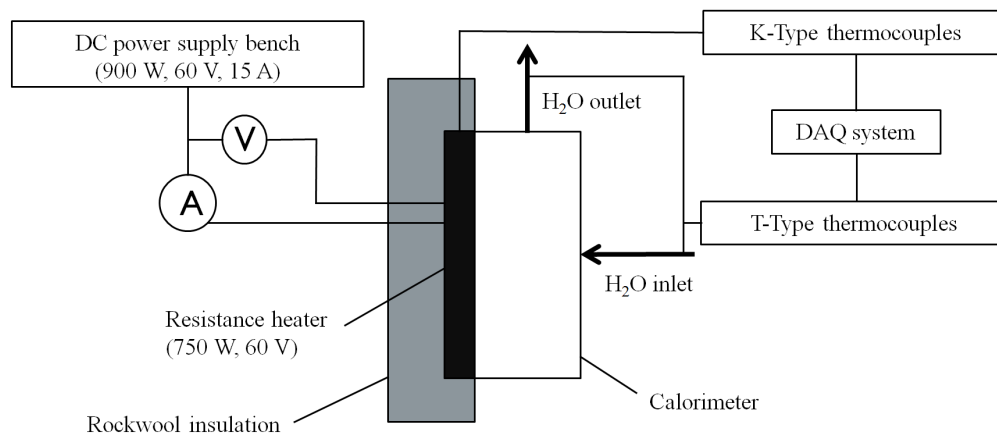


**Figure C.2:** Calibration setup used to characterize the performance of the calorimeter under uniform power input

pled to a flat mica resistance heating element. The rear side of the resistance heater is insulated with rockwool insulation. Volt- and ammeters were used to quantify the applied power, and T-type thermocouples were used to measure the inlet and outlet fluid temperatures. A data acquisition (DAQ) system logged the thermocouple readings with the commercially available Labview software package. A two meter high constant volume tank filled with water at ambient temperatures provided the mass flow through the calorimeter.

The resistance heater was specifically constructed to match with the design profile of the absorber plate with the heater directly screwed against the plate. A metal backing plate was built to squeeze the rockwool insulation against the resistance heater in order to force the energy in the direction of the calorimeter only. It was hoped that the calorimeter would experience the same power magnitude as measured by the volt- and ammeters. Unfortunately, in practice this could not be achieved. The calorimeter including the resistance heater and the rockwool insulation are shown in figure C.3.

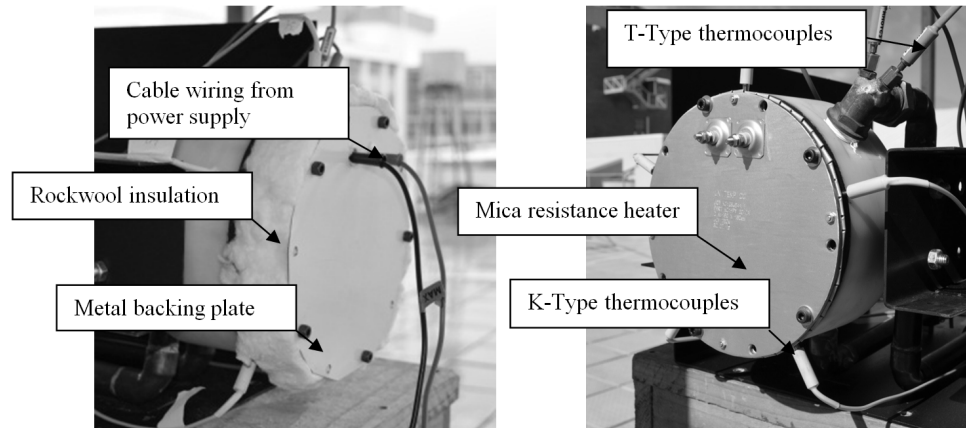


**Figure C.3:** Illustration of the flat mica resistance heater, rockwool insulation and calorimeter during calibration experiment

### C.3.2 Experimental Procedure

The experimental procedure consisted of 3 major steps. Firstly, the voltage level was set to 60 V, and electric power was fed into the system by slowly increasing the current. Secondly, the mass flow rate was adjusted such that a constant change in fluid temperature ( $\Delta T$ ) of 10 °C was obtained. Finally, once the calorimeter reached a steady state at a certain power level, the mass flow rate was measured using the time/volume collection method. Figure C.4 illustrates the system behaviour of the calorimeter under a constant power input of 300 W. The recorded mass flow rate was  $\dot{m} = 0.0061$  kg/s.

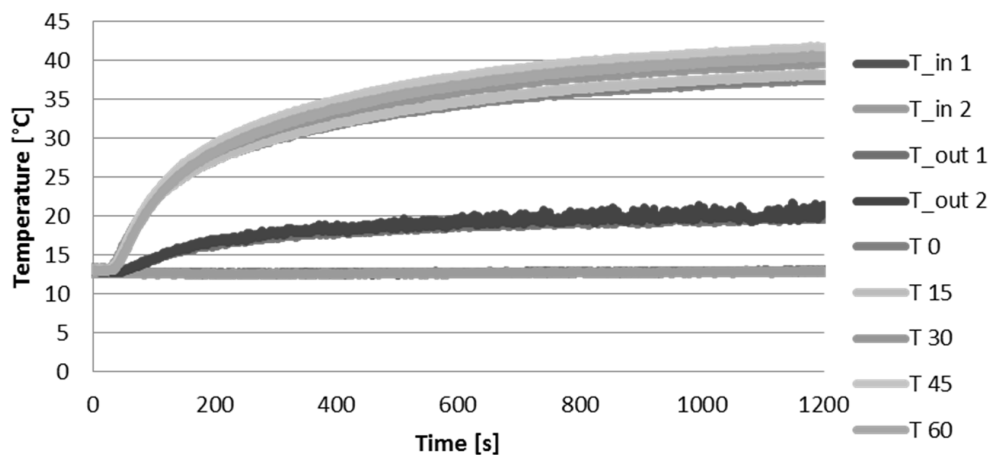


**Figure C.4:** Transient thermal response of the calorimeter to a constant electric power input of 300 W with change in water temperature  $\Delta T \approx 10$  °C and mass flow rate of  $\dot{m} = 0.0061$  kg/s.

### C.3.3 Power Calibration Curves

Figure C.5 illustrates the empirical results obtained for the calibration test at various power inputs. Here, the electrical power input ranges from 300 W to

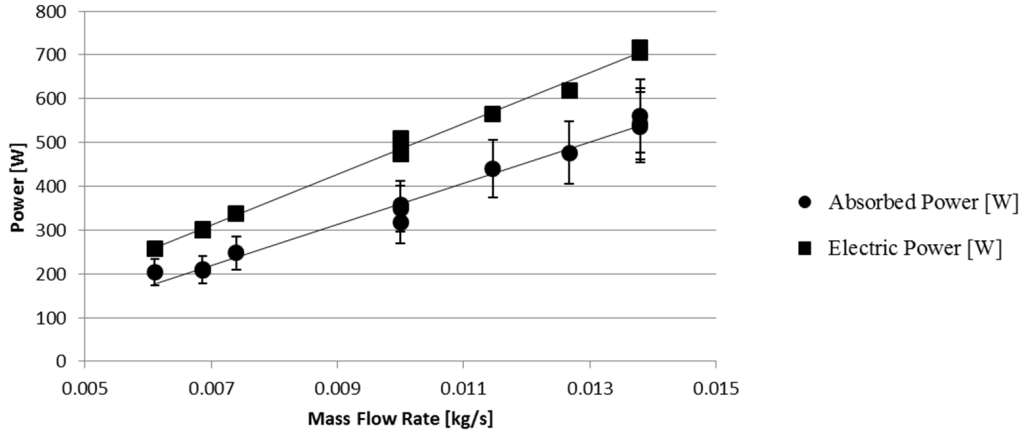


**Figure C.5:** Absorbed power and electric power curves ranging from electric power input of 700 W ( $\dot{m} = 0.0138$  kg/s) to 300 W ( $\dot{m} = 0.00686$  kg/s) at  $\Delta T \approx 10 \pm 0.5$  °C

700 W. For each specific power input the mass flow rate was throttled such that the change in fluid outlet temperature was  $\Delta T \approx 10$  °C. The straight lines are trendlines, which were used to develop correlations, as given below,

$$\dot{Q}_u = \left[ 45800 \left( \frac{\dot{m}}{\text{kg/s}} \right) - 96 \right] \text{ W} \quad (\text{C.1})$$

$$\dot{Q}_i = \left[ 58000 \left( \frac{\dot{m}}{\text{kg/s}} \right) - 98 \right] \text{ W} \quad (\text{C.2})$$

where,  $\dot{Q}_u$  and  $\dot{Q}_i$  depict the absorbed and electrical power, respectively. These correlations are used to determine the magnitude of an electric power in watts that is required to generate a given system response according to the absorbed power value. Assuming that the insulation material worked well, the  $\dot{Q}_i$  can, subsequently, be used as a representative value of the internal energy absorbed by the calorimeter. The work presented in this chapter is used in appendix D.4.

## Appendix D

# Optical Simulation and Validation of the Solar Concentrator

### D.1 Introduction

The work presented in this chapter is used to characterise the medium-scale solar concentrator for use as a flux source during small-scale receiver tests. The main description of the solar concentrator was presented in chapter 5, as well as the description of the modelling setup. This chapter presents the ray-tracing results where the aiming strategy was adjusted to more accurately predict the results obtained during the experiments.

### D.2 Modelling Setup

The model was set up as described in chapter 5. The Matlab-SolTrace coupling tool was used to perform the aimpoint calculations and the optical properties were also set as before. The difference between the ray-tracing analysis from chapter 5 and the one presented in this chapter is that the receiver stage was replaced by a simple flat circular target with a diameter of 150 mm.

### D.3 Modelling Results

The maximum power absorbed by the target for 150 mirrors with  $0.01 \text{ m}^2$  surface area is 1.5 kW at an assumed DNI of  $1000 \text{ W/m}^2$ . This value however is reduced significantly by cosine losses, spillage losses, blocking and shading losses. It is therefore useful to obtain a theoretical value of the remaining flux on the target where these losses are included. The model presented in this section aims to account for these losses, but still needs to be categorised as a theoretical model. This is due to the aimpoints of each heliostat being mathematically calculated, compared to the physical concentrator, where the

*APPENDIX D. OPTICAL SIMULATION AND VALIDATION OF THE SOLAR CONCENTRATOR* **93**

heliostats are calibrated by hand. The idea was to obtain an indication of the maximum power that can be obtained if a perfect concentrator is built and tested.

The optical properties for the mirror and absorber surfaces was obtained from table 5.1. The specifications for the geometry of the concentrator were presented in section 5.2. The simulation was performed with 2 million ray intersections which run for 42.525 s and at a seed value of 5186 for the last ray. The results for the 150 mm diameter round aperture target was as follows:

- Peak Flux : 124 670 W/m<sup>2</sup>
- Average Flux : 54 903.9 W/m<sup>2</sup>
- Absorbed Power: 1189 W

The results reveal that the cosine losses, spillage losses, blocking and shading losses give rise to major reduction in absorbed power of 1189 W, compared to the maximum value of 1500 W. A further reason for the reduction in optical efficiency is the shadow effect of the tower, as can be seen in figure D.1. Also, the central rear mirror facet was used for the beam calibration.

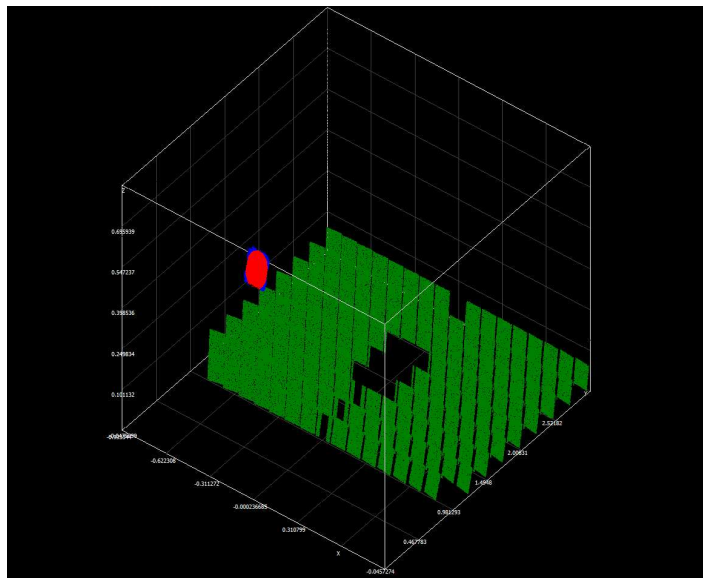


**Figure D.1:** Illustration of the solar concentrator as modelled in SolTrace

Since perfect mirror alignment was applied the spillage losses were expected to be minimal. To investigate the magnitude of these losses and verify the assumption another stage was added to the system. The stage was set in-plane with the aperture target but with slightly larger area to emulate a back wall. The wall was given a 0.3 mm x 0.3 mm rectangular aperture with the

absorber material properties taken as optical properties. The flux values and absorbed power were recorded as follows:

- Peak Flux :  $9332 \text{ W/m}^2$
- Average Flux :  $334 \text{ W/m}^2$
- Absorbed Power:  $8.75 \text{ W}$

The flux maps of the target and the back wall are shown in figures D.2 and D.3. One can clearly see the flux contours approximate the square shape of the mirror facets. Also spillage only occurs at the edges of the flux map.

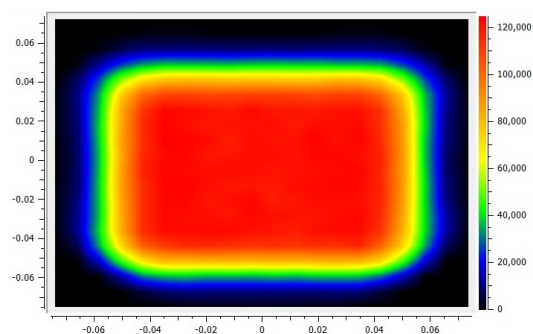


**Figure D.2:** Flux map of target at perfectly aligned mirrors

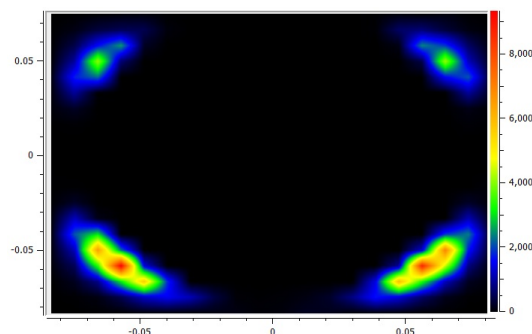


**Figure D.3:** Flux map of back wall at perfectly aligned mirrors

Generally, the results have shown that about 20% of the power is lost due to shading, blocking and cosine losses. For perfectly aligned mirrors the spillage losses constitute about 0.73%. To compare the model with empirical results the model however requires more realistic aimpoint predictions.

### D.3.1 Numerical Results with Adapted Aiming Positions

This section addresses a numerical model in which more realistic aiming positions are applied to the model from section D.3. The objective is to obtain more realistic approximations for the power magnitudes of the spillage losses. The methodology for this approach is to consider the empirically obtained flux image from a testing day (2 July 2013), apply an estimated boundary to the flux image and measure the approximated diameter of the boundary. Then, a Gaussian aimpoint error function is multiplied with the calculated aimpoint vectors, such that the numerical flux map more accurately depicts the empirical flux map.



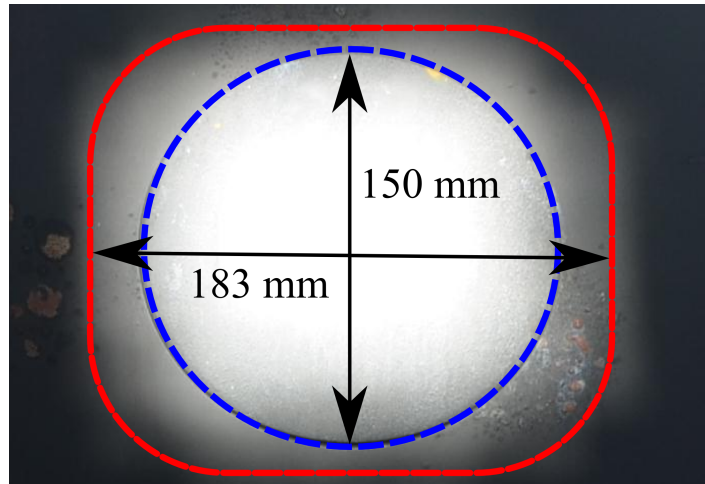


**Figure D.4:** Flux map characterisation from image of target, as seen on 2 July 2013

Figure D.4 illustrates the estimated size of the empirical flux map with an approximate diameter of 183 mm. The overall flux map is approximated as a rectangular shape with round edges.

To model the empirical flux map an error function was introduced in Matlab, based on the Gaussian distribution, with a mean value of 1 and a standard deviation of 0.008. The error value was multiplied with each heliostat's aim-point vector. The ray-tracing results for the target using the same setup as in section D.3 but with the corrected aimpoints is given below:

- Peak Flux : 104 846 W/m<sup>2</sup>
- Average Flux : 44 865 W/m<sup>2</sup>
- Absorbed Power: 1008 W

Similarly, the ray-tracing results for the back wall are recorded as follows:

- Peak Flux : 14 458 W/m<sup>2</sup>
- Average Flux : 1510 W/m<sup>2</sup>
- Absorbed Power: 126.094 W

When comparing the results with section D.3 it can be seen that the absorbed power on the target was reduced by approximately 100 W whereas the power magnitude on the spillage losses significantly increased to 126 W, compared to the previously obtained 8.75 W. This corresponds to spillage losses of about 11 %.

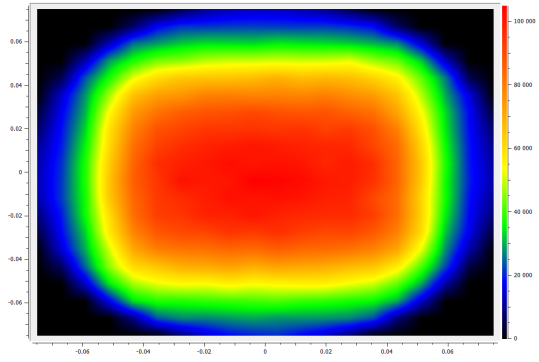


**Figure D.5:** Flux map of target with adapted aimpoint corrections

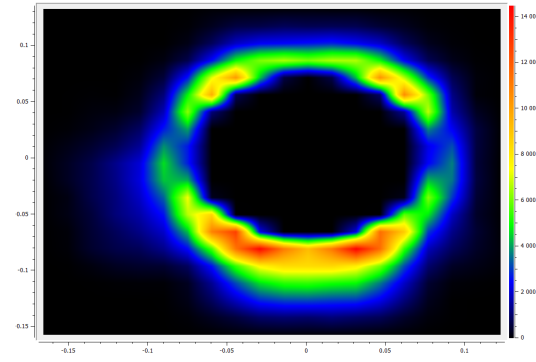


**Figure D.6:** Flux map of the back wall with adapted aimpoint corrections

The flux maps shown in figure D.5 and figure D.6 depict the corrected flux maps of the target and back wall, which reveal closer resemblance of the empirical flux map than the ones obtained in section D.3.

The shapes of these flux maps, however, vary between simulation runs. This is due to the error function generating random standard deviations that distribute the aimpoints arbitrarily.

To obtain a more controlled and repeatable flux map the specular error of the reflected rays was manipulated in SolTrace. The default value of 0.2 mrad was adjusted to 8.5 mrad to obtain a flux map with the approximate diameter of 183 mm. Here, the Gaussian aimpoint error function was neglected. The ray-tracing results for the target are given below:

- Peak Flux : 110 023 W/m<sup>2</sup>
- Average Flux : 45 433.3 W/m<sup>2</sup>
- Absorbed Power: 1021 W

Similarly, the ray-tracing results for the back wall are recorded as follows:

- Peak Flux : 15 045 W/m<sup>2</sup>
- Average Flux : 1359 W/m<sup>2</sup>
- Absorbed Power: 115.175 W

The difference between the results obtained by varying the specular error compared to the results obtained by varying aimpoint error is minimal. This value however changes between simulation runs. In fact, it was found that after performing several simulation runs the difference using the specular error was in a range of 2 W whereas the difference between simulation runs using the aimpoint error varied up to 20 W.

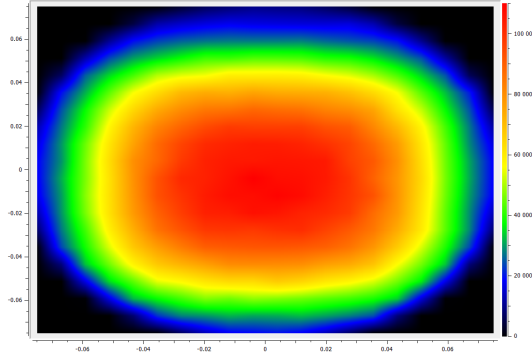


**Figure D.7:** Flux map of target with large specularity error

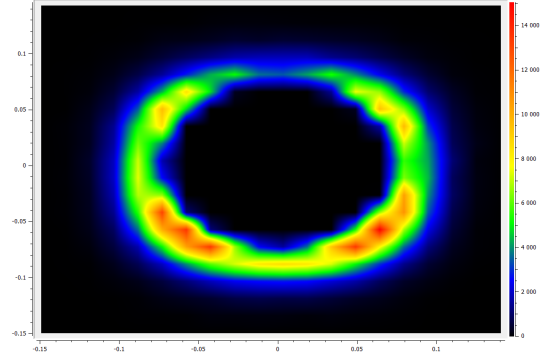


**Figure D.8:** Flux map of the back wall with large specularity error

The flux maps, when using the specularity error method, for the target and back wall are illustrated in figure D.7 and D.8.

When comparing these flux maps with the flux maps in figure D.5 and D.6, one can clearly see that by varying the specularity error a more uniform and controllable flux map generation is obtained. Even though this method does not reflect the physical nature of the problem it provides an adequate approximation thereof. This method was further used during validation.

## D.4 Empirical Validation

From section D.3 it was revealed that peak flux densities of up to  $124 \text{ kW/m}^2$  can be expected at the target. Conventional flux sensors are not applicable for these high fluxes. Also, specialised flux sensors are highly expensive and they were not readily available. As a result, a flat-plate cold water calorimeter was constructed and calibrated. Appendix C provides further details.

The thermocouple readings at the inlet and outlet of the calorimeter were used to obtain the value for the change in temperature,  $(T_{fo} - T_{fi})$ , in equation D.1. Also, by using the time-volume collection method, the mass flow rate was recorded, and, thus, the absorbed energy was obtained.

$$\dot{Q}_u = \dot{m}c_p(T_{fo} - T_{fi}) \quad (\text{D.1})$$

If the absorbed energy was measured at a higher or lower change in temperature than  $10^\circ\text{C}$ , then equation D.2 is used to correct the mass flow rate value.

$$\dot{m}_{\text{norm}} = \left[ \frac{(\dot{Q}_u/W) - (96/W)}{45800} \right] \text{ kg/s} \quad (\text{D.2})$$

The normalized mass flow rate is defined as the mass flow rate that the system would be subject to if, based on a certain absorbed energy value, a change in

fluid temperature of 10 °C would be experienced. Using the corrected mass flow rate the internal energy can be computed from,

$$\dot{Q}_i = \left[ 58000 \left( \frac{\dot{m}_{\text{norm}}}{\text{kg/s}} \right) - 98 \right] \text{W} \quad (\text{D.3})$$

The internal energy value is a summation of the internal losses and absorbed energy, without external losses. Once the internal energy is obtained the external convection and radiation losses are added to this value to provide the total incident energy on the target.

$$\dot{Q}_{\text{tot}} = \dot{Q}_i + \dot{Q}_{\text{rad}} + \dot{Q}_{\text{conv}} \quad (\text{D.4})$$

$\dot{Q}_{\text{tot}}$  can be compared with the energy value from the ray-tracing, denoted as  $\dot{Q}_{\text{tot},n}$  in table D.1. Reflection losses are not considered since the ray-tracing software provides a value with these losses already incorporated. Table D.1 highlights the results obtained from two different testing days, 24 August 2012 and 2 July 2013. The results from 24 August 2012 are obtained from Kretzschmar *et al.* (2012).

**Table D.1:** Validation results of solar concentrator as tested on 2 July 2013 and 24 August 2012

Description	Unit	24 August 2012	2 July 2013
$\phi$	W/m <sup>2</sup>	966	878
$\theta_{\text{elv}}$	[°]	39	21
$\dot{Q}_{\text{tot},n}$	W	1174	895
$\dot{Q}_u$	W	836	641
$\dot{m}$	kg/s	0.0208	0.0142
$\dot{m}_{\text{norm}}$	kg/s	0.0204	0.0161
$\dot{Q}_i$	W	1107.7	834.9
$T_{\text{fo}}$	K	302.6	300.8
$T_{\text{fi}}$	K	293	290
$T_s$	K	348	348
$T_a$	K	292.3	290
$\dot{Q}_{\text{rad}}$	W	6.5	6.7
$\dot{Q}_{\text{conv}}$	W	9.85	10.1
$\dot{Q}_{\text{tot}}$	W	1124	851.7
$\delta_{\text{err}}$	[%]	4.3	4.8

The DNI and the surrounding air temperature was obtained from the Stellenbosch University weather station website on the specific day of testing. The sun angles were obtained from the Solar Position Algorithm (SPA) website (NREL, 2013). The surface temperature was obtained using an infra-red

camera, as shown by the snapshot in figure D.9. The crosshair points at the measured value. The measured value is indicated in the top left corner of the snapshot.

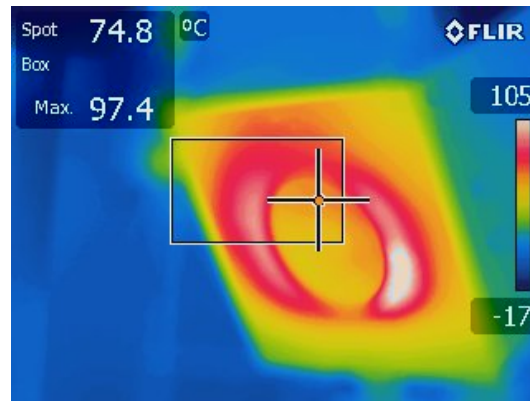


**Figure D.9:** Snapshot image from the infra-red camera

The results show that for 24 August, the incident energy from SolTrace amounted to 1174 W. In comparison, 1124 W has been obtained using the measured value from the calorimeter and adding the analytically calculated convection and radiation losses to this value. The error between the empirical and numerical results for this specific day was therefore 4.3 %. Following the same recipe the flux characterisation for 2 July 2013 was performed and an error of 4.8 % was obtained between numerical and empirical results. Figure D.10 illustrates the sensitivity of absorbed energy variation for three days.

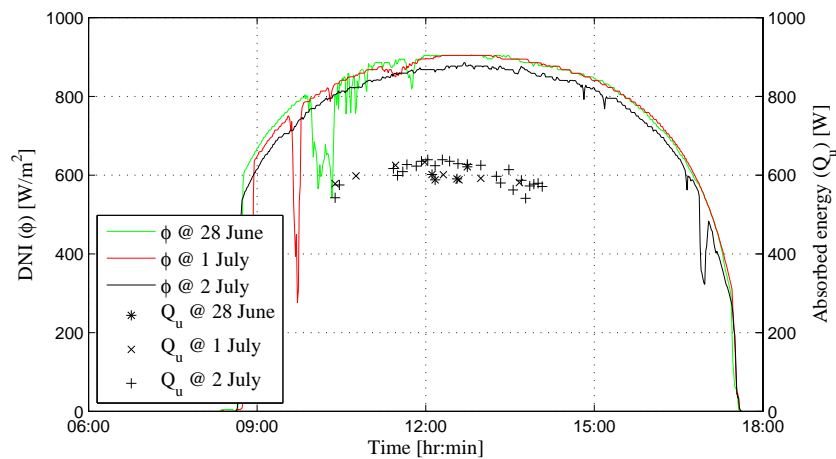


**Figure D.10:** DNI and absorbed energy curves as measured during the experiments on 28 June, 1 July and 2 July 2013

APPENDIX D. OPTICAL SIMULATION AND VALIDATION OF THE SOLAR CONCENTRATOR 100

The energy recordings were conducted between 11:00:00 AM and 14:30:00 PM. One can see that the solar concentrator is highly sensitive to DNI variation as the measured values indicate the same curvature as the DNI measurements.

To investigate whether the solar concentrator provides accurate tracking the energy absorbed values have been normalized with respect to the DNI measurements, denoted as  $\Theta$ . The results are shown in figure D.11.

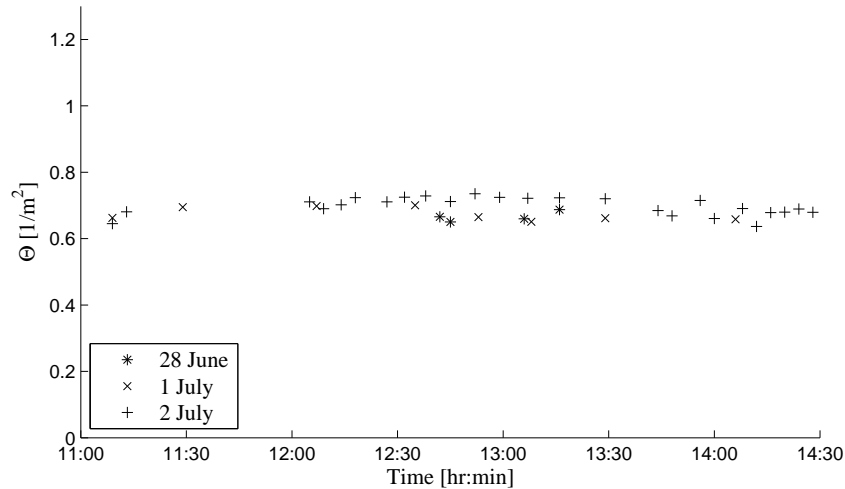


**Figure D.11:** Normalized absorbed power data points obtained from empirical results tested on 28 June, 1 July and 2 July 2013

One can see that the normalized values depict a relatively uniform energy output throughout the testing time. It is therefore shown that the solar tracker provides accurate tracking.

## D.5 Conclusion

A small-scale solar concentrator with 150 suns was modelled and empirically validated. The numerical results were presented in three modes. The first mode included a theoretical case where perfect alignment of the mirrors was assumed. It was revealed that cosine, blocking, and shading losses accumulate to approximately 20%. Spillage losses amount to 0.6%. To obtain a more realistic representation of the spillage losses a Gaussian aimpoint error function was applied to the aimpoint vectors which showed that approximately 11% spillage losses can be expected. Significant variation between simulation runs was observed, though. Subsequently, the specular error of the mirrors was increased to emulate the spillage losses. 10% spillage losses were obtained and less variation between simulation runs was found. Lastly, the numerical results were compared with on-rig experiments using the calorimeter. Errors of 4.3% and 4.8% between numerical and empirical results were obtained.

*APPENDIX D. OPTICAL SIMULATION AND VALIDATION OF THE SOLAR  
CONCENTRATOR* **101**

Further repeatability tests have shown that the solar concentrator provides good tracking accuracy throughout the day.

# Appendix E

## Design of Empirical Validation Setup

### E.1 Introduction

The work presented in this chapter includes a description of the basic requirements of the experimental rig that was used to empirically validate the HPAR concept in chapter 7. The design calculations and the calibration curves of the measuring equipment are also presented.

### E.2 Specification

The basic requirements for the experimental setup was to develop a tower facility onto which a receiver module could be mounted. The receiver model further had to incorporate a way to provide an externally forced flow. Therefore the setup consisted of a ducting system and an in-line suction fan. A variable fan speed controller was used to set the fan speed. Because the fan was limited to air temperatures of 40 °C the test setup further had to incorporate some sort of thermal storage that would cool down the air temperature prior to entering the fan. It was decided to use a small-scale rockbed for this purpose. The rockbed would therefore allow operation for about 20 min until the outlet air temperature of the rockbed would start heating up.

In order to measure the mass flow rate through the ducting system a venturi flow meter was constructed and calibrated. Figure E.1 depicts the main components of the test setup.



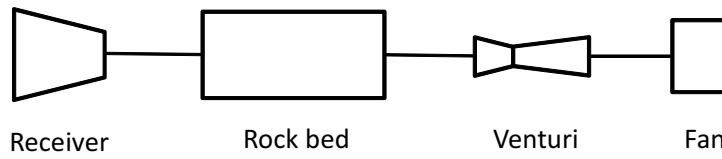


**Figure E.1:** Schematic of components used in test setup to empirically validate the HPAR concept

## E.3 Pressure Drop Calculation

### E.3.1 Duct Impedance

This section presents the design calculations of the system impedance which is used to select a suitable fan model. For these conditions a target velocity flow rate of 6 m/s at the receiver outlet is defined. Also, the geometric dimensions of the duct, rock-bed and pebble sizes are fixed. The impedance is calculated and a fan size is chosen to meet these maximum conditions. A fan control system is further incorporated to throttle down the velocity flow, if smaller velocity magnitudes are desired.

The duct impedance for a target velocity of 6 m/s was calculated in a spread sheet using the velocity method as discussed in Stoecker and Jones (1982).

### E.3.2 Rock Bed Impedance

The pressure drop for the rock-bed itself was obtained by using the Ergun's pressure drop approximation through spherically packed beds (Ergun, 1952). It was decided to use a pebble size of 0.02 m. The rock bed dimensions were chosen as 0.1 m x 0.1m x 0.3 m. The Ergun equation is given by (Ergun, 1952; Allen, 2010),

$$-\frac{\Delta P}{L} = 150 \frac{(1 - \epsilon)^2}{\epsilon^3} \frac{\mu V}{D^2} + 1.75 \frac{(1 - \epsilon)}{\epsilon^3} \frac{\rho V^2}{D} \quad (\text{E.1})$$

where,

$\Delta P$  = pressure drop [Pa]

$\mu$  = fluid dynamic viscosity [kg/m s]

$\epsilon$  = void fraction [ ]

$\rho$  = fluid density [kg/m<sup>3</sup>]

$V$  = flow velocity [m/s]

$D$  = particle diameter [m]

$L$  = length of bed [m]

This equation can be written in terms of the friction factor, as follows.

$$f_{\text{Erg}} = \frac{\Delta P}{L} \frac{D\epsilon^3}{V^2\rho(1-\epsilon)} \quad (\text{E.2})$$

A relation for the friction factor was proposed by Ergun (1952) as given by,

$$f_{\text{Erg}} = 1.75 + \frac{150}{Re_{\text{Erg}}} \quad (\text{E.3})$$

Table E.1 highlights the calculation results for a range of mass flow rates, where one can see the significant increase in pressure drop. The target velocity of 6 m/s corresponds to a mass flow rate of 0.0054 kg/s. As a result, a pressure drop of about 100 Pa can be expected.

**Table E.1:** Pressure drop through rock bed for different Reynolds numbers

$Re_{\text{erg}}$ [-]	$f_{\text{erg}}$ [-]	$\Delta P$ [Pa]	$V$ [m/s]	$\dot{m}$ [kg/s]	$L$ [m]
2098.742	1.821471	336.3474	1.145913	0.009	0.3
1865.548	1.830405	267.0595	1.018589	0.008	0.3
1399.161	1.857207	152.4206	0.763942	0.006	0.3
932.774	1.910811	69.69769	0.509295	0.004	0.3

### E.3.3 Total Impedance

For a target mass flow rate of 0.054 kg/s a pressure drop of 100 Pa is expected through the rockbed, the duct impedance was calculated as 15 Pa, and, therefore, a system impedance of about 115 Pa is expected for the maximum design point.

## E.4 Fan Specification

The fan was specified in such a way that the system impedance, as calculated in section E.3, can be met. Geometric constraints were also considered where fans with duct diameters in excess of 100 mm were rejected. Subsequently, a K100 XL series fan was chosen. The fan curve and power curve are illustrated in figures E.2 and E.3 (Systemair, 2013). The triangle marker depicts the fans working point for maximum efficiency.

## E.5 Venturi Design

The venturi flow meter was designed based on the requirements for venturi flow meters as given by a design catalogue from Preferred-Instruments (2013).

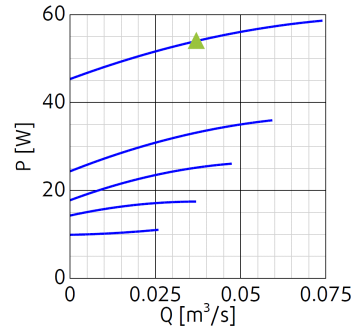
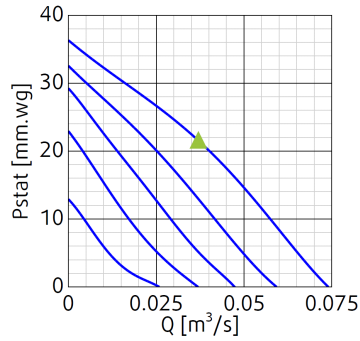


**Figure E.2:** Fan curve K100 XL      **Figure E.3:** Power curve K100 XL

## E.6 Venturi Calibration

The venturi flow meter, as shown in figure 7.1, designed for this setup, was calibrated against an already calibrated venturi flow meter. This was done by adding the calibrated venturi flow meter in series with the duct system and adjusting the mass flow rate. The mass flow rate was varied using the fan speed controller. Figure E.4 illustrates the recorded data points from a differential pressure gauge.

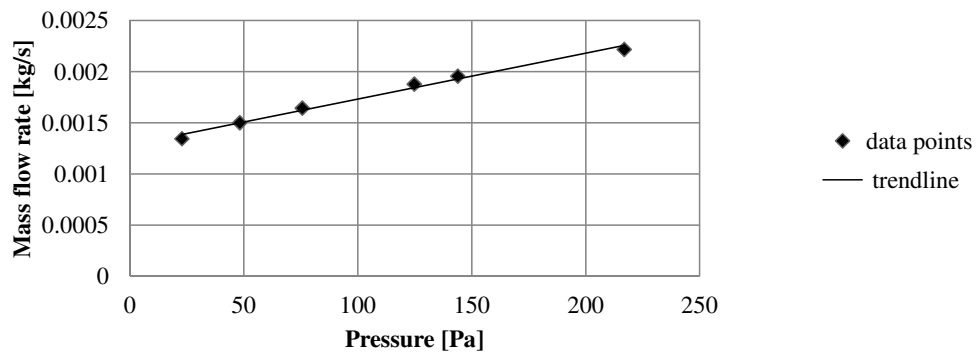


**Figure E.4:** Venturi calibration curve plotted over range of pressure values

A trend line with the following correlation was obtained,

$$\dot{m} = [4 \cdot 10^{-6}(P/\text{Pa}) + 0.0013] \text{ kg/s} \quad (\text{E.4})$$

where  $P$  denotes the pressure measurement in Pa and  $\dot{m}$  the corresponding mass flow rate in kg/s. Once the mass flow rate is known the velocity of the air at different cross-sections in the ducting system can be calculated. For the receiver experiments the airflow was set to a constant velocity of 2.3 m/s.

## E.7 Thermocouple Calibration

All thermocouples were calibrated using a bucket of ice cubes and boiling water. The measurement check was also done to ensure that the probes matched with the probe descriptions in a data acquisition software, called Labview.

# List of References

- Abengoa (2013). Khi Solar One.  
Available at: [http://www.abengoasolar.com/web/en/nuestras\\_plantas/plantas\\_en\\_construccion/sudafrica/#seccion\\_1](http://www.abengoasolar.com/web/en/nuestras_plantas/plantas_en_construccion/sudafrica/#seccion_1)
- Ahlbrink, N., Andersson, J. and Diehl, M. (2010). Optimized operation of an open volumetric air receiver. In: *Proceedings of SolarPACES*, pp. 1–10. Pergignan, France.
- Allen, K. (2010). *Performance characteristics of packed bed thermal energy storage for solar thermal power plants*. Masters (MSc Eng) Thesis, Stellenbosch University.
- Amsbeck, L., Denk, T., Ebert, M., Gertig, C., Heller, P., Herrmann, P., Jedamski, J., John, J., Pitz-paal, R., Prosinečki, T., Rehn, J., Reinalter, W. and Uhlig, R. (2010). Test of a solar-hybrid microturbine system and evaluation of storage deployment. In: *Proceedings of SolarPACES*, 1, pp. 1–8. Pergignan, France.
- Amsbeck, L., Hensch, G., Röger, M. and Uhlig, R. (2009). Development of a Broad-band Antireflection Coated Transparent Silica Window for a Solar-Hybrid Driven Microturbine System. In: *Proceedings of SolarPACES*.
- ANSYS (2012). ANSYS FLUENT 12.0 Theory Guide. , no. October, pp. 1–788.
- Ávila Marín, A.L. (2011 May). Volumetric receivers in Solar Thermal Power Plants with Central Receiver System technology: A review. *Solar Energy*, vol. 85, no. 5, pp. 891–910. ISSN 0038092X.
- Ballestrín, J., Ulmer, S., Morales, A., Barnes, A., Langley, L.W. and Rodriguez, M. (2003 November). Systematic error in the measurement of very high solar irradiance. *Solar Energy Materials and Solar Cells*, vol. 80, no. 3, pp. 375–381. ISSN 09270248.
- Baranov, V.K. (1966). Parabolotoroidal mirrors as elements of solar energy concentrators. *Applied Solar Energy*, vol. 2, pp. 9–12.
- Barbato, M.C. (2013). Si-SiC foams and lattices for high temperature volumetric receivers.
- Becker, M., Fend, T., Hoffschmidt, B., Pitz-Paal, R., Reutter, O., Stamatov, V., Steven, M. and Trimis, D. (2006 October). Theoretical and numerical investigation of flow stability in porous materials applied as volumetric solar receivers. *Solar Energy*, vol. 80, no. 10, pp. 1241–1248. ISSN 0038092X.

- Behar, O., Khellaf, A. and Mohammedi, K. (2013 July). A review of studies on central receiver solar thermal power plants. *Renewable and Sustainable Energy Reviews*, vol. 23, pp. 12–39. ISSN 13640321.
- Berraho, D., Stenzel, T. and Sara, K. (2012). TuNur project : Utility-scale solar energy export from Tunisia' s deserts to Europe. In: *Proceedings of SolarPACES*, pp. 1–10. Marakech, Morocco.
- Boerema, N., Morrison, G., Taylor, R. and Rosengarten, G. (2012 September). Liquid sodium versus Hitec as a heat transfer fluid in solar thermal central receiver systems. *Solar Energy*, vol. 86, no. 9, pp. 2293–2305. ISSN 0038092X.
- Buck, R. (2013). Personal Communication.
- Buck, R., Barth, C., Eck, M. and Steinmann, W. (2006 October). Dual-receiver concept for solar towers. *Solar Energy*, vol. 80, no. 10, pp. 1249–1254. ISSN 0038092X.
- Buck, R., Bräuning, T., Denk, T., Pfänder, M., Schwarzbözl, P. and Tellez, F.M. (2002). Solar-hybrid gas turbine-based power tower systems (REFOS). *Journal of Solar Energy Engineering*, vol. 124, pp. 2–9.
- Burgaleta, J.I., Ternero, A., Vindel, D., Salbidegoitia, I. and Azcarraga, G. (2012). Gemasolar, key points for the operation of the plant. In: *Proceedings of SolarPACES*, pp. 1–11. Marakech, Morocco.
- Cengel, Y.A. (2006). *Heat and Mass Transfer: A Practical Approach*. 3rd edn. Mc Graw-Hill, Singapore.
- Cengel, Y.A. and Boles, M.A. (2007). *Thermodynamics: An engineering approach*. 6th edn. Mc Graw-Hill, New York, USA. ISBN 978-007-125771-8.
- Chen, Y.T. and Buck, R. (2004). Comparison of Two Sun Tracking Heliostat Field. vol. 126, no. 17, pp. 638–644.
- Craig, K., Gauché, P. and Kretzschmar, H. (2013). Optimization of solar tower hybrid pressurized air receiver using CFD. In: *Proceedings of SolarPACES*, pp. 1–10. Las Vegas, USA.
- Daguenet-Frick, X., Toutant, A., Bataille, F. and Olalde, G. (2013 April). Numerical investigation of a ceramic high-temperature pressurized-air solar receiver. *Solar Energy*, vol. 90, pp. 164–178. ISSN 0038092X.
- Duffie, J.A. and Beckman, W.A. (2006). *Solar Engineering of Thermal Processes*, vol. 53. Wiley. ISBN 0471698679.  
Available at: <http://link.aip.org/link/?AJP/53/382/1&Agg=doi>
- Ergun, S. (1952). Fluid flow through packed columns. *Chemical Engineering Progress*, vol. 48.2, pp. 89–94.

- Estrada, C., Jaramillo, O., Acosta, R. and Arancibia-Bulnes, C. (2007 October). Heat transfer analysis in a calorimeter for concentrated solar radiation measurements. *Solar Energy*, vol. 81, no. 10, pp. 1306–1313. ISSN 0038092X.
- Faghri, M. and Welty, J. (1978). Analysis of heat transfer, including axial fluid conduction, for laminar tube flow with arbitrary circumferential wall heat flux variation. *International Journal of Heat and Mass Transfer*, vol. 21, pp. 317–323.
- Fang, J., Wei, J., Dong, X. and Wang, Y. (2011 January). Thermal performance simulation of a solar cavity receiver under windy conditions. *Solar Energy*, vol. 85, no. 1, pp. 126–138. ISSN 0038092X.
- Fend, T., Hoffschmidt, B., Pitz-Paal, R., Reutter, O. and Rietbrock, P. (2004 April). Porous materials as open volumetric solar receivers: Experimental determination of thermophysical and heat transfer properties. *Energy*, vol. 29, no. 5-6, pp. 823–833. ISSN 03605442.
- Fend, T., Pitz-paal, R. and Reutter, O. (2004b). Two novel high-porosity materials as volumetric receivers for concentrated solar radiation. *Solar Energy Materials*, vol. 84, pp. 291–304.
- Garbrecht, O., Al-sibai, F., Kneer, R. and Wieghardt, K. (2012). Numerical Investigation of a New Molten Salt Central Receiver Design. In: *Proceedings of SolarPACES*, pp. 1–10. Marakech, Marocco.
- Gartner, D., Johannsen, K. and Ramm, H. (1974). Turbulent heat transfer in a circular tube with circumferentially varying thermal boundary conditions. *International Journal of Heat and Mass Transfer*, vol. 17, pp. 1003–1018.
- Gazzo, A., Kost, C.P., Ragwitz, M., Govindarajalu, C., Roos, P. and Hassan, F. (2010). Review of CSP Technologies. In: *MENA Assessment of the local manufacturing potential for Concentrated Solar Power projects*, pp. 9–68. World Bank.  
Available at: [http://arabworld.worldbank.org/content/awi/en/home/research/mena\\_solar.html](http://arabworld.worldbank.org/content/awi/en/home/research/mena_solar.html)
- Grange, B., Ferrière, A., Siros, F. and Fan, Y. (2011). Modelling and design of a pressurized air solar receiver for the PEGASE project. In: *Proceedings of SolarPACES*, pp. 1–8. Grenada, Spain.
- Grasse, W. (1991). PHOEBUS: international 30 MWe solar tower plant. *Solar Energy Materials*, vol. 24, no. 1-4, pp. 82–94. ISSN 01651633.
- Grasse, W., Hertlein, H. and Winter, C. (1991). Thermal solar power plants experience. In: *Solar Power Plants*, pp. 251–282. Springer, Berlin.
- Haeberle, A., Zahler, C., Lerchenmueller, H., Mertins, M., Wittwer, C., Trieb, F. and Dersch, J. (2002). The Solarmundo line focussing Fresnel collector. Optical and thermal performance and cost calculations. In: *Proceedings of SolarPACES*, pp. 1–11. Zurich, Switzerland.

- Harris, J. and Lenz, T. (1985). Thermal performance of solar concentrator/cavity receiver systems. *Solar Energy*, vol. 34, no. 2, pp. 135–142.
- Heller, L. and Gauché, P. (2013). Dual-pressure air receiver cycle for direct storage charging. In: *Proceedings of SolarPACES*, vol. 00, pp. 1–10. Las Vegas, USA.
- Heller, P. (2011). Solar-Hybrid Power and Cogeneration Plants (SOLHYCO): Public report. Tech. Rep. 019830, Deutsche Luft- und Raumfahrt e.V, Cologne, Germany.
- Heller, P., Pfänder, M., Denk, T., Tellez, F., Valverde, A., Fernandez, J. and Ring, A. (2006 October). Test and evaluation of a solar powered gas turbine system. *Solar Energy*, vol. 80, no. 10, pp. 1225–1230. ISSN 0038092X.
- Hischier, I. (2011). *Development of a pressurized receiver for solar-driven gas turbines*. Ph.D. thesis, ETH Zurich.  
Available at: <http://e-collection.library.ethz.ch/view/eth:5243>
- Ho, C.K. (2008). Implementing the Discrete Ordinate (DO) radiation model for UV-dose simulations. Tech. Rep., Sandia National Laboratory, Albuquerque, New Mexico.
- Hoffschmidt, B., Tellez, F.M., Valverde, A., Fernandez, J. and Fernandez, V. (2003). Performance evaluation of the 200-kWth HiTRec-II open volumetric air receiver. *Journal of Solar Energy Engineering*, vol. 125, no. 1, p. 87. ISSN 01996231.
- Howell, J.R., Siegel, R. and Menguc, M.P. (2011). *Thermal Radiation Heat Transfer*. 5th edn. Taylor and Francis Group, LLC, Boca Raton. ISBN 978-1-4398-0533-6.
- Hunt, A. and Miller, F. (2010). Small Particle Heat Exchange Receivers for Solar Thermal Power. In: *Proceedings of SolarPACES*, pp. 1–9. Pergignan, France.
- IRENA (2012). Concentrating solar power.  
Available at: [http://www.trec-uk.org.uk/resources/ingenia\\_18\\_Feb\\_March\\_2004.pdf](http://www.trec-uk.org.uk/resources/ingenia_18_Feb_March_2004.pdf)
- Jaramillo, O., Pérez-Rábago, C., Arancibia-Bulnes, C. and Estrada, C. (2008 October). A flat-plate calorimeter for concentrated solar flux evaluation. *Renewable Energy*, vol. 33, no. 10, pp. 2322–2328. ISSN 09601481.
- Jilte, R.D., Kedare, S.B. and Nayak, J.K. (2013 January). Natural Convection and Radiation Heat Loss from Open Cavities of Different Shapes and Sizes Used with Dish Concentrator. *Mechanical Engineering Research*, vol. 3, no. 1, pp. 25–43. ISSN 1927-0615.
- Karni, J., Kribus, A., Rubin, R. and Doron, P. (1998). The Porcupine : A Novel High-Flux Absorber For Volumetric Solar Receivers. *Energy Engineering*, vol. 120.
- Kitamura, R., Pilon, L. and Jonasz, M. (2007). Optical constants of silica glass from extreme ultraviolet to far infrared at near room temperature. vol. 46, no. 33.



- Kolb, G., Ho, C.K., Mancini, T.R. and Gary, J.A. (2011). Power tower technology roadmap and cost reduction plan. Tech. Rep. April, Sandia National Laboratories, Albuquerque, New Mexico.
- Koll, G., Sahraoui, T., Hoffschmidt, B., Khedim, A., Pomp, S., Schwarzbözl, P. and Dillig, M. (2011). ALSOL: Solar Thermal Tower Power Plant Algeria. In: *SolarPaces conference proceedings*, pp. 1–8.
- Koll, G., Schwarzbözl, P., Hennecke, K., Hartz, T., Schmitz, M. and Hoffschmidt, B. (2009). The solar tower Jülich- A research and demonstration plant for central receiver systems. In: *Proceedings of SolarPACES*, pp. 1–8. Berlin, Germany.
- Kretzschmar, H. and Gauché, P. (2012). Hybrid pressurized air receiver for the SUNSPOT cycle. In: *Proceedings of SASEC*, pp. 1–9. Stellenbosch, South Africa.
- Kretzschmar, H., Mouzouris, M. and Gauché, P. (2012). Development of a flat-plate calorimeter for a small-scale heliostat field. In: *Proceedings of SolarPACES*, pp. 1–10. Marakech, Morocco.
- Kribus, A. (1999). Future directions in solar thermal electricity generation. In: *Solar Thermal Electricity Generation*, pp. 251–285. CIEMAT, Madrid, Spain.
- Kribus, A., Doron, P. and Rubin, R. (2001). Performance of the Directly-Irradiated Annular Pressurized Receiver (DIAPR) operating at 20 bar and 1,200 C. *Journal of Solar Energy Engineering*, vol. 123, pp. 10–17.
- Kribus, A., Ries, H. and Spirkel, W. (1996). Inherent Limitations of Volumetric Solar Receivers. *Journal of Solar Energy Engineering*, vol. 118, pp. 151–155.
- Kröger, D.G. (2004). *Air-cooled heat exchangers and cooling towers: Thermal-flow performance evaluation and design, Vol 2*. PenWell Corp., Stellenbosch, South Africa. ISBN 978-1-59370-019-5.
- Kröger, D.G. (2012). The Stellenbosch University solar power thermodynamic cycle. Tech. Rep., University Stellenbosch, Stellenbosch, South Africa.  
Available at: [http://blogs.sun.ac.za/sterg/files/2012/10/SUNSPOT\\_July\\_2012.pdf](http://blogs.sun.ac.za/sterg/files/2012/10/SUNSPOT_July_2012.pdf)
- Kumar, P. and Eswaran, V. (2010). A Numerical Simulation of Combined Radiation and Natural Convection in a Differential Heated Cubic Cavity. *Journal of Heat Transfer*, vol. 132, no. 2, p. 023501. ISSN 00221481.  
Available at: <http://heattransfer.asmedigitalcollection.asme.org/article.aspx?articleid=1449835>
- Li, X., Kong, W., Wang, Z., Chang, C. and Bai, F. (2010 May). Thermal model and thermodynamic performance of molten salt cavity receiver. *Renewable Energy*, vol. 35, no. 5, pp. 981–988. ISSN 09601481.
- Li, Z. (2007). *Characteristics of buoyancy driven natural ventilation through horizontal openings*. PhD thesis, Aalborg University.

- Lipinski, W., Modest, M. and Steinfeld, A. (2009). Heat transfer analysis of a novel pressurized air receiver for concentrated solar power via combined cycles. *Journal of Thermal Science and Engineering Applications*, vol. 1, no. 4, pp. 041002/1–6.
- Maag, G., Falter, C. and Steinfeld, A. (2011). Temperature of a quartz/sapphire window in a solar cavity receiver. *Journal of Solar Energy Engineering*, vol. 133, no. 1, p. 014501. ISSN 01996231.
- Meduri, P., Hannemann, C. and Pacheco, J. (2010). Performance characterization and operation of eSolar's Sierra SunTower power tower plant. In: *Proceedings of SolarPACES*, pp. 1–8. Pergignan, France.
- Meinecke, W. and Cordes, S. (1994). Phoebus technology program solar air receiver (TSA)- operational experience and test evaluation of the 2.5 MWth volumetric air receiver test facility at the Plataforma Solar de Almeria. In: *Proceeding of the 7th International Symposium on Solar Thermal Concentrating Technologies*, pp. 943–957. Moscow, Russia.
- Montes, M., Rovira, A., Martinez-Val, J. and Ramos, A. (2011 October). Proposal of a fluid flow layout to improve the heat transfer in the active absorber surface of solar central cavity receivers. *Applied Thermal Engineering*, vol. 35, pp. 220–232. ISSN 13594311.
- Moufekkik, F., Moussaoui, M., Mezrhab, a., Bouzidi, M. and Laraqi, N. (2013 January). Study of double-diffusive natural convection and radiation in an inclined cavity using lattice Boltzmann method. *International Journal of Thermal Sciences*, vol. 63, pp. 65–86. ISSN 12900729.  
Available at: <http://linkinghub.elsevier.com/retrieve/pii/S1290072912002153>
- Mouzouris, M., Kretschmar, H. and Brooks, M.J. (2012). Design challenges in point-focus solar collectors: Optical error analysis and thermal performance validation. In: *Proceedings of SolarPACES*, Figure 1, pp. 1–8. Marakech, Morocco.
- Mouzouris, M., Roberts, L.W. and Brooks, M.J. (2002). Heat transfer analysis for high-flux solar measurements using a flat plate calorimeter. *R & D Journal of the South African Institution of Mechanical Engineering*, vol. 27, pp. 10–22.
- Naphon, P. (2011 January). Study on the heat transfer and flow characteristics in a spiral-coil tube. *International Communications in Heat and Mass Transfer*, vol. 38, no. 1, pp. 69–74. ISSN 07351933.
- Nouanegue, H., Muftuoglu, a. and Bilgen, E. (2008 December). Conjugate heat transfer by natural convection, conduction and radiation in open cavities. *International Journal of Heat and Mass Transfer*, vol. 51, no. 25-26, pp. 6054–6062. ISSN 00179310.  
Available at: <http://linkinghub.elsevier.com/retrieve/pii/S0017931008003086>

- NREL (2013). NREL's Solar Position Algorithm (SPA).  
Available at: <http://www.nrel.gov/midc/spa/>
- Nutec (2009). Nutec Ceiling Boards.  
Available at: [www.everite.co.za](http://www.everite.co.za)
- Okić, M., Roušar, I., Táborský, Z. and Roháček, K. (1987). Reflectivity and surface composition of electrochemically and mechanically polished stainless steel. *Materials chemistry and physics*, vol. 17, pp. 301–309.
- Omega (2013). Table of Total Emissivity.  
Available at: [www.omega.com](http://www.omega.com)
- Pacheco, J.E., Bradshaw, R.W., Dawson, D.B., De la Rosa, W., Gilbert, R., Goods, S.H., Hale, M.J., Jacobs, P., Jones, S.A., Kolb, G.J., Prairie, M.R., Reily, H.E., Showalter, S.K. and Vant-Hull, L.L. (2002). Final Test and Evaluation Results from the Solar Two Project. Tech. Rep. January, Sandia National Laboratories, Albuquerque, New Mexico.  
Available at: <http://prod.sandia.gov/techlib/access-control.cgi/2002/020120.pdf>
- Pacheco, J.E., Reilly, H.E., Kolb, G.J. and Tyner, C.E. (2000). Summary of the Solar Two test and evaluation program. In: *Proceeding of the Renewable Energy for the New Millennium*, pp. 1–11. Sydney, Australia.
- Paitoonsurikarn, S. and Lovegrove, K. (2003). On the study of convection loss from open cavity receivers in solar paraboloidal dish applications. In: *Proceedings of ANZSES*, vol. 0, pp. 154–161. Queensland, Australia.
- Pitz-Paal, R., Morhenne, J. and Fiebig, M. (1991). A new concept of a selective solar receiver for high temperature applications. *Solar Energy Materials*, vol. 24, pp. 293–306.
- Pompea, S. and Breault, R. (1995). Black surfaces for optical systems. In: Bass, M. (ed.), *Handbook of Optics*, chap. 37, p. 37.15. Mc Graw-Hill, Florida, USA. ISBN 0-07-047974-7.
- Prakash, M., Kedare, S. and Nayak, J. (2010 April). Determination of stagnation and convective zones in a solar cavity receiver. *International Journal of Thermal Sciences*, vol. 49, no. 4, pp. 680–691. ISSN 12900729.
- Preferred-Instruments (2013). Flow meter piping requirements.  
Available at: <http://www.preferredinstruments.com/documents/flowmeterpipingrequirements.pdf>
- Price, H., Luepfert, E., Kearney, D., Zarza, E., Cohen, G., Gee, R. and Mahoney, R. (2002). Advances in Parabolic Trough Solar Power Technology. *Journal of Solar Energy Engineering*, vol. 124, no. 2, p. 109. ISSN 01996231.

- Radosevich, L.G. and Skinrood, A.C. (1989). The power production operation of Solar One, the 10 MWe solar thermal central receiver pilot plant. *Journal of Solar Energy Engineering*, vol. 111, no. 2, pp. 144–151.
- Reda, I. and Andreas, A. (2003). Solar Position Algorithm for Solar Radiation Applications. Tech. Rep. January, National Renewable Energy Laboratory, Colorado, USA.
- Reynolds, W. (1963 June). Turbulent heat transfer in a circular tube with variable circumferential heat flux. *International Journal of Heat and Mass Transfer*, vol. 6, no. 6, pp. 445–454. ISSN 00179310.
- Romero, M., Buck, R. and Pacheco, J.E. (2002). An Update on Solar Central Receiver Systems, Projects, and Technologies. *Journal of Solar Energy Engineering*, vol. 124, no. 2, pp. 98–108. ISSN 01996231.
- Romero, M. and Steinfeld, A. (2012). Concentrating solar thermal power and thermochemical fuels. *Energy & Environmental Science*, vol. 5, no. 11, p. 9234. ISSN 1754-5692.  
Available at: <http://xlink.rsc.org/?DOI=c2ee21275g>
- Romero-Alvarez, M. and Zarza, E. (2007 May). Concentrating Solar Thermal Power. In: Kreith, F. and Yogi Goswami, D. (eds.), *Handbook of Energy Efficiency and Renewable Energy*, vol. 20070849 of *Mechanical Engineering Series*, chap. 21, pp. 21.1–21.97. CRC Press, Boca Raton, Florida. ISBN 978-0-8493-1730-9.  
Available at: <http://www.crcnetbase.com/doi/book/10.1201/9781420003482>
- Ruther, S. and Miller, F. (2010). Monte Carlo Radiation Simulation of a Cylindrical Small Particle Solar Receiver. In: *Proceedings of SolarPACES*, pp. 1–8. Pergignan, France.
- Schmitz, M., Schwarzbozl, P., Buck, R. and Pitzpaal, R. (2006 January). Assessment of the potential improvement due to multiple apertures in central receiver systems with secondary concentrators. *Solar Energy*, vol. 80, no. 1, pp. 111–120. ISSN 0038092X.
- Segal, A. and Epstein, M. (2003 December). Optimized working temperatures of a solar central receiver. *Solar Energy*, vol. 75, no. 6, pp. 503–510. ISSN 0038092X.
- Shub, L. (1993 March). Calculation of turbulent flow and heat transfer in a tube with a periodically varying cross-section. *International Journal of Heat and Mass Transfer*, vol. 36, no. 4, pp. 1085–1095. ISSN 00179310.
- Slack, M., Meduri, P. and Sonn, A. (2010). eSolar power tower performance modeling and experimental validation. In: *Proceedings of SolarPACES*, pp. 1–8. Pergignan, France. ISBN 1626685185.
- SOLGATE (2005). Solar hybrid gas turbine electric power system (SOLGATE). Tech. Rep..  
Available at: [http://ec.europa.eu/research/energy/pdf/solgate\\_en.pdf](http://ec.europa.eu/research/energy/pdf/solgate_en.pdf)

- Soo Too, Y.C. and Benito, R. (2013 January). Enhancing heat transfer in air tubular absorbers for concentrated solar thermal applications. *Applied Thermal Engineering*, vol. 50, no. 1, pp. 1076–1083. ISSN 13594311.
- Sparrow, E.M. and Cess, R.D. (1978). *Radiation heat transfer*. Augmented edn. Washington : Hemisphere Pub. Corp., c1978. ISBN 0070599106.
- Stein, W., Kim, J.-S., Burton, A., Menaughton, R., Soo Too, Y.C., McGregor, J., Nakatani, H., Tagawa, M., Osada, T., Okubo, T. and Kobayashi, K. (2010). Design and construction of a 200kWe tower brayton cycle pilot plant. In: *Proceedings of SolarPACES*. Pergignan, France.
- Stine, W.B. and Geyer, M. (2001). Central Receiver Systems. In: *Power from the sun*. Available at: <http://www.powerfromthesun.net>
- Stoecker, W.F. and Jones, J.W. (1982). *Refridgeration and air conditioning*. 2nd edn. Mc Graw-Hill, Austin, USA. ISBN 0-07-066591-5.
- Suter, C. (2012). *Thermoelectric conversion of concentrated solar radiation and geothermal energy*. Dissertation, ETH Zurich, Zurich, Switzerland.
- Systemair (2013). K 100 XL circular duct fan. Available at: <http://www.systemair.com/K-100-XL-Circular-duct-fan-en-1004.aspx>
- Tahboub, Z.M., Dahleh, B. and Goebel, O. (2012). Solar mirrors soiling campaign - Abu Dhabi. In: *Proceedings of SolarPACES*, pp. 1–9. Marakech, Marocco.
- Tan, T. and Chen, Y. (2010 January). Review of study on solid particle solar receivers. *Renewable and Sustainable Energy Reviews*, vol. 14, no. 1, pp. 265–276. ISSN 13640321.
- Taumoefolau, T. and Lovegrove, K. (2002). An experimental study of natural convection heat loss from a solar concentrator cavity receiver at varying orientation. In: *Proceedings of SolarPACES*, pp. 1–6. Zurich, Switzerland.
- Teichel, S.H., Feierabend, L., Klein, S.a. and Reindl, D.T. (2012 June). An alternative method for calculation of semi-gray radiation heat transfer in solar central cavity receivers. *Solar Energy*, vol. 86, no. 6, pp. 1899–1909. ISSN 0038092X.
- Tian, Y. and Zhao, C. (2013 April). A review of solar collectors and thermal energy storage in solar thermal applications. *Applied Energy*, vol. 104, pp. 538–553. ISSN 03062619.
- Tydex (2013). Quartz Glass for Optics. Available at: [www.tydex.ru](http://www.tydex.ru)
- Uhlig, R. (2009). Transient Stresses at Metallic Solar Tube Receivers. In: *Proceedings of SolarPACES*, pp. 1–8. Berlin, Germany.

- Versteeg, H. and Malalasekera, W. (2007). Calculation of radiative heat transfer. In: *An introduction to computational fluid dynamics: The finite volume method*, 2nd edn, chap. 13, p. 420. Pearson Prentice Hall, Harlow, England. ISBN 978-0-13-127498-3.
- Villafán-Vidales, H., Abanades, S., Caliot, C. and Romero-Paredes, H. (2011 November). Heat transfer simulation in a thermochemical solar reactor based on a volumetric porous receiver. *Applied Thermal Engineering*, vol. 31, no. 16, pp. 3377–3386. ISSN 13594311.
- Wagner, M. (2008). *Simulation and predictive performance modeling of utility-scale central receiver system power plants*. Ph.D. thesis.
- Wiesenberg, R., Serrano, E., Villa, J., Rayo, D., Ruano, A., Santana, D., Reyes, R. and Barroso, H. (2012). Potential energy recovery system for central receiver solar power plants using molten salts as working fluid. In: *Proceedings of SolarPACES*, pp. 1–7. Marakech, Marocco.
- Winston, R. (1974). Principles of solar concentrators of a novel design. *Solar Energy*, vol. 16, pp. 89–95.
- Winston, R. and Hinterberger, H. (1975). Principles of cylindrical concentrators for solar energy. *Solar Energy*, vol. 17, pp. 255–259.
- Winston, R., Miñano, J. and Benitez, P. (2004). Nonimaging Optical Systems. In: *Nonimaging optics*, chap. 4, pp. 43–68. Elsevier Academic Press, Burlington, Vermont. ISBN 978-0-12-759751-5.
- Winter, C.-J., Vant-Hull, L.L. and Sizmann, R.L. (1991). *Solar Power Plants*. Springer-Verlag, Berlin, Heidelberg. ISBN 978-3-642-64759-8.  
Available at: <http://www.springerlink.com/index/10.1007/978-3-642-61245-9>
- Wu, S.-Y., Xiao, L., Cao, Y. and Li, Y.-R. (2010 August). Convection heat loss from cavity receiver in parabolic dish solar thermal power system: A review. *Solar Energy*, vol. 84, no. 8, pp. 1342–1355. ISSN 0038092X.
- Wu, Z., Caliot, C., Flamant, G. and Wang, Z. (2011 July). Coupled radiation and flow modeling in ceramic foam volumetric solar air receivers. *Solar Energy*, vol. 85, no. 9, pp. 2374–2385. ISSN 0038092X.
- Yang, X., Yang, X., Ding, J., Shao, Y. and Fan, H. (2012 February). Numerical simulation study on the heat transfer characteristics of the tube receiver of the solar thermal power tower. *Applied Energy*, vol. 90, no. 1, pp. 142–147. ISSN 03062619.
- Yu, Q., Wang, Z. and Xu, E. (2012 January). Simulation and analysis of the central cavity receiver's performance of solar thermal power tower plant. *Solar Energy*, vol. 86, no. 1, pp. 164–174. ISSN 0038092X.

- Yu-ting, W., Bin, L., Chong-fang, M. and Hang, G. (2009 October). Convective heat transfer in the laminar-turbulent transition region with molten salt in a circular tube. *Experimental Thermal and Fluid Science*, vol. 33, no. 7, pp. 1128–1132. ISSN 08941777.
- Zanganeh, G., Pedretti, A., Zavattoni, S., Barbato, M. and Steinfeld, A. (2012 October). Packed-bed thermal storage for concentrated solar power-Pilot-scale demonstration and industrial-scale design. *Solar Energy*, vol. 86, no. 10, pp. 3084–3098. ISSN 0038092X.